Doctoral Dissertation

# Study on the Mathematical Modeling of Motors with Magnetic Geared Effect

SHI HYOSEOK

July 2019

Department of Adaptive Machine Systems,
Graduate School of Engineering,
Osaka University

博士学位論文

# 磁気ギア効果を有するモータの数学的モデリングに関する研究

シ　ヒョソク

2019 年 07 月

大阪大学大学院工学研究科

知能・機能創成工学専攻

知能アクチュエータ・センサデバイス創成研究室

# Abstract

In recent years, there is a growing interest in magnetic gears that can replace mechanical gears in many industries. Mechanical gears have a high torque transmission capability. However, since the various gear pieces are directly in contact with each other to transmit torque, they have problems such as a vibration, noise and efficiency, and require a gear lubrication and cooling. On the other hand, since the magnetic gear is made of a non-contact type torque transmitting structure using magnetic force, it is possible to eliminate losses caused by the friction of the mechanical gear, and it is not necessary to incur the maintenance cost.

However, conventional magnetic gears have a problem that a practical transmission torque is insufficient due to a narrow facing area. In order to solve this problem, various types of magnetic gears have been proposed. In particular, coaxial magnetic gears driven by harmonics are attracting attention because they have a high torque density. Accordingly, various novel structures such as a vernier motor and a magnetic geared motor, which are based on the operational principle of a magnetic gear operated by harmonics of an air gap magnetic field, have been actively studied.

In this study, the operational principle is described in detail by the mathematical modeling of the air gap magnetic field distribution according to the structural characteristics of the motors with a magnetic gear effect, and the effectiveness is evaluated by comparing the analytical calculation results with the FEM results.

In Chapter 1, the types and history of magnetic gears are discussed. Next, the operational principles of magnetic gears using magnetic flux harmonics are explained and the purpose of this study is presented.

In Chapter 2, the mathematical modeling of the air gap magnetic field distribution of a magnetic geared motor with two air gaps is described. The results of magnetic flux density, back-emf and n-T characteristics of the inner and outer air gaps were evaluated and compared with FEM and prototype's experimental results. The analytical results showed a good agreement with FEM results and experimental results.

In Chapter 3, the mathematical modeling of the air gap magnetic flux density of the vernier motor is described first. Secondly, the analytical calculation results are compared with FEM and evaluated, and the analysis of the characteristics according to various pole combinations is performed. Next, a method to obtain design parameters with optimum values of the magnetic flux density space harmonic using the analytical calculation method is proposed and evaluated its effectiveness by comparing FEM and results.

In Chapter 4, this paper is summarized and future works of each chapter are described.

## Contents

# Chapter 1 Introduction

## 1.1 Magnetic Gears

Mechanical gears have been continually explored and exploited along with the remarkable development of the modern industry. Mechanical gears are used not only to transmit torque and force but also to alter the operating speed and direction. Mechanical gears work well in a wide variety of applications. However, the direct contact mechanism between the gears has many problems such as noise, vibration and efficiency reduction, and requires gear lubrication and maintenance.

On the other hand, since the magnetic gear is a non-contact structure that transmits power by using the magnetic force of the permanent magnet, many problems of the mechanical gear except the bearing loss can be eliminated. However, conventional magnetic gears have a problem that a practical transmission torque is insufficient due to a narrow facing area, and therefore, it is deficient to be utilized in an industrial field.

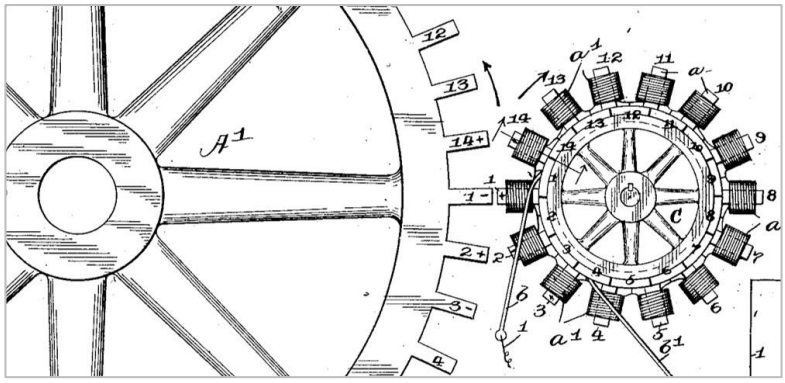

Fig. 1.1. First magnetic gear [1]

### 1.1.1 Early Magnetic Gears

The idea of magnetic gears began in the early 20th century. The first proposed magnetic gear was an electromagnetic spur gear[1] designed by Armstrong in 1901 (Fig. 1.1). The gear consisted of two gears, one with electromagnets as the gear teeth and the other with steel pieces. It utilizes a magnetic attraction by replacing the teeth of conventional mechanical gears with magnetic steel segments and electromagnets. In 1913, Neuland invented a far superior magnetic gear which should be the original topology[2]. The gear consisted of three parts: modulation magnet pieces, inner and outer rotors made of laminated sheets. The modulation magnet pieces are designed to

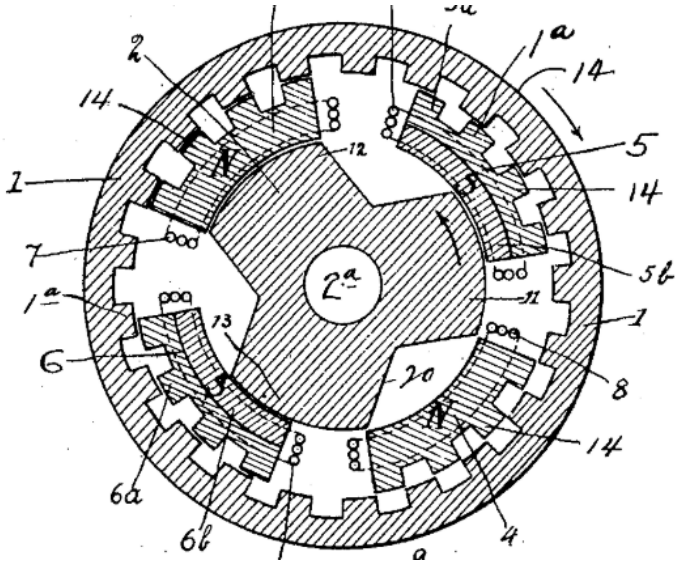

Fig. 1.2. Coaxial magnetic gear[2]

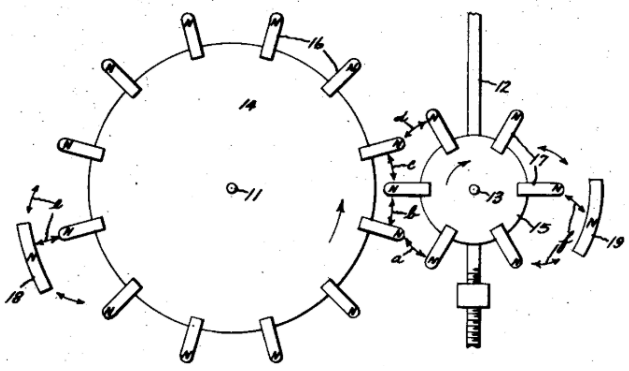

Fig. 1.3. Permanent magnet spur gear[3]

modulate the magnetic flux so that the inner and outer rotors are driven by the correct harmonics according to the number of teeth of each rotor. The torque density of the gear is significantly improved compared to Armstrong's gear. This is because all the sides of the permanent magnet are involved in the transmission torque by facing the rotors that transmit the torque. However, it did not attract much attention (Fig. 1.2). Faus[3] proposed a magnetic spur gear similar to the Armstrong model. However, it used permanent magnets instead of steel segments and electromagnets. The permanent magnet of the two rotors uses a repulsive magnet force by making the N pole always facing outward.

As the technology of permanent magnets developed, power transmission devices using permanent magnets were invented more and more. Hurvitz's magnetic spur gearbox, invented in 1951, was able to switch gears using electromagnets. However, it was inefficient and very bulky[4].

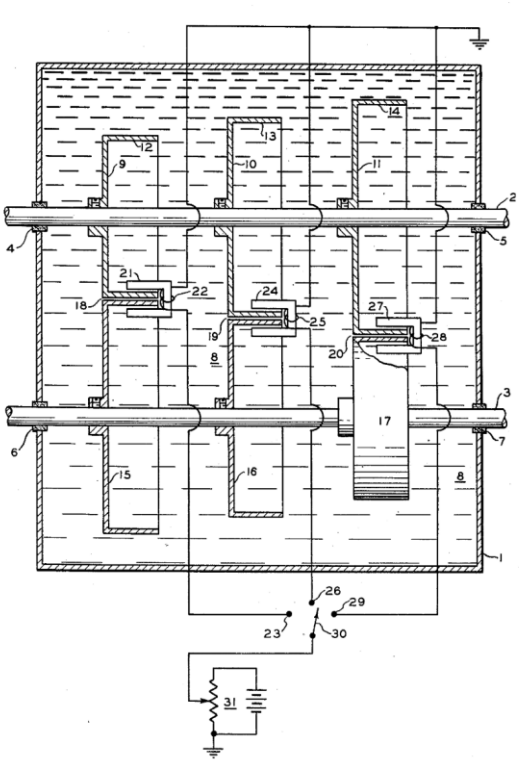


Fig. 1.4. Magnetic gearbox by Hurvitz[4]

In 1967, Reese[5] invented a coaxial magnetic gear with a permanent magnet on the inner rotor, though it has a structure similar to the Neuland's gear. As shown in Fig. 1.5, the inner rotor is a permanent magnet, and the output is a middle rotor. The outermost is the stator. The middle rotor and stator had different numbers of teeth. As the inner rotor rotates, the magnetic flux of the permanent magnet passes through the teeth of the middle rotor and the stator, and the middle rotor rotates at a gear ratio of the number of teeth of the middle rotor and the permanent magnet poles.

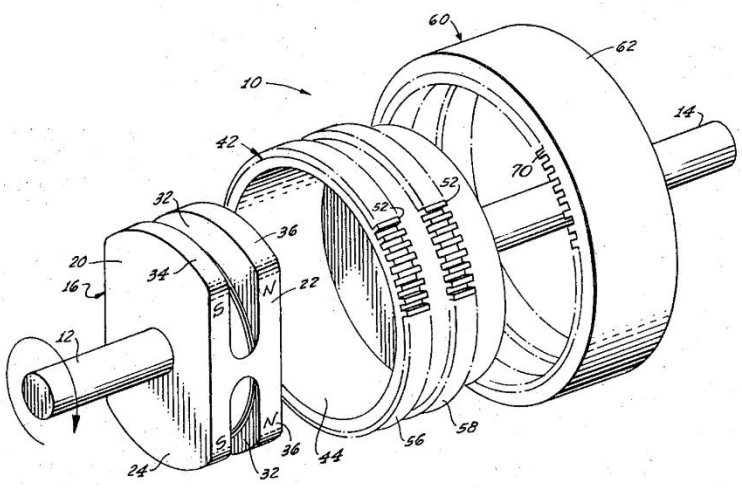


Fig. 1.5. Coaxial magnetic gear by Reese[5]

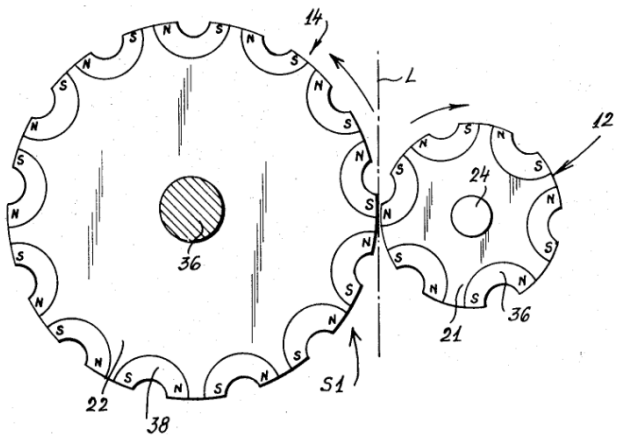


Fig. 1.6. Spur type magnetic gear by Rand[6]

A magnetic gear patented by Rand in 1970 (Fig. 1.6) was a simple spur type[6]. In its basic form, permanent magnets are mounted in circumferentially spaced disposition in two discs. The discs are adjacent to each other and transmit torque through the magnetic force of the arcuate bar magnets. This increased the amount of magnetic material needed and the manufacturing cost.

Since the 1970s, the development of magnetic gears has attracted wide attention due to the advent of rare-earth permanent magnets such as samarium-cobalt and the neodymium-iron-boron (Nd-Fe-B) alloys. Rare-earth permanent magnets have the ability to produce a significantly strong magnetic field without continuous exterior excitements. There are two major classes of magnetic gears: a converted topology and field modulated topology. The converted magnetic gear is a direct extension from the mechanical gear topology so that the mechanical gear's teeth and slots are replaced by the magnet's N-S pole. This type has a problem of causing a low torque density because the contact area of the permanent magnet is narrow. The field modulated magnetic gear is based on the modulation of magnetic fields produced by two permanent magnet rotors. Hence, all permanent magnets can simultaneously contribute to torque transmission, leading to offer higher torque density.

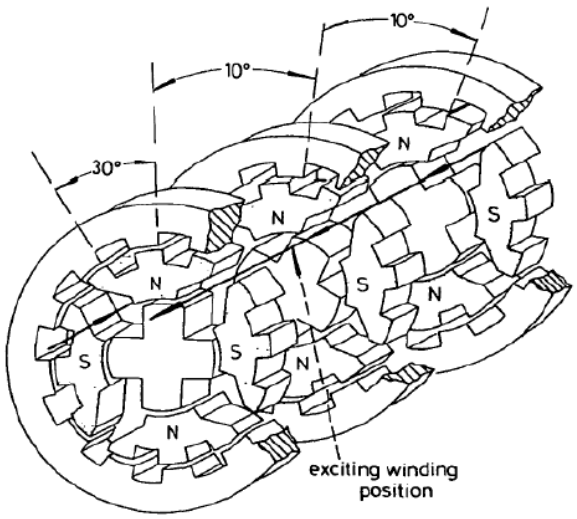


Fig. 1.7. Multi element magnetic gear [7]

### 1.1.2 Converted Magnetic Gears

In the 1980s, various types of magnetic gears were proposed and studied. Hermondhalgh and Tipping proposed a multi-element magnetic gear[7] (Fig. 1.7). The magnetic gear was arranged in an array of gears of Neuland's[2] to increase maximum torque and efficiency. Then, a magnetic involute gear[8] and a magnetic worm gear[9] were proposed by Tsurumoto and Kikuchi, as shown in Figs. 1.8 and 1.9, respectively.

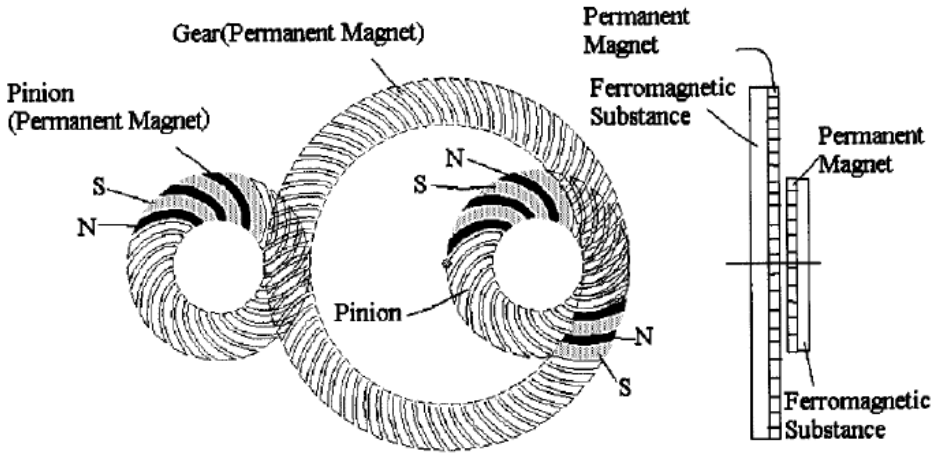


Fig. 1.8. Magnetic involute gear[8]

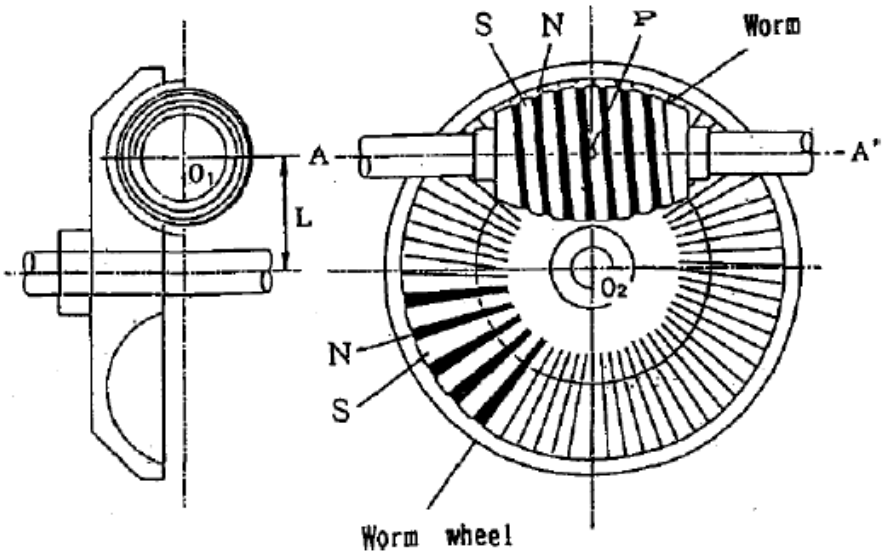


Fig. 1.9. Magnetic worm gear[9]

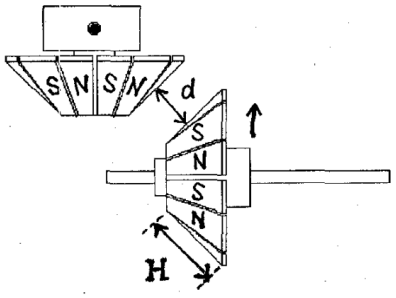


Fig. 1.10. Perpendicular-axis magnetic spur gear[10]

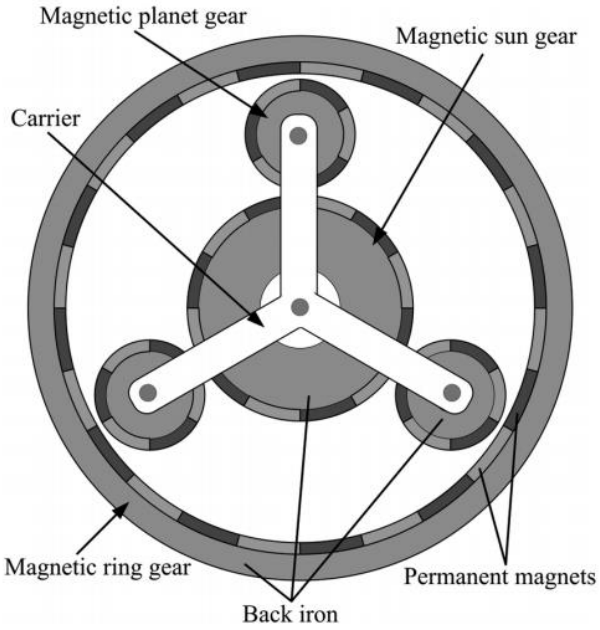


Fig. 1.11. Magnetic planetary gear[11]

Because the utilization of the permanent magnets is low, it is inevitable to show a low torque density.

In addition, a perpendicular-axis magnetic spur gear[10] is developed by Yao as shown in Fig. 1.10. In [10], a critical separation distance was explained where if the air gap length was smaller than the critical distance, the transmitted torque could be increased by increasing the number of poles. These magnetic gears similar in shape to mechanical gears have not been widely used in the industry because they are simple in construction but too low in torque density.

Accordingly, magnetic planetary gears[11] based on the structure of a mechanical

planetary gear were proposed by Yao as shown in Fig. 1.11. This magnetic planetary gear has achieved shear stress close to 100kNm/m$^3$ in magnetic ring gear. Hence, there is an increasing interest in using the magnetic planetary gear for various applications.

### 1.1.3 Field Modulated Magnetic Gears

In 2001, a novel topology for a high-performance magnetic gear was proposed by Atallah[12]. As shown in Figure 1.12, it consists of two rotors with permanent magnets mounted on the inner and outer sides and a stationary pole piece equipped with a ferromagnetic segment for modulating the magnetic field. The operational principle of modulating the magnetic field generated by the permanent magnet mounted on the inner and outer rotors to the ferromagnetic segment was presented in the paper [13].

The magnetic gears of this structure showed torque transmission densities, 50-150kNm/m$^3$, equal to those of the two- or three-stage mechanical helical gears because all the permanent magnets contributed to the transmission torque and can replace mechanical gears.

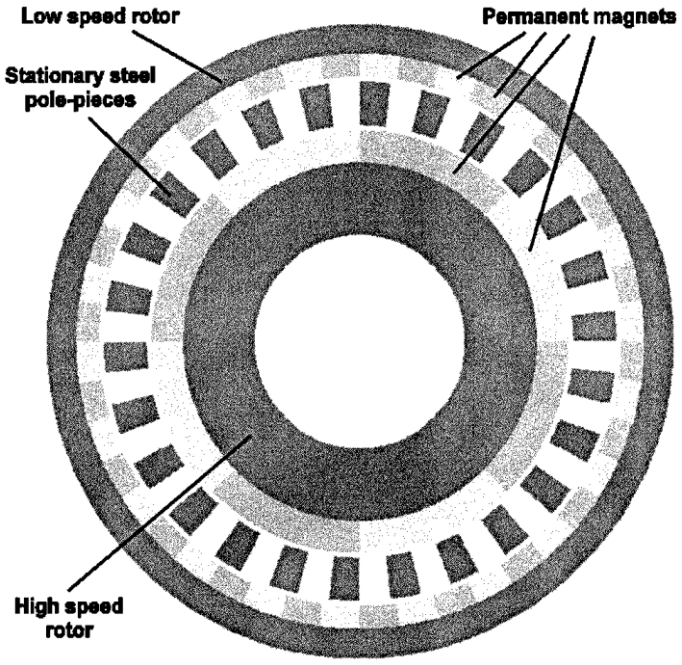


Fig. 1.12. Magnetic coaxial gear[12]

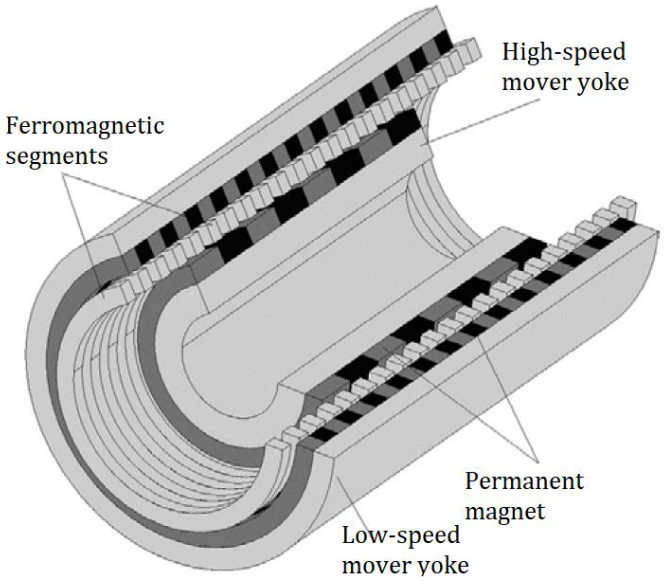


Fig. 1.13. Magnetic linear gear[14]

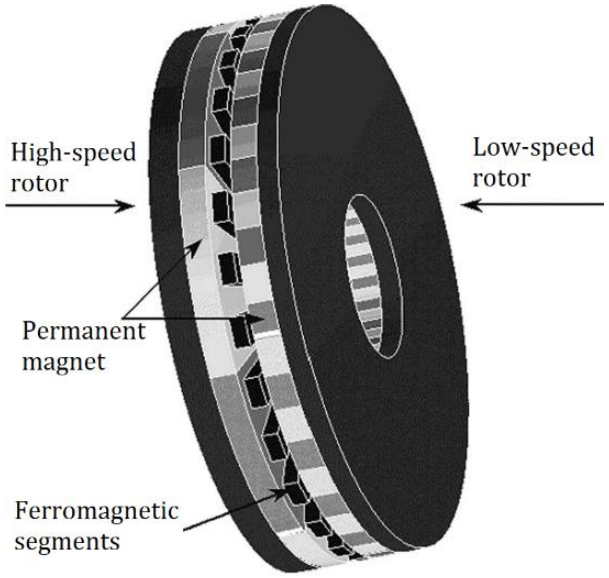


Fig. 1.14. Magnetic axial-flux gear[15]

Since their publication, magnetic gears with this operational principle have been proposed in various forms such as a magnetic linear gear[14] and magnetic axial-flux gear[15] as shown in Figs. 1.13 and 1.14, respectively.

The operational principle of the coaxial magnetic gear will be described in detail in the following chapter.

## 1.2 Operational Principle of Coaxial Magnetic Gears

### 1.2.1 Principle analysis using space harmonics

The coaxial magnetic gear is shown in Fig. 1.15 consists of high-speed, low-speed rotors and a stator. The coaxial magnetic gear is operated using space harmonics created according to a combination of the number of poles of the high-speed rotor, low-speed rotor and stator. In this chapter, the operational principle[16] that the magnetic gear is realized as a gear will be described by a mathematical formula.

Assuming that the low-speed rotor is removed, only the high-speed rotor permanent

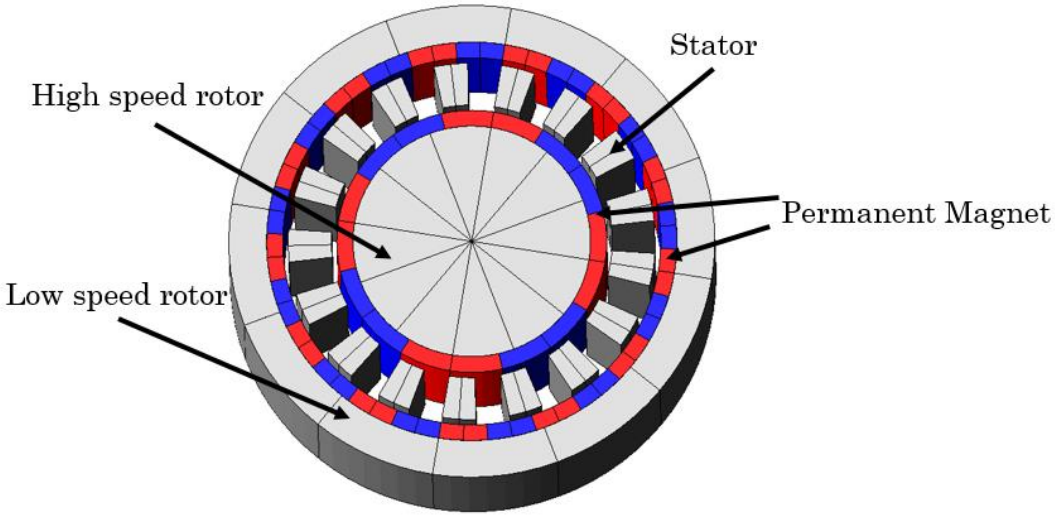


Fig. 1.15. Structure of coaxial magnetic gear

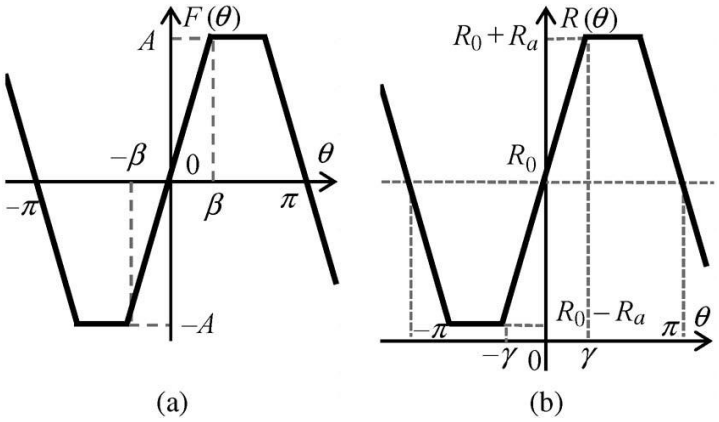


Fig. 1.16. Distribution of the (a) magnetomotive force and (b) permeance

magnet generates a magnetomotive force, as shown in Fig. 1.16(a). The permeance shown in Fig. 1.16(b) is modified by the stationary pole pieces, where $\theta$ represents the rotor angle. This permeance distribution is attributed to the difference in a magnetic resistance between the pole piece made of magnetic material and the air in the slot. The Fourier series expansions of the magnetomotive force $F(\theta)$ by the permanent magnet of the high-speed rotor and the permeance $R(\theta)$ of the stationary pole piece are shown in

$$F(\theta) = \sum_{m=1}^{\infty} a_m \sin\left\{\left(2m-1\right) N_h \theta\right\} \tag{1.1}$$

$$R(\theta) = R_0 + \sum_{l=1}^{\infty} a_l \sin\left\{\left(2l-1\right) N_s \theta\right\} \tag{1.2}$$

where $N_h$ and $N_s$ are the number of pole pairs of the high-speed rotor and stationary pole pieces, respectively. $a_m$ and $a_l$ are constants that depend on $m$ and $l$. $R_0$ is the average permeance of the radial direction of the stationary part.

Moreover, the magnetic flux distribution $\phi(\theta)$ can be obtained by the product between the magnetomotive force and permeance as follows:

$$\begin{aligned}\phi(\theta) = &\sum_{m=1}^{\infty} a_m R_0 \sin\left\{\left(2m-1\right) N_h \theta\right\} \\ &+\sum_{l=1}^{\infty}\sum_{m=1}^{\infty} \frac{a_l a_m}{2}\left[\cos\left\{\left(2l-1\right) N_s - \left(2m-1\right) N_h\right\}\theta - \cos\left\{\left(2l-1\right) N_s + \left(2m-1\right) N_h\right\}\theta\right]\end{aligned} \tag{1.3}$$

The stationary pieces modulate the magnetic flux density distribution from the high-speed rotor permanent magnet to produce a new imaginary magnet, shown in Fig.1.17, which has $N_h$ and $N_s \pm N_h$ pole pairs. When the high-speed rotor is rotated $\Delta\theta$, the magnetic flux $\phi(\theta)$ is expressed as

$$\begin{aligned}\phi(\theta) = &\sum_{m=1}^{\infty} a_m R_0 \sin\left\{\left(2m-1\right) N_h \left(\theta + \Delta\theta\right)\right\} \\ &+\sum_{l=1}^{\infty}\sum_{m=1}^{\infty} \frac{a_l a_m}{2}\left[\begin{array}{l}\cos\left[\left\{\left(2l-1\right) N_s - \left(2m-1\right) N_h\right\}\left\{\theta - \dfrac{\left(2m-1\right) N_h \Delta\theta}{\left(2l-1\right) N_s - \left(2m-1\right) N_h}\right\}\right] \\ -\cos\left[\left\{\left(2l-1\right) N_s + \left(2m-1\right) N_h\right\}\left\{\theta + \dfrac{\left(2m-1\right) N_h \Delta\theta}{\left(2l-1\right) N_s + \left(2m-1\right) N_h}\right\}\right]\end{array}\right]\end{aligned} \tag{1.4}$$

From (1.4), the magnetic flux component $(2m-1)N_h$, $(2l-1)N_s-(2m-1)N_h$ and $(2l-1)N_s+(2m-1)N_h$ each rotates $\Delta\theta$, $-\{(2m-1)N_h\Delta\theta\}/\{(2l-1)N_s-(2m-1)N_h\}$ and $\{(2m-1)N_h\Delta\theta\}/\{(2l-1)N_s+(2m-1)N_h\}$, respectively. To operate as a reduction gear, the number of pole pairs of the low-speed rotor should be equal to $(2l-1)N_s-(2m-1)N_h$ or $(2l-1)N_s-(2m-1)N_h$. Hence, the relationship among $N_h$, $N_s$ and $N_l$ can be obtained as follows:

$$(2l-1)N_s = N_l \pm (2m-1)N_h \tag{1.5}$$

The gear ratio can also be obtained as follows:

$$G_r = \mp \frac{N_l}{(2m-1)N_h} \tag{1.7}$$

where the minus sign indicates that the low-speed rotor rotates in the opposite direction of the high-speed rotor.

On the other hands, as shown in Fig. 1.17, if the stationary pole piece rotates as a low-speed rotor($N_s \rightarrow N_l$), and the low-speed rotor is fixed as a stator($N_l \rightarrow N_s$), the equation can be rearranged.

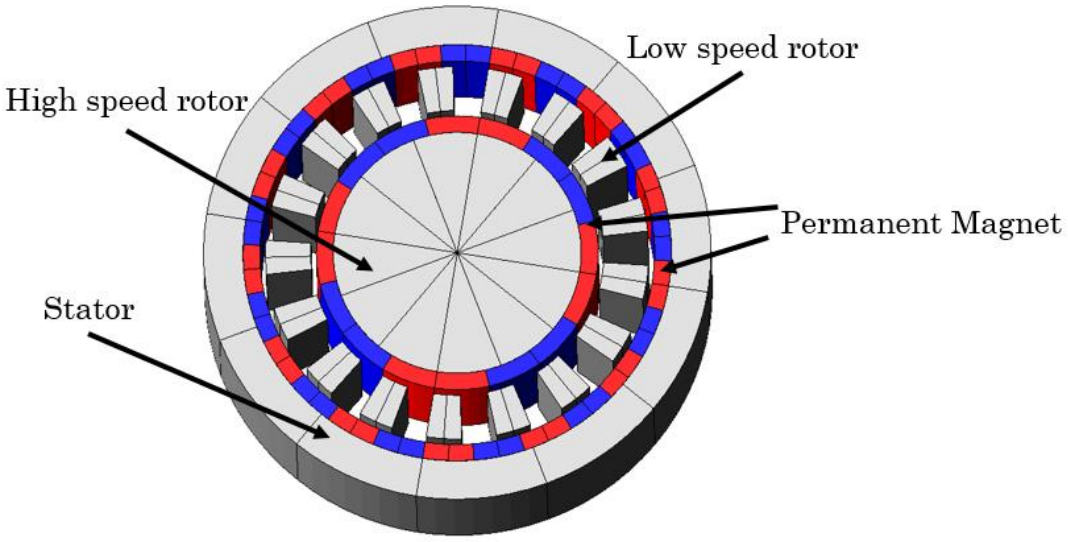


Fig. 1.17. Coaxial magnetic gear

$$F(\theta)=\sum_{m=1}^{\infty}a_m\sin\left\{(2m-1)N_h(\theta+\alpha)\right\} \tag{1.8}$$

$$R(\theta)=R_0+\sum_{l=1}^{\infty}a_l\sin\left\{(2l-1)N_l(\theta+\beta)\right\} \tag{1.9}$$

where $\alpha$ and $\beta$ are rotating angles of the high-speed and low-speed rotors, respectively. Then, the magnetic flux $\phi(\theta)$ can be expressed as

$$\begin{aligned}\phi(\theta)=&\sum_{m=1}^{\infty}a_m R_0\sin\left\{(2m-1)N_h(\theta+\alpha)\right\}\\&+\sum_{l=1}^{\infty}\sum_{m=1}^{\infty}\frac{a_l a_m}{2}\left[\begin{array}{l}\cos\left[\left\{(2l-1)N_l-(2m-1)N_h\right\}\left\{\theta-\dfrac{(2m-1)N_h\alpha-(2l-1)N_l\beta}{(2l-1)N_l-(2m-1)N_h}\right\}\right]\\-\cos\left[\left\{(2l-1)N_l+(2m-1)N_h\right\}\left\{\theta+\dfrac{(2m-1)N_h\alpha+(2l-1)N_l\beta}{(2l-1)N_l+(2m-1)N_h}\right\}\right]\end{array}\right]\end{aligned} \tag{1.10}$$

According to (1.10), the harmonic components of the magnetic flux are equal to (1.4) and rotation angles are changed by $\beta$. Therefore, the relationship among $N_h$, $N_s$ and $N_l$ is the same as in (1.5), the gear ratio can be defined as follows:

$$G_r=\mp\frac{(2l-1)N_l}{(2m-1)N_h} \tag{1.11}$$

### 1.2.2 Coaxial Magnetic Gear Design Example

Through the design example, the theory of the previous chapters will be verified. As shown in Fig. 1.18, in this design example, the inner rotor is a high-speed rotor, the modulated pole pieces in the middle are a low-speed rotor and the outermost is a stator. The example gear has 4- and 13-pole pairs of permanent magnets mounted on the high-speed rotor and stator, respectively, and 17-pole pieces of magnetic steel sheets of the low-speed rotor. Therefore, the gear ratio of the high-speed rotor($N_h=4$) and the low-speed rotor($N_l=17$) is 4.25.

To obtain the maximum transmission torque of the model, the low-speed rotor was fixed and the torque was measured by rotating only the high-speed rotor. The torque waveform of the model is shown in Fig. 1.19. The maximum transmission torque of the

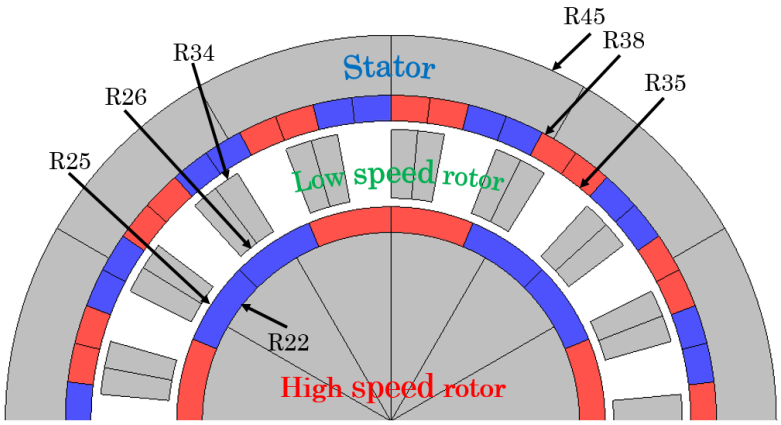


Fig. 1.18. Parameters of the magnetic gear

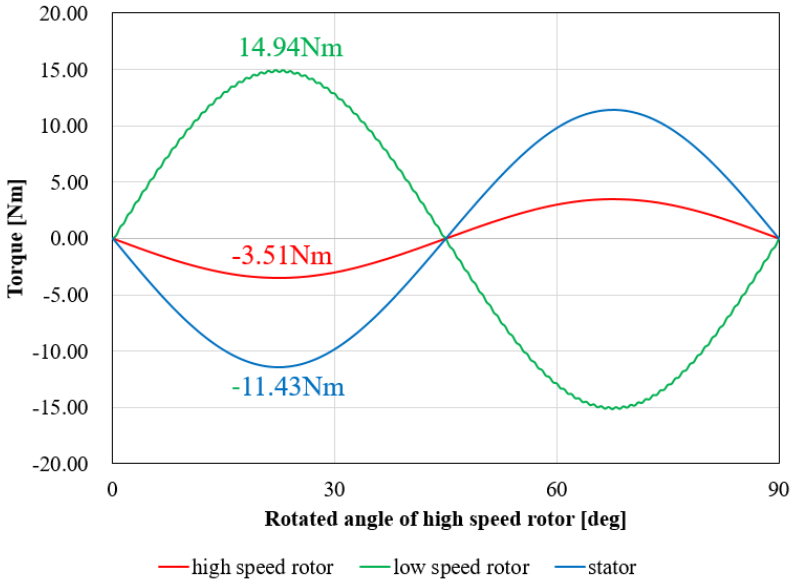


Fig. 1.19. Torque waveform of magnetic gear

low-speed rotor is 14.94 Nm and the gear ratio is $G_r = N_l / N_h = 14.94/-3.51 \approx -4.25$. As mentioned in chapter 1.2.1, assuming that the stator operates as a low-speed rotor, the output torque ratio is $-11.43/-3.51 \approx 3.25$, which is consistent with the theory in (1.7).

## 1.3 Electrical Machines with Magnetic Geared Effect

Since magnetic gears were introduced as mentioned in the previous chapter, various types of devices have been proposed using magnetic geared effects, such as magnetic geared motors[17-21], continuously variable speed vernier magnetic gears[22-24], and vernier motors[25-37]. In this research, mathematical modeling of magnetic geared motors and vernier motors is focused. Therefore, this chapter briefly discusses the types and origins of magnetic geared motors and vernier motors. Their details are explained in Chapter 2 and 3.

### 1.3.1 Magnetic Geared Motor

In 2008, Atallah proposed a magnetic geared motor[21] that shared the magnetic circuit of a magnetic gear and brushless DC motor as shown in Fig. 1.20. The Atallah's magnetic geared motor has a two-layered air gap and can use the same support structure as a coaxial magnetic gear. Since the magnetic circuit is integrated, the permanent magnet of the high-speed rotor is used as a magnetic gear and also as a

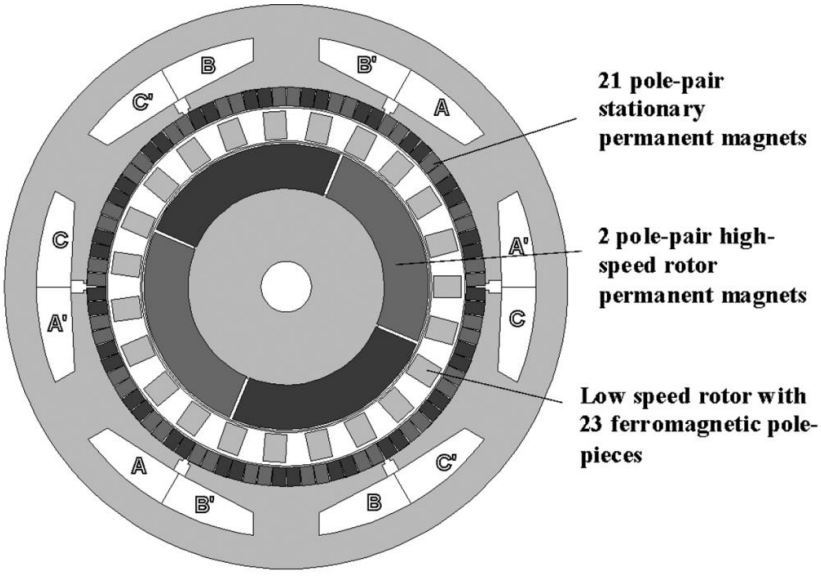


Fig. 1.20. Magnetically and mechanically coupled magnetic gear and permanent magnet brushless machine[21]

rotor of the motor. Therefore, compared to a drive system composed of a magnetic gear and a motor, it is possible to reduce the amount of permanent magnet used in the system, and it leads to a lower cost and miniaturization. However, the magnetic geared motor in Fig. 1.20 applies a current to a coil of the stator to rotate the high-speed rotor. Since the permanent magnet and the steel pieces are in the gap between the stator and the high-speed rotor, the magnetic resistance is large and the armature flux is very low.

In 2012, Niguchi proposed a magnetic geared motor[17], as shown in Fig. 1.21, that removes the permanent magnet of the stator from a conventional magnetic gear and drives a high-speed rotor by applying currents to the coils. This structure has the effect of increasing the flux linkage as the distance between the stator and the high-speed rotor is reduced compared to Atallah's model[21]. However, as the permanent magnet was excluded from the stator side, the torque transmitted to the low-speed rotor as a magnetic gear was measured to be extremely low.

Thus, in 2015, Niguchi proposed two models[20], as shown in Figs. 1.22 and 1.23, that can dramatically improve the transmission torque by placing permanent magnets

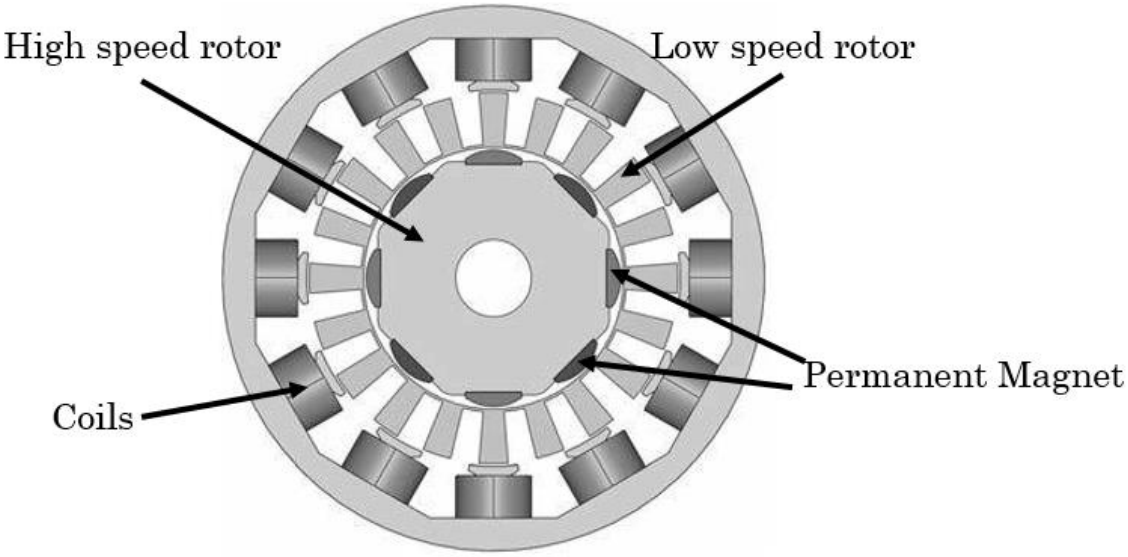


Fig. 1.21. Niguchi's magnetic geared motor[17]

between the stator teeth, and showed a higher torque density than the Atallah's model. Also, to reduce the amount of permanent magnet, the magnetic-geared motor shown in Fig. 1.23 is proposed, where the amount of the permanent magnets in the high-speed rotor is half of that shown in Fig. 1.23.

In chapter 2, the mathematical modeling of a magnetic geared motor is performed

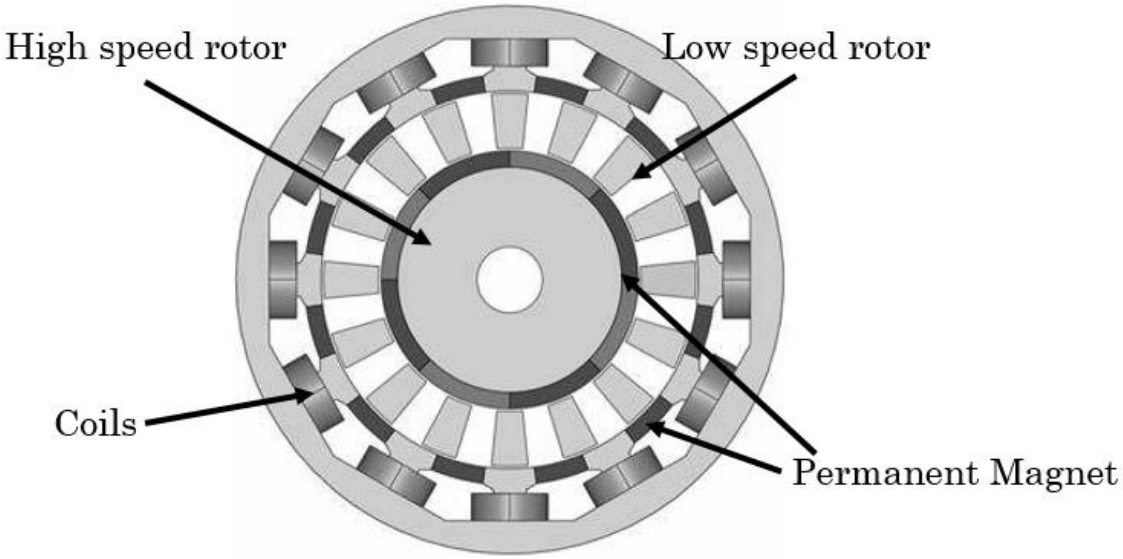


Fig. 1.22. Niguchi's high toque type magnetic geared motor[20]

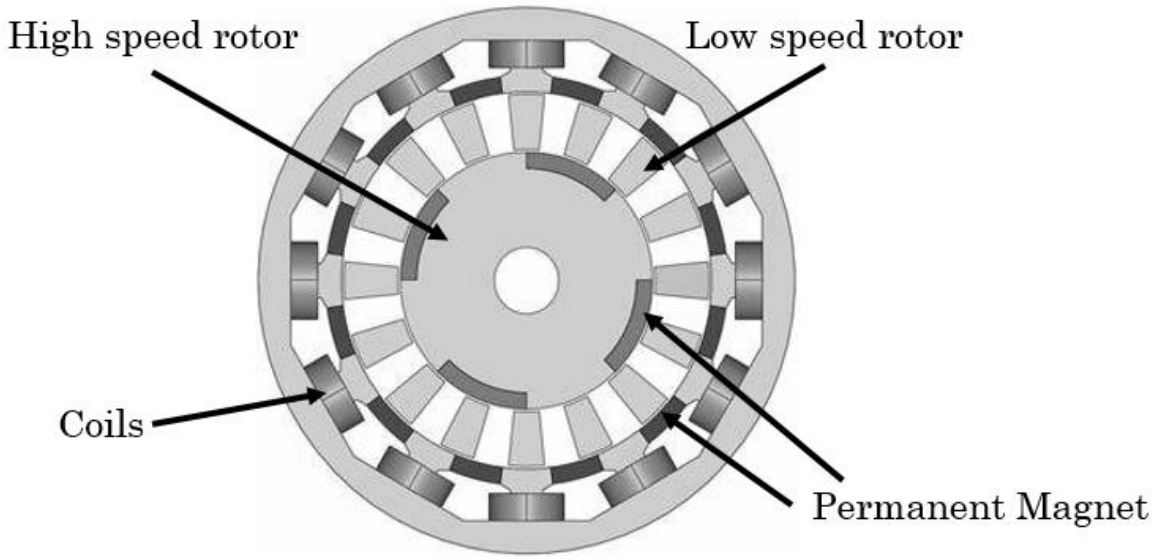


Fig. 1.23. Niguchi's high torque type magnetic geared motor with half permanent magnet[20]

to obtain the calculation results of the air gap magnetic field, the EMF and the torque output, and its effectiveness is verified by comparing the experimental results with the FEM.

### 1.3.2 Vernier Motor

The vernier motor is a kind of motors that uses the operational principle of the magnetic gear and has the feature of high torque at low speeds similarly to the magnetic gear. The first vernier motor was proposed by C. H. Lee in 1968[25]. The vernier motor was an unexcited inductor synchronous motor in which a small displacement of the rotor produces a large displacement of the axes of permeance. He mentioned that the vernier motor was named because it operates on the principle of a vernier. Since then, interests in vernier motors have been revived with advancements in permanent magnets and permanent magnet brushless motors.

Since the advent of the vernier motor, various types of vernier motors have been proposed, such as vernier reluctance[32,35], hybrid and surface permanent magnet types.

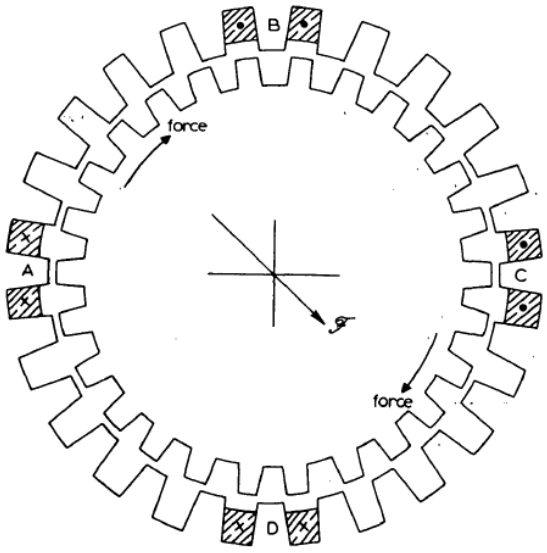


Fig. 1.25. K. C. Mukherji's vernier reluctance motor[32]

As shown in Fig. 1.25, Mukherji proposed a vernier reluctance motor[32]. It has been estimated that this vernier reluctance motor has a slightly higher output coefficient compared to an induction motor. However, it does not show much difference. In 2017, Sekine proposed a reluctance type bearingless vernier motor[36] as shown in Fig. 1.26 and investigated the stator structure, the number of teeth, tooth width, tooth depth for generating a high torque and suspension force. Many experimental results have contributed to improving the maximum torque.

The vernier hybrid motor[31] as shown in Fig. 1.27 was proposed by E. Spooner in 2013. Although the proposed motor has a rotor with teeth like a vernier reluctance motor, it has a permanent magnet on the stator side, and it can be economically designed with a small number of stator teeth and has a high torque. However, there is a drawback that the power factor is low.

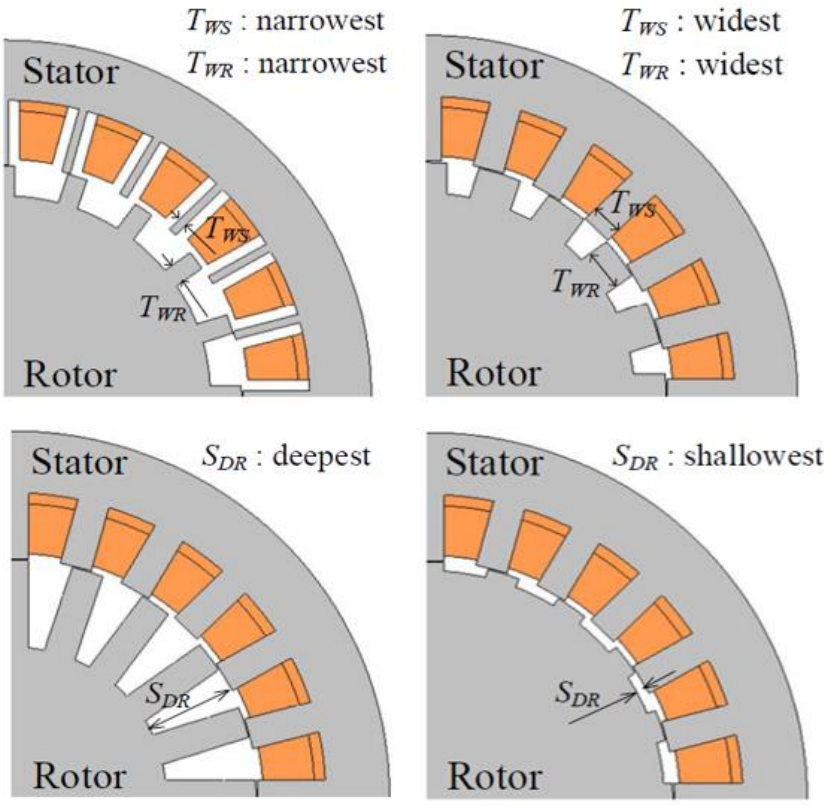


Fig. 1.26. Vernier reluctance motor proposed by Sekine[36]

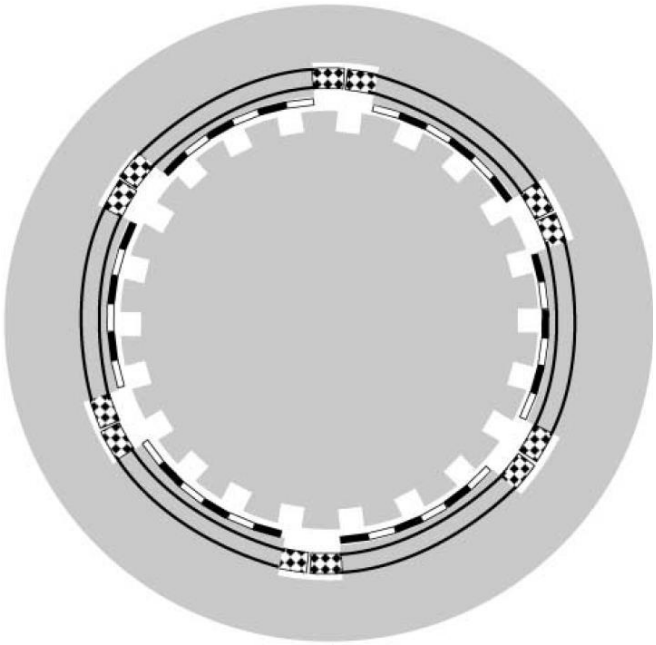

Fig. 1.27. Vernier hybrid motor[31]

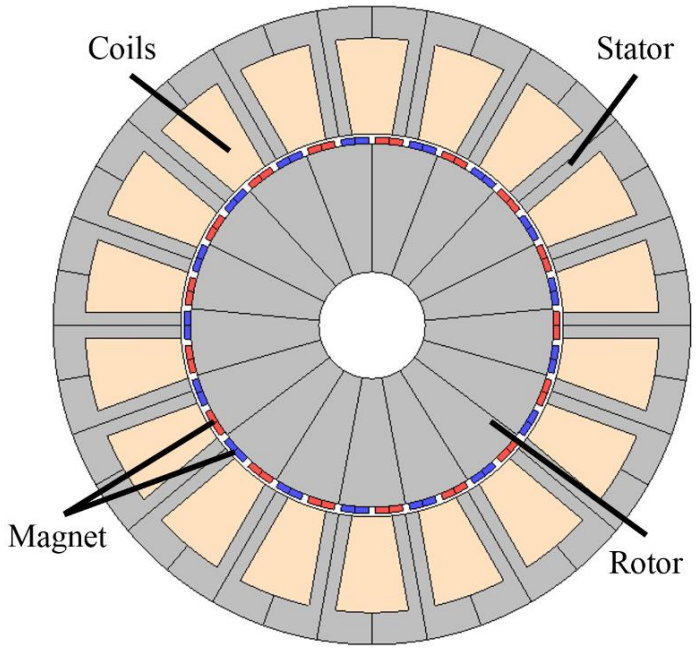


Fig. 1.28. Surface permanent magnet vernier motor[29]

Surface permanent magnet vernier motors[26-30] are very similar to general synchronous motors as shown in Fig. 1.28. Ishizaki introduced the structure of surface permanent magnet vernier motor[30] in 1995 and proposed a design method based on vernier theory. In 2000, Toba presented a novel torque-maximized design

methodology[26] through a quantitative analysis of the machine. This method showed a clear design policy and reduced a design effort compared to the conventional method. However, there was no modeling of the thickness of the permanent magnet and the stator slot which greatly affect the performance of the vernier motor, so that a definite maximum torque could not be obtained. Therefore, in chapter 3, precise mathematical modeling that reflects mechanical dimensions and a design method that can maximize the performance by using an analytical method are proposed.

In addition to the types mentioned above, various types of vernier motors such as spoke-array magnet type[37] and axial type[34], etc. have been constantly being studied. Chapter 3 in this paper focuses on permanent magnet vernier motors.

## 1.4 Purpose and Outline of Thesis

This paper is aimed at mathematical modeling of magnetic geared motor and surface permanent magnet vernier motor with magnetic gear effect. The performance of the motors can be calculated and predicted using an analytical calculation method before the time-consuming FEM is performed. Also, a torque-maximizing design method by analyzing the air gap magnetic field characteristic of a surface permanent magnet vernier motor is proposed. The proposed method is verified through the analysis of characteristics of output according to pole combinations and the design of surface permanent vernier linear motor.

Chapter 1.1 describes the history and types of magnetic gears, and their operating principles, on which the purpose of the proposal is based. Chapters 1.2 and 1.3 describe the history and types of magnetic geared motors and vernier motors using magnetic geared effects and present the purpose of this paper.

Chapter 2 describes the operation principle of the magnetic geared motor and the process of deriving the mathematical modeling and evaluates its effectiveness by comparing it with experimental results using FEM and prototype.

Chapter 3 deals with the mathematical modeling of vernier motors. In Chapter 3.2

and 3.3, the process of the mathematical modeling of surface permanent magnet vernier motors is performed step by step, and the results are compared with FEM and evaluated. Chapter 3.4 presents a design methodology for vernier motors that brings its torque-maximizing structure using mathematical modeling methods. Next, the comparative analysis is performed on the characteristics of the variation of the pole ratio and the number of winding poles pairs. Finally, a surface permanent magnet vernier linear motor is designed by applying the design procedure and the effectiveness of the design process methodology is evaluated by comparing the torque-speed characteristics of the designed model with the existing model.

Chapter 4 summarizes this paper.

# Chapter 2 Mathematical modeling for magnetic geared motor

## 2.1 Introduction

Magnetic geared motors are operated using the identical operational principle as general synchronous motors equipped with magnetic gears. The magnetic geared motor is structurally similar to a magnetic gear. However, by applying currents to the stator coil, the high-speed rotor is rotated by a magnetic field and the low-speed rotor is rotated according to the gear ratio.

In this chapter, the operational principle of a magnetic geared motor and the magnetic flux density distribution in its inner and outer air gaps are described. Then the harmonics of the magnetic flux density in the inner- and outer- air gaps are used to describe a method for calculating the mechanical and electrical output. Results obtained with the analytical calculation method are compared with those of the finite element analysis. Finally, a prototype is used to verify the results of the analytical calculation and FEA.

## 2.2 Analytical Calculation of the Air Gap Magnetic Flux Density Distribution in a Magnetic Geared Motor

The magnetic geared motor shown in Fig. 2.1 is similar to the structure of the magnetic gear composed of the high- and low-speed rotors and stator. The high-speed rotor consists of a five pole pair of permanent magnet( $B_r = 1.44T$ ) and a yoke. The low-speed rotor is composed of 17 magnetic pole-pieces formed by laminated steel sheets 50A400. The stator with 12 slots has a three-phase concentrated winding. The high-speed rotor is rotated by currents applied to the coil wound on the stator slot with a winding factor of 0.933. It should be stressed here that the low-speed rotor cannot be

rotated by the rotating flux due to the current. The low-speed rotor is rotated by employing the operational principle of a magnetic gear. Therefore, the relationship between the number of the permanent magnet of the high-speed rotor, the number of teeth of the low-speed rotor and the number of permanent magnet poles between the stator teeth should be satisfied as follows[20]:

$$(2l-1)N_s = N_l \pm (2m-1)N_h \tag{2.1}$$

where $m$ and $n$ are positive integers, $N_h$ is the pole-pair number of the permanent magnet on the high-speed rotor, $N_l$ is the number of steel pole pieces in the low-speed rotor, and $N_s$ is the number of slots and pole-pairs of the permanent magnet in the stator.

To analytically calculate the air gap magnetic fields of the magnetic geared motor, the magnetic flux densities of the outer and inner air gaps should be separately calculated centering on the low-speed rotor.

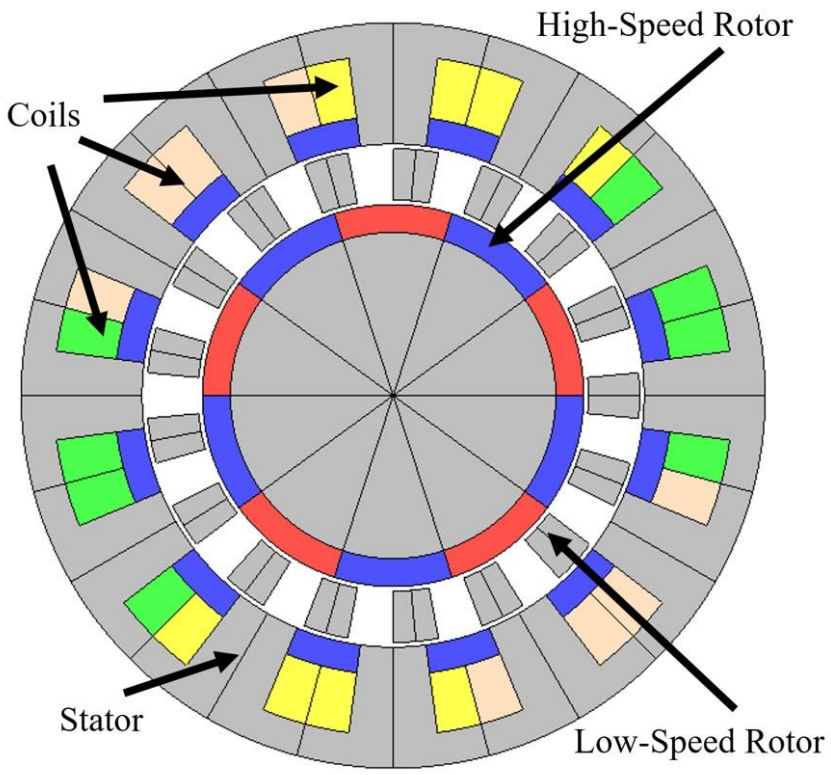


Fig. 2.1. Cross section of a magnetic geared motor

### 2.2.1 Magnetic Flux Density in the Inner Air Gap

In order to calculate the magnetic flux density distribution in the inner air gap, it is assumed that there is no stator. Only the high-speed rotor and low-speed rotor are used for the calculation. This is because the magnetomotive force generated by the permanent magnet on the stator has a considerably small influence on the inner air gap. An analytical method for modeling the effect of the stator slotting of a radial field brushless permanent magnet dc motor was presented in [38]. The air gap permeance of the low-speed rotor teeth with the slotting effect, as shown in Fig. 2.2, can be calculated by a Fourier decomposition with a unit magnetic potential between the low-speed rotor teeth and the high-speed rotor permanent magnet. Therefore, the permeance function $P^{in}(\theta+\delta)$ of the low-speed rotor can be described by the following equation:

$$P^{in}(\theta+\delta) = P_0^{in} + \sum_{i=1}^{\infty} P_i^{in} \cos\left\{(2i-1) N_l (\theta+\delta)\right\} \tag{2.2}$$

where $N_l$ is the number of the low-speed rotor pole pieces. The coefficients $P_0^{in}$ and $P_i^{in}$ in (2.2) can be obtained as follows:

$$P_0^{in} = \frac{\mu_0}{K_c^{in} g_e^{in}} \left(1 - 1.6 \beta^{in} r_o^{in}\right) \tag{2.3}$$

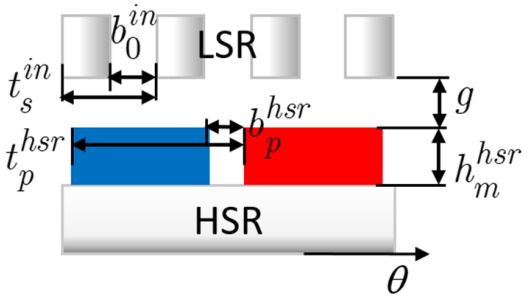


Fig. 2.2. Slotted structure of inner air gap

$$g_e^{in} = g + \frac{h_m^{hsr}}{\mu_r} \tag{2.4}$$

$$P_i^{in} = \frac{4}{i\pi}\frac{\mu_0}{g_e^{in}}\beta^{in}\left[0.5 + \frac{\left(ir_o^{in}\right)^2}{0.78125 - 2\left(ir_o^{in}\right)^2}\right]\sin\left(1.6\pi i r_o^{in}\right) \tag{2.5}$$

$$K_c^{in} = \left[1 - \frac{2}{\pi}r_o^{in}\left\{\tan^{-1}\left(\frac{b_0^{in}}{g_e^{in}}\right) - \frac{g_e^{in}}{b_0^{in}}\ln\left[1 + \frac{1}{4}\left(\frac{b_0^{in}}{g_e^{in}}\right)\right]\right\}\right]^{-1} \tag{2.6}$$

$$\beta^{in} = \frac{1}{2} + \frac{1}{2\sqrt{1 + \left(\frac{t_s^{in} r_o^{in}}{2g_e^{in}}\right)}} \tag{2.7}$$

where $r_o^{in}$ is the opening ratio of the opening length $b_0^{in}$ to the pitch $t_s^{in}$; $\mu_r$ and $\mu_0$ are the relative permeabilities of the low-speed rotor and the high-speed yokes with respect to the permeability of a vacuum. $g$, $h_m^{hsr}$ and $g_e^{in}$ are the air gap length, the permanent magnet thickness shown in Fig. 2.2, and the replaced air gap length for the computation of Carter's coefficient [40]. Carter's coefficient $K_c^{in}$ has been included to account for the increase in the effective air gap length due to the slotting phenomenon of the low-speed rotor. The magnetomotive force due to the permanent magnet of the high-speed rotor is expressed by:

$$F^{hsr}\left(\theta + \gamma\right) = \sum_{j=1}^{\infty} A_j^{hsr}\cos\left\{\left(2j-1\right)N_h\left(\theta + \gamma\right)\right\} \tag{2.8}$$

where $N_h$ is the pole-pair number of the permanent magnet of the high-speed rotor. The coefficient $A_j^{hsr}$ of the MMF function is the magnetization, which is assumed to be uniform throughout the cross-section of the permanent magnets and is given by [38]:

$$A_j^{hsr} = \frac{B_r}{\mu_0 j N_h} r_p^{hsr} h_m^{hsr} \frac{\sin\left(\frac{j\pi r_p^{hsr}}{2}\right)}{\frac{j\pi r_p^{hsr}}{2}} \tag{2.9}$$

where $B_r$ is the permanent magnet remanence, and $r_p^{hsr}$ is the ratio of the permanent magnet pole $\left(t_p^{hsr} - b_p^{hsr}\right)$ to the pole pitch $t_p^{hsr}$. Using the product between the air gap

permeance $P^{in}(\theta+\delta)$ and the magnetomotive force $F^{hsr}(\theta+\gamma)$, the magnetic flux density in the inner air gap can be obtained by

$$
\begin{aligned}
B^{inner}(\theta) &= F^{hsr}(\theta+\gamma)P^{in}(\theta+\delta) \\
&= \sum_{j=1}^{\infty} A_j^{hsr} P_0^{in} \cos\left\{(2j-1)N_h(\theta+\gamma)\right\} \\
&+ \sum_{i=1}^{\infty}\sum_{j=1}^{\infty} \frac{A_j^{hsr} P_i^{in}}{2} \times \left[ \begin{array}{l} \cos\left[\left\{(2j-1)N_h+(2i-1)N_l\right\}\left\{\theta+\dfrac{(2j-1)N_h\gamma+(2i-1)N_l\delta}{(2j-1)N_h+(2i-1)N_l}\right\}\right] \\ +\cos\left[\left\{(2j-1)N_h-(2i-1)N_l\right\}\left\{\theta+\dfrac{(2j-1)N_h\gamma-(2i-1)N_l\delta}{(2j-1)N_h-(2i-1)N_l}\right\}\right] \end{array} \right]
\end{aligned}
\tag{2.10}
$$

### 2.2.2 Magnetic Flux Density in the Outer Air Gap

To calculate the magnetic field distribution in the outer air gap, it is necessary to compute the magnetic flux density by the magnetomotive force of the permanent magnet between the stator teeth and the air gap permeance by the low-speed rotor. It is also necessary to consider the influence of the permanent magnet on the high-speed rotor. Thus, the magnetic flux density in the outer air gap can be described as a combination of the magnetic flux from the magnetomotive force due to the permanent magnet and permeance of the low-speed rotor, and the magnetomotive force due to the

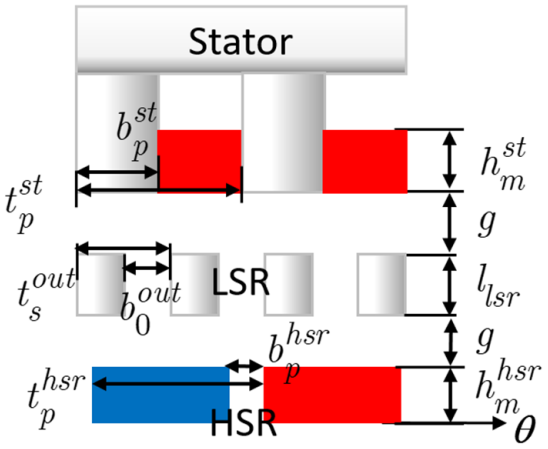


Fig. 2.3. Overall slotted structure

permanent magnet on the stator teeth and the air gap permeance of the low-speed rotor. As mentioned above, the methods used for calculating the air gap permeance and magnetomotive force are similar to those discussed above. The outer air gap permeance $P^{out}(\theta+\delta)$ of the low-speed rotor can be obtained as follows:

$$P^{out}(\theta+\delta) = P_0^{out} + \sum_{i=1}^{\infty} P_i^{out} \cos\left\{(2i-1) N_l (\theta+\delta)\right\} \tag{2.11}$$

$$P_0^{out} = \frac{\mu_0}{K_c^{out} g_e^{out}} \left(1 - 1.6 \beta^{out} r_o^{out}\right) \tag{2.12}$$

$$g_e^{out} = g + \frac{h_m^{st}}{\mu_r} \tag{2.13}$$

$$P_i^{out} = \frac{4}{i\pi} \frac{\mu_0}{g_e^{out}} \beta^{out} \left[ 0.5 + \frac{\left(i r_o^{out}\right)^2}{0.78125 - 2\left(i r_o^{out}\right)^2} \right] \sin\left(1.6\pi i r_o^{out}\right) \tag{2.14}$$

$$K_c^{out} = \left[ 1 - \frac{2}{\pi} r_o^{st} \left\{ \tan^{-1}\left( \frac{b_0^{st}}{g_e^{out}} \right) - \frac{g_e^{out}}{b_0^{st}} \ln\left[ 1 + \frac{1}{4}\left( \frac{b_0^{st}}{g_e^{out}} \right) \right] \right\} \right]^{-1} \tag{2.15}$$

$$\beta^{out} = \frac{1}{2} + \frac{1}{2\sqrt{1 + \left( \frac{t_s^{st} r_o^{out}}{2 g_e^{out}} \right)}} \tag{2.16}$$

where $r_o^{out}$ is the ratio of the opening length $b_o^{out}$ to the pitch $t_s^{out}$ of the low-speed rotor adjacent to the outer air gap, and $h_m^{st}$ is the permanent magnet thickness as shown in Fig. 2.3. In (2.15), $k_t^{out}$ is Carter's coefficient, and $g_e^{out}$ is the replaced air gap length for the computation of Carter's coefficient of the outer air gap.

The magnetomotive force of the permanent magnet on the stator is expressed by:

$$F^{st}(\theta) = \sum_{l=1}^{\infty} A_l^{st} \cos\left\{(2l-1) N_s \theta\right\} \tag{2.17}$$

$$A_l^{st} = \frac{B_r}{\mu_0 l N_s} r_p^{st} h_m^{st} \frac{\sin\left(\frac{l\pi r_p^{st}}{2}\right)}{\frac{l\pi r_p^{st}}{2}} \tag{2.18}$$

where $r_o^{st}$ is the ratio of the permanent magnet length to the stator pitch, which is 0.5 in this model. $N_s$ is the number of the stator teeth, and $h_m^{st}$ is the thickness of the permanent magnet on the stator teeth.

To express the influence of the permanent magnet on the high-speed rotor, the magnetic field is obtained by the product between the air gap permeance by the stator teeth and the magnetomotive force by the high-speed rotor magnet. Therefore, the air gap permeance function $P^{st}(\theta)$ of the stator teeth can be obtained by

$$P^{st}(\theta) = P_0^{st} + \sum_{k=1}^{\infty} P_k^{st} \cos\left\{(2k-1) N_s \theta\right\} \tag{2.19}$$

$$P_0^{st} = \frac{\mu_0}{K_c^{st} g_e^{st}} \left(1 - 1.6 \beta^{st} r_o^{st}\right) \tag{2.20}$$

$$g_e^{st} = 2g + l_{lsr} + \frac{h_m^{st}}{\mu_r} \tag{2.21}$$

$$P_k^{st} = \frac{4}{k\pi} \frac{\mu_0}{g_e^{out}} \beta^{st} \left[ 0.5 + \frac{\left(i r_o^{st}\right)^2}{0.78125 - 2\left(i r_o^{st}\right)^2} \right] \sin\left(1.6\pi i r_o^{st}\right) \tag{2.22}$$

$$K_c^{st} = \left[ 1 - \frac{2}{\pi} r_o^{st} \left\{ \tan^{-1}\left(\frac{b_0^{st}}{g_e^{st}}\right) - \frac{g_e^{st}}{b_0^{st}} \ln\left[ 1 + \frac{1}{4}\left(\frac{b_0^{st}}{g_e^{st}}\right)\right]\right\}\right]^{-1} \tag{2.23}$$

$$\beta^{st} = \frac{1}{2} + \frac{1}{2\sqrt{1 + \left(\frac{t_s^{st} r_o^{st}}{2 g_e^{st}}\right)}} \tag{2.24}$$

where $g_e^{st}$ is the effective air gap length obtained as the sum of the inner and outer air gaps and the length of the low-speed rotor. Other coefficients are calculated by applying the stator teeth in the process described above. Finally, the magnetic flux

density in the outer air gap can be obtained as the sum of the products between the magnetomotive force due to the permanent magnet and the air gap permeance of the low-speed rotor teeth, and between the magnetomotive force of the high-speed rotor magnet and the air gap permeance of the stator teeth as follows:

$$
\begin{aligned}
&B^{outer}\left(\theta,\delta,\gamma\right)=F^{st}\left(\theta\right)P^{out}(\theta+\delta)+F^{hsr}\left(\theta+\gamma\right)P^{st}(\theta)\\
&=\sum_{l=1}^{\infty}A_l^{st}P_0^{out}\cos\left\{\left(2l-1\right)N_s\theta\right\}+\sum_{j=1}^{\infty}A_j^{hsr}P_0^{st}\cos\left\{\left(2j-1\right)N_h\left(\theta+\gamma\right)\right\}\\
&+\sum_{l=1}^{\infty}\sum_{i=1}^{\infty}\frac{A_l^{st}P_i^{out}}{2}\times\left[\begin{array}{l}\cos\left[\left\{\left(2l-1\right)N_s+\left(2i-1\right)N_l\right\}\left\{\theta+\dfrac{\left(2i-1\right)N_l\delta}{\left(2l-1\right)N_s+\left(2i-1\right)N_l}\right\}\right]\\+\cos\left[\left\{\left(2l-1\right)N_s-\left(2i-1\right)N_l\right\}\left\{\theta+\dfrac{\left(2i-1\right)N_l\delta}{\left(2l-1\right)N_s-\left(2i-1\right)N_l}\right\}\right]\end{array}\right]\\
&+\sum_{j=1}^{\infty}\sum_{k=1}^{\infty}\frac{A_j^{hsr}P_k^{st}}{2}\times\left[\begin{array}{l}\cos\left[\left\{\left(2j-1\right)N_h+\left(2k-1\right)N_s\right\}\left\{\theta+\dfrac{\left(2j-1\right)N_h\gamma}{\left(2j-1\right)N_h+\left(2k-1\right)N_s}\right\}\right]\\+\cos\left[\left\{\left(2j-1\right)N_h-\left(2k-1\right)N_s\right\}\left\{\theta+\dfrac{\left(2j-1\right)N_h\gamma}{\left(2j-1\right)N_h-\left(2k-1\right)N_s}\right\}\right]\end{array}\right]
\end{aligned}
\tag{2.25}
$$

### 2.2.3 Back EMF and Torque

In the case of a three-phase surface permanent synchronous motor, the general torque equation is as follows:

$$T_e=\frac{P}{\omega_m}=\frac{e_u i_u+e_v i_v+e_w i_w}{\omega_m} \tag{2.26}$$

where $P$ is the power, $\omega_m$ is the rotor speed in $rad/s$, $e$ and $i$ are the back electromotive force(EMF) and current of each phase, respectively.

For a conventional surface permanent magnet synchronous motor, the back EMF is the derivate of the flux linkage waveform. However, since magnetic geared motors have a geared effect, they contain a coefficient $k_r$ when calculating the back EMF. The phase back EMF of a magnetic geared motor can be obtained by:

$$e_{ph}=\frac{d\lambda}{dt}=\frac{d\theta_m}{dt}\frac{d\lambda}{d\theta_m}=k_r\omega_m\frac{d\lambda}{d\theta_m} \tag{2.27}$$

$$k_r = k_{hsr}^{lsr} \cdot k_{stator}^{lsr} \tag{2.28}$$

$$k_{lsr}^{hsr} = \frac{N_l}{N_h} \tag{2.29}$$

$$k_{stator}^{lsr} = \frac{N_l}{N_s} \tag{2.30}$$

where $k_{lsr}^{hsr}$ and $k_{stator}^{lsr}$ are the ratio of the number of the low-speed and high-speed rotor poles, and the ratio of the number of the low-speed rotor poles and the stator teeth. Therefore, the back EMF of a magnetic geared motor can be redefined by:

$$\begin{aligned} e_{ph} &= \frac{d\lambda}{dt} = \frac{d\theta_m}{dt}\frac{d\lambda}{d\theta_m} = k_r k_w \omega_m \frac{d\lambda}{d\theta_m} \\ &= k_r k_w \frac{N_h}{2} \omega_m \frac{2N\phi}{\pi} \\ &\approx k_r k_w \frac{N_h}{2} \omega_m \frac{2N}{\pi}\left(\frac{2\pi}{N_h} B_{g1} L_{stk} R_{ro}\right) \\ &\approx 2k_r k_w \omega_m N B_{g1} L_{stk} R_{ro} \end{aligned} \tag{2.31}$$

where $\theta_m$ is the mechanical angle, $k_w$ is the winding factor, $L_{stk}$ is the stack length, $R_{ro}$ is the outer radius of the low-speed rotor, $\phi$ and $B_{g1}$ are the harmonic flux and the amplitude of the 5th harmonics of the magnetic flux density in the outer air gap, respectively. Finally, the torque equation can be obtained by:

$$T_e = \frac{3}{2}\frac{e_{ph} i_{ph}}{\omega_m} \approx 3k_r k_w N B_{g1} L_{stk} R_{ro} i_{ph} \tag{2.32}$$

## 2.3 Finite Element Method Verification

The 2-D finite element method was used to compare the magnetic flux density in the inner and outer air gaps with the analytical calculation. To compare the results of the 2-D FEM and the analytical calculation, a magnetic geared motor was designed with the same dimensions and the parameters are listed in Table 1. In the FEM analysis, JMAG Designer 17.1.01za (JSOL Corporation) was used, and the N-T characteristics were obtained through a coupled analysis of MATLAB 7.5.0.342 (R2007b) and JMAG.

TABLE I

MAIN DESIGN PARAMETER

| Item | Unit | Value |
|---|---|---|
| $N_h$ | | 5 |
| $N_l$ | | 17 |
| $N_s$ | | 12 |
| Gear ratio | | 3.4 |
| Stator outside radius | [mm] | R40 |
| Stator inside radius | [mm] | R27 |
| Low-speed rotor length | [mm] | 5.5 |
| High-speed rotor outside radius | [mm] | R20.5 |
| Magnet thickness | [mm] | 3 |
| Stack length | [mm] | 30 |
| Air gap length | [mm] | 0.5 |
| Slot opening ratio | | 0.5 |
| Magnet material | | N42SH |
| Steel sheet | | 50A400 |

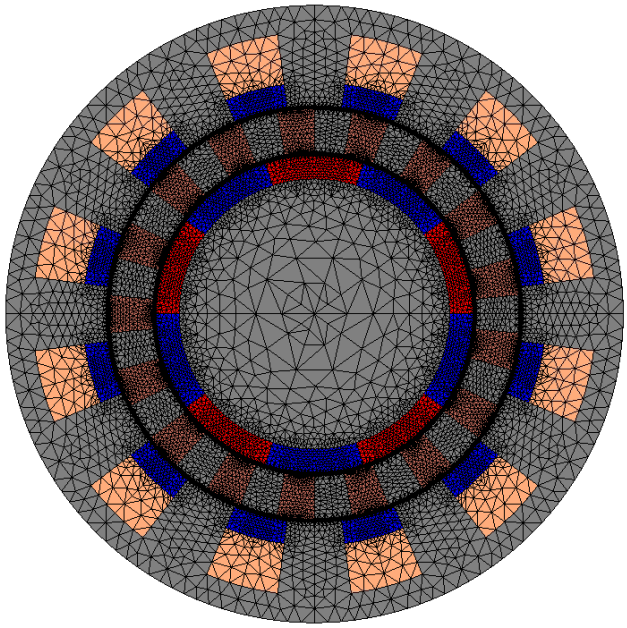

Fig. 2.4. Mesh model of magnetic geared motor

A mesh model of the magnetic geared motor is shown in Fig. 2.4. A control block diagram and the analysis conditions are shown in Fig. 2.5 and Table II, respectively. The number of nodes and elements are 21,265 and 32,422, respectively. In this section, the magnetic flux density and the space harmonics distribution in the inner and outer air gaps are shown and compared through the result of the 2-D FEM and analytical calculation. The magnetic flux density and the space harmonics distribution in the inner air gap at $t = 0$ are shown in Fig. 2.6. It can be seen that the analytical calculation method shows a good agreement with the 2-D FEM.

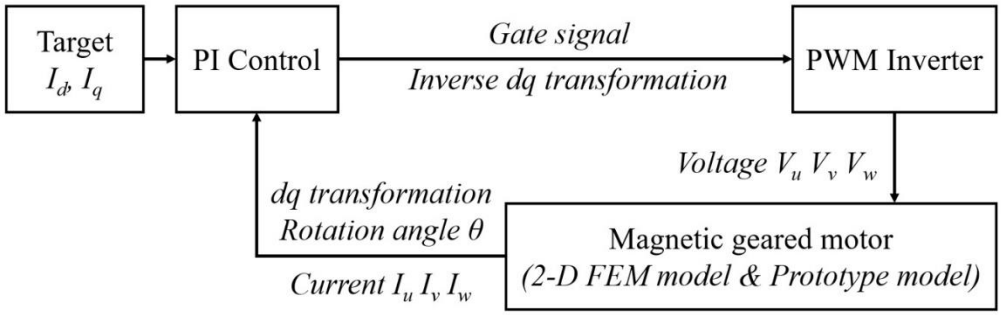


Fig. 2.5. Control block diagram

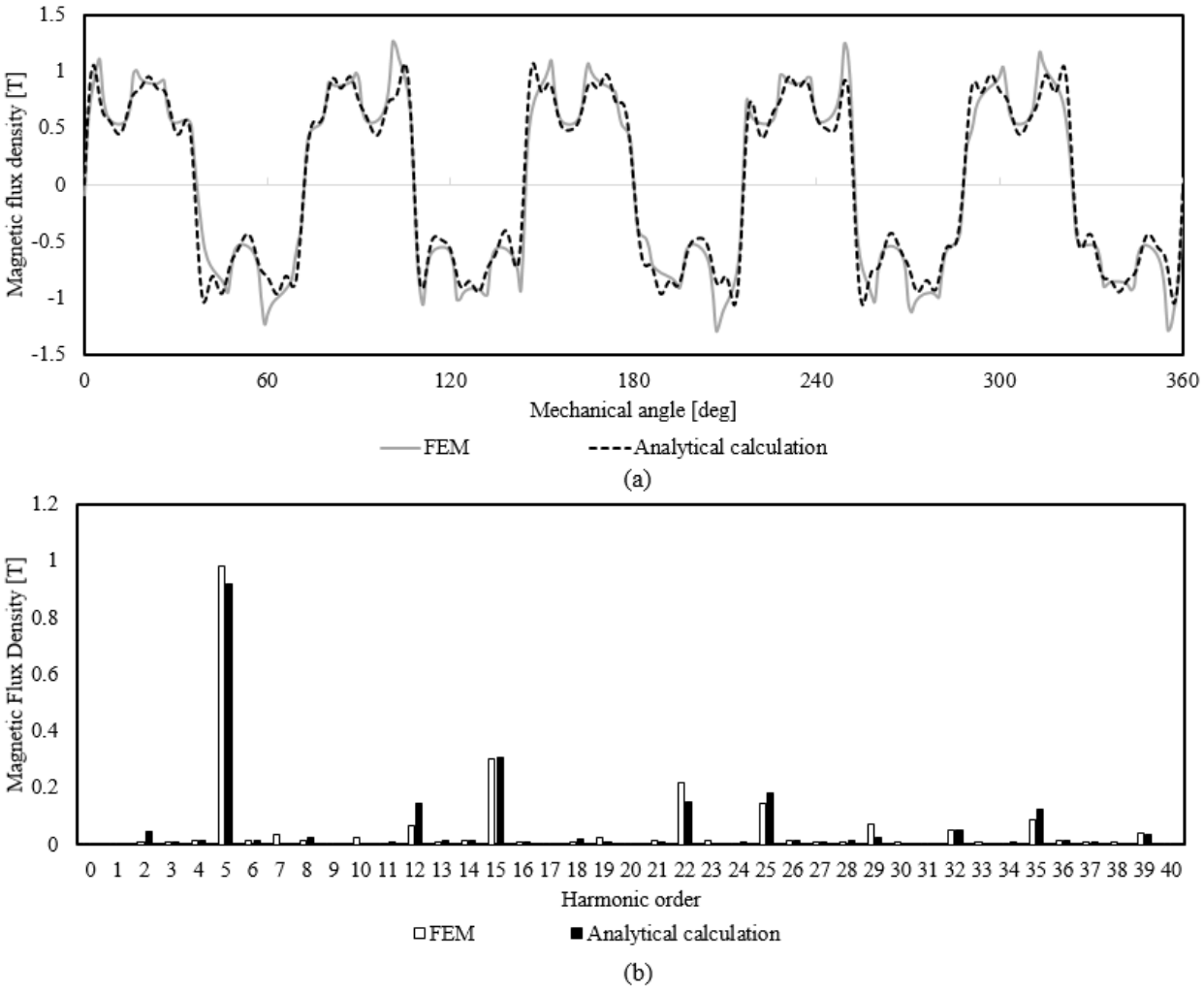


Fig. 2.6. Comparison of FEM and the analytical calculations in the inner air gap flux density waveform and space harmonics. (a) flux density distribution. (b) space harmonics

TABLE II

ANALYSIS CONDITION

| Item | Value |
|---|---|
| Carrier frequency | 20kHz |
| Control period | 2$\mu s$ |
| Time step | 2$\mu s$ |
| Target $I_d$ | 0A |
| Power supply | 12V |

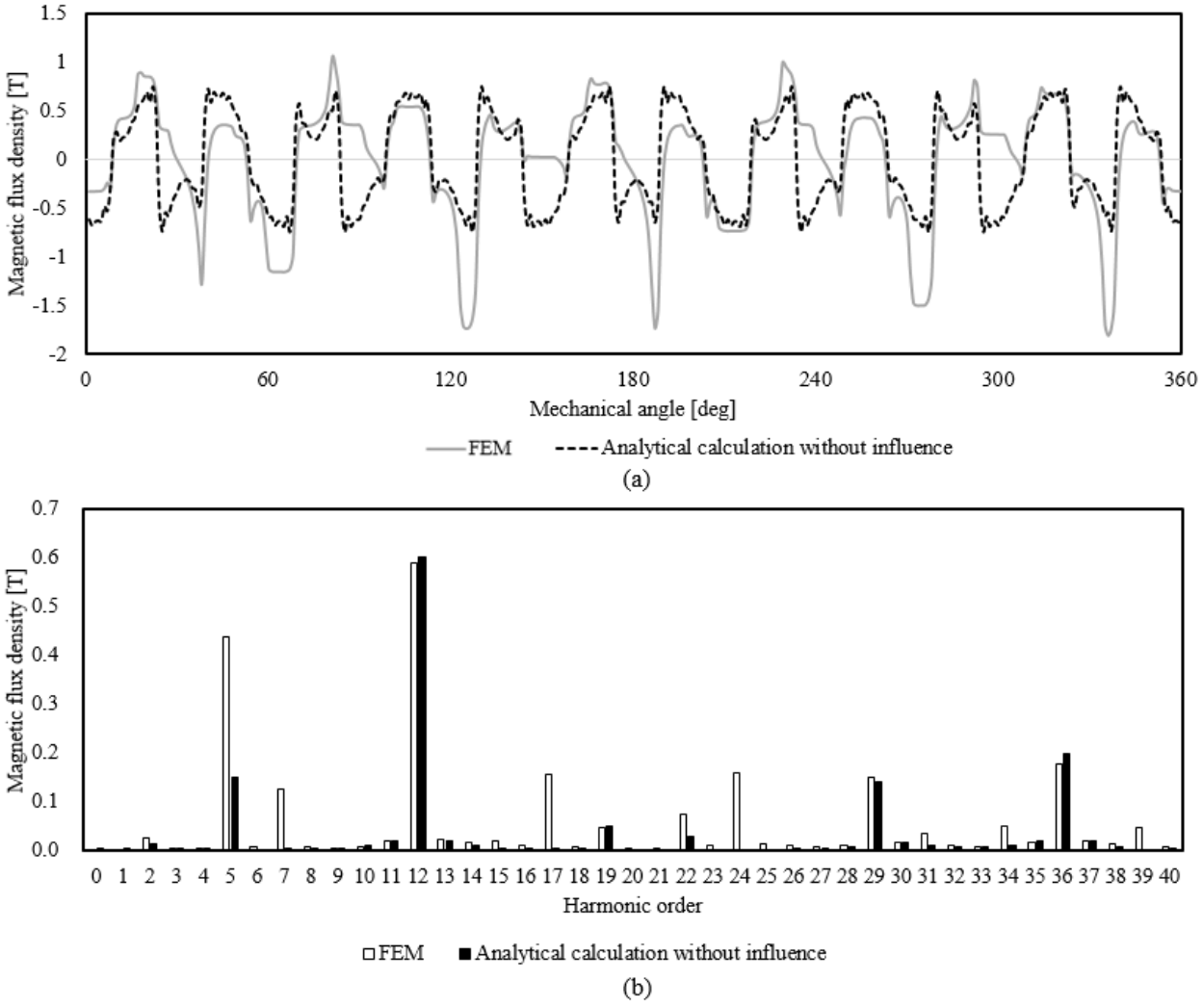


Fig. 2.7. Comparison of FEM and the analytical calculations without influence of the high-speed rotor magnet in the outer air gap flux density waveform and space harmonics. (a) flux density distribution. (b) space harmonics

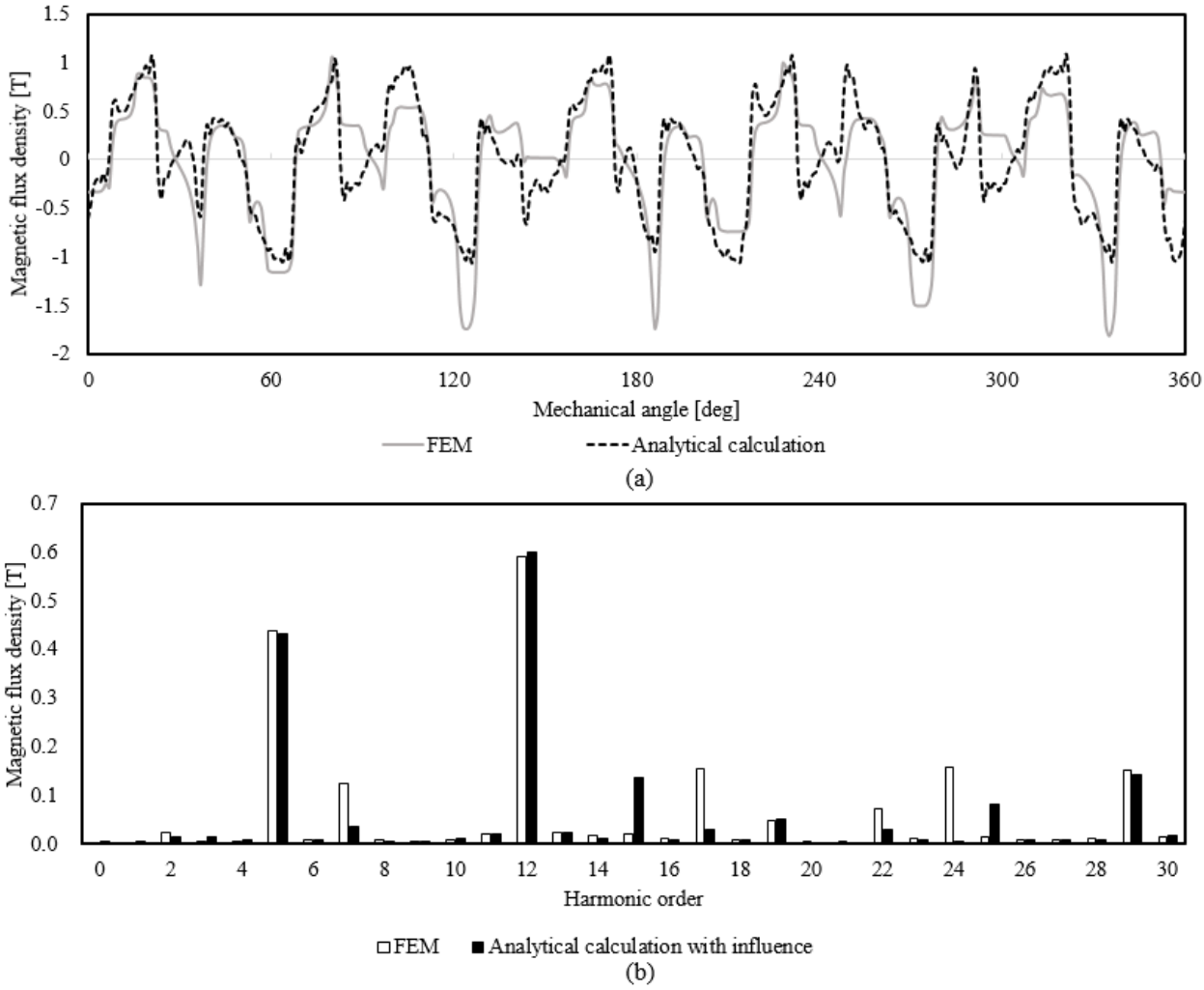


Fig. 2.8. Comparison of FEM and the analytical calculations with influence of the high-speed rotor magnet in the outer air gap flux density waveform and space harmonics.

(a) flux density distribution. (b) space harmonics

Fig. 2.7 compares the results of FEM with the analytical calculation results of the outer air gap magnetic flux density, which does not reflect the permanent magnet of the high-speed rotor. Fig. 2.7 (a) shows a similar pattern. However, in the space harmonic graph of (b), the fifth order component shows a large difference in the FEM results.

Fig. 2.8 shows the analytical calculation result with the influence of the high-speed

rotor permanent magnet when calculating the magnetic flux density of the outer air gap. In Fig. 2.8(a), there is a slight difference between these results. This is due to the fact that the influence of the permeability of the low-speed rotor is not reflected in the calculation of the outer gap. However, it can be seen from Fig. 2.8(b) that the amplitudes of the major 5th and 12th order harmonics used to drive the magnetic geared motor are very similar. This is demonstrated through analysis calculations that reflect the high-speed rotor permanent magnet and the air gap permeability of the stator teeth. To obtain more accurate results, it can be estimated that the effect of the permeability of the low-speed rotor teeth should be used in analyzing the influence of the high-speed rotor permanent magnet.

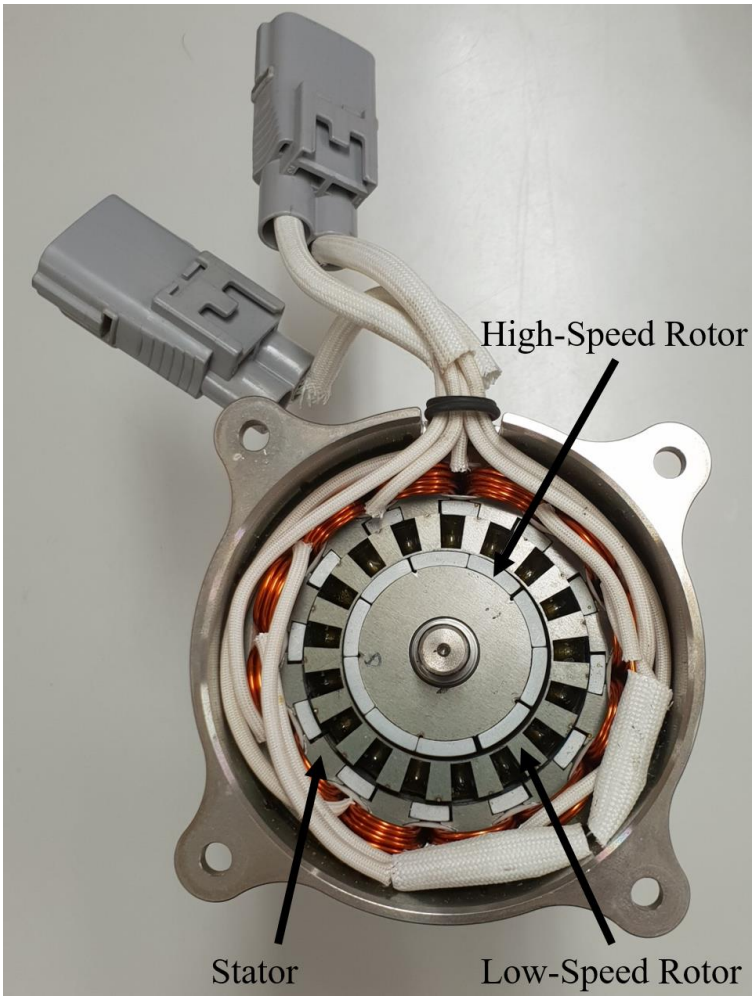


Fig. 2.9 Prototype of the magnetic geared motor

## 2.4 Prototype Model

In order to validate the analytical calculation, a prototype of the magnetic geared motor has been manufactured as shown in Fig. 2.9. The prototype was designed based on the dimensions in TABLE.I In the driving test, the maximum transmission torque and the back EMF were measured. Then the N-T characteristics were analyzed by driving the motor under loads. Like the coupled analysis, the prototype was tested based on the control block shown in Fig. 2.5 and TABLE II. Finally, the measured results were compared and evaluated with the FEM and analytical calculation.

The EMF waveforms were computed and measured when the low-speed rotor was rotated at a speed of 500 rpm. The results of the back-EMF were compared among the analytical calculation, the measured prototype and the FEM as shown in Fig. 2.10. The EMF results of the analytical calculations show a good agreement with the prototype measurements but show a slight discrepancy with the FEM. It seems that the back

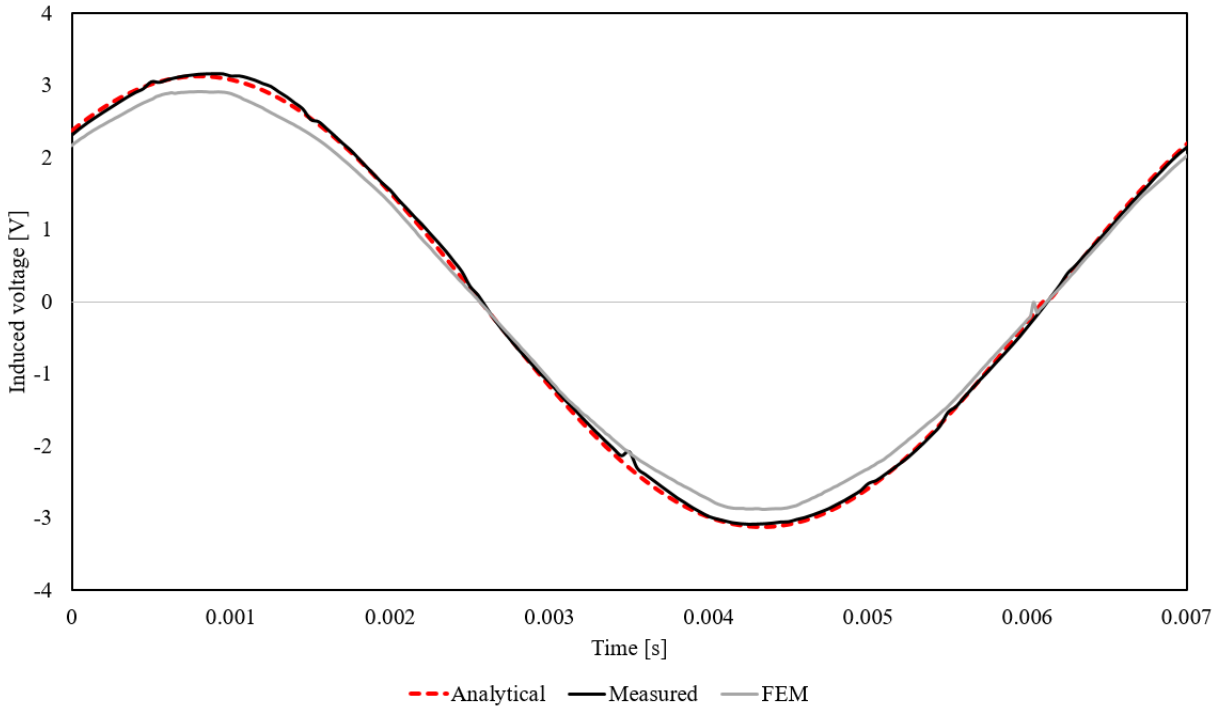


Fig. 2.10. Comparison of the phase back-EMF among the analytical calculation, the measured prototype and the FEM

EMF constant is lowered due to magnetic saturation phenomenon in the FEM calculations.

Fig. 2.11 shows a comparison of the maximum transmission torque of the FEM and the prototype when the high-speed rotor was rotated with the low-speed rotor fixed. The maximum transmission torques of the FEM and the prototype are 2.286Nm and 1.937Nm in the high-speed rotor, and 7.546Nm and 6.692Nm in the low-speed rotor, respectively. Both of these results were lower than the FEM and distorted. It is

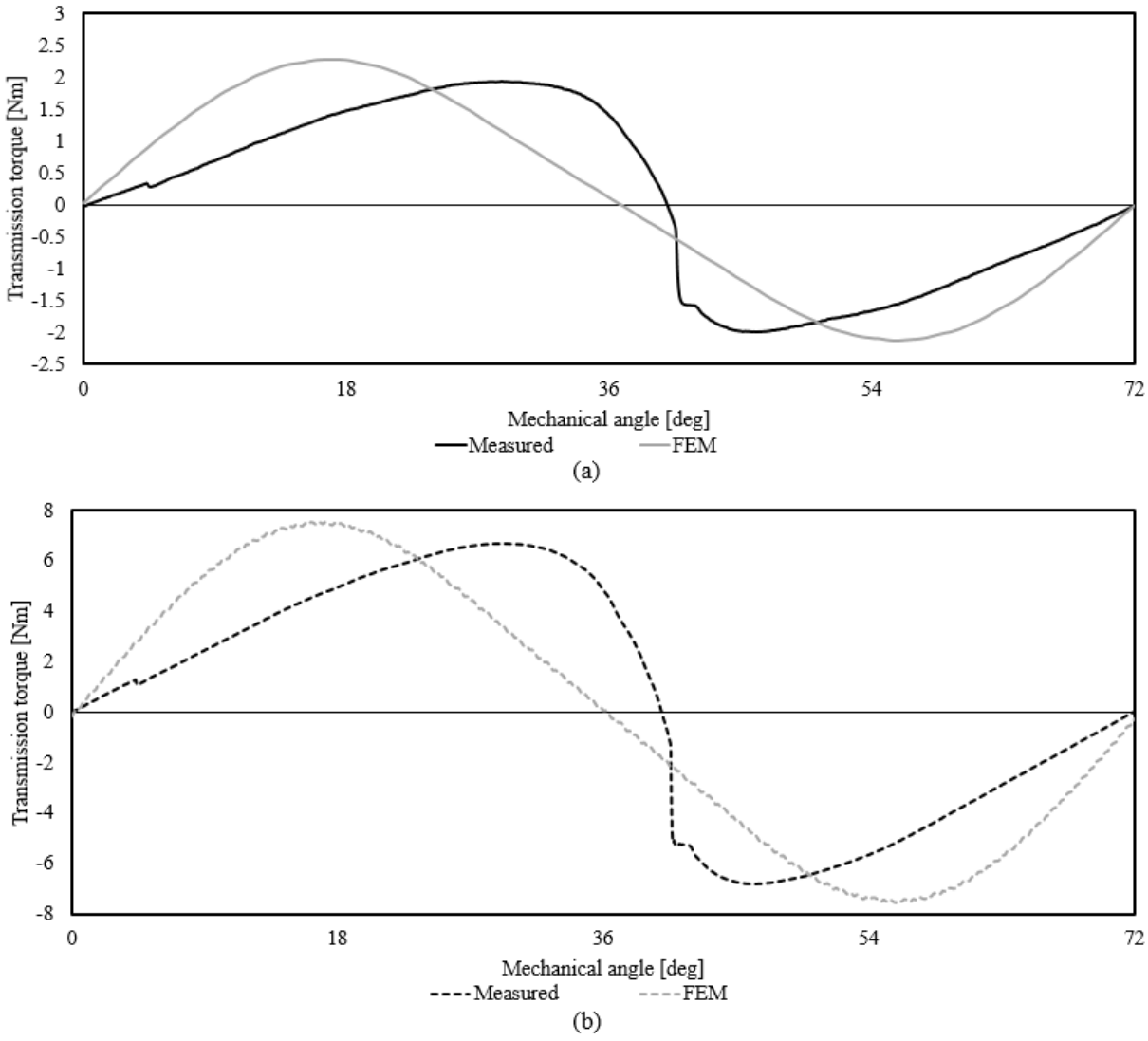


Fig. 2.11. Comparison of the maximum transmission torque between the FEM and the measured prototype (a) High-speed rotor, (b) Low-speed rotor

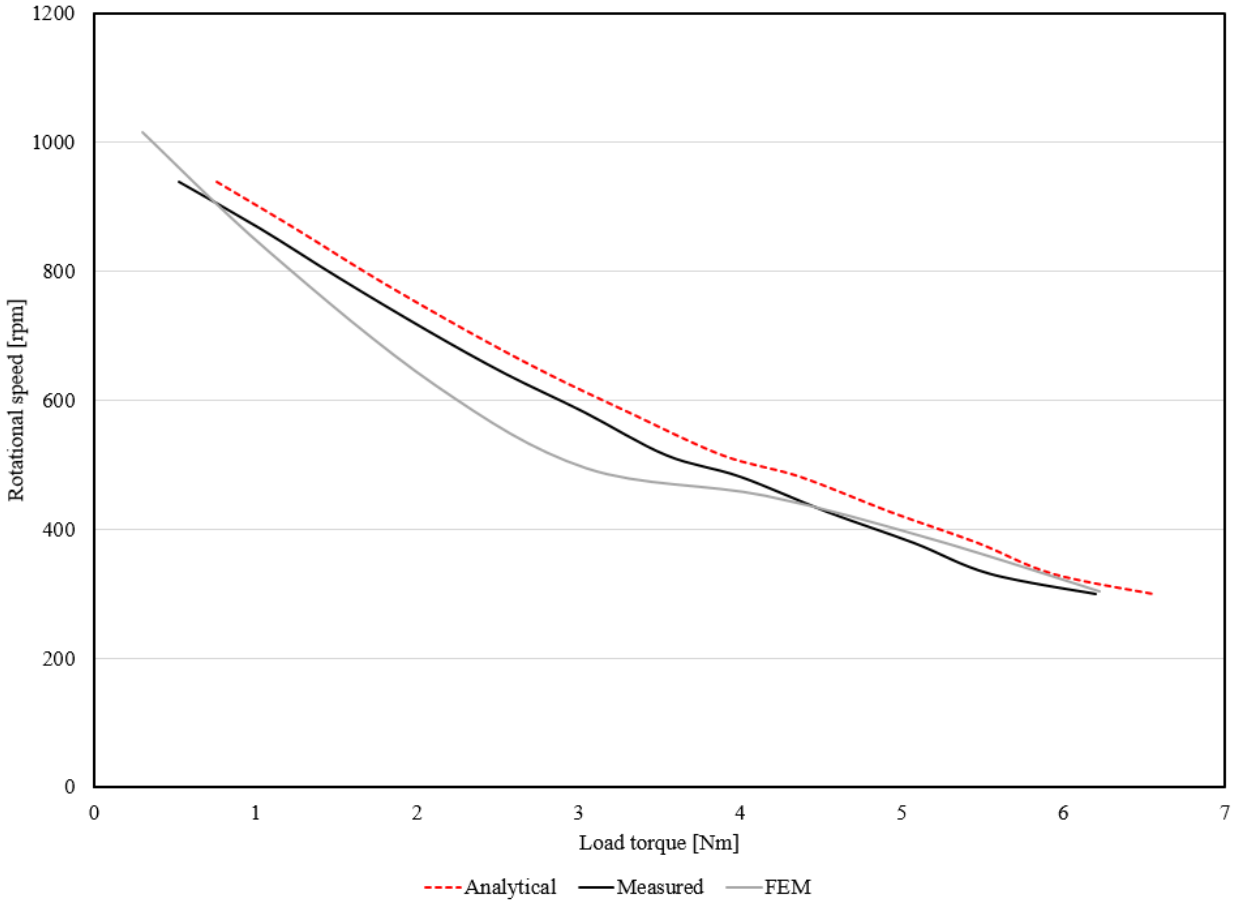


Fig. 2.12. Comparison of the N-T characteristics between the analytical calculation, the measured prototype and the FEM

considered that a measurement error causes the brake of the slip on the low-speed rotor during measurement. Fig. 2.12 shows the comparison of the torque versus the speed curves of the experiments, the FEM and the analytical calculation. A good agreement can be seen between the measured and the analytical approaches. However, the FEM results show a significant difference in the range of 2 Nm to 3 Nm when compared to the analytical result. This is considered to be caused by ignoring the iron losses such as the eddy current and hysteresis when calculating in the FEM.

## 2.5 Conclusion

This paper expressed an analytical calculation that can be used to effectively and

quickly analyze the N-T characteristics of a magnetic geared motor. Results such as a magnetic flux density in the inner and outer air gaps, the back-EMF and the N-T characteristics were verified and compared with the FEM and experiment on a prototype model. The analytical calculation method showed a good agreement with both the FEM results and the experimental results obtained from the prototype model. In future works, an efficient design method by searching for the optimal design parameters using this calculation method will be proposed.

# Chapter 3 Mathematical Modeling for vernier motor

## 3.1 Introduction

In recent years, vernier motors have become an issue of increasing importance in the field of industrial electric machines[41-45] The vernier motor is a kind of electric motors with a magnetic gear effect and has high torque characteristics at low speeds without mechanical gears. The vernier motor also has various advantages such as low noises and maintenance-free operations. The surface permanent magnet vernier motor is operated using space harmonics of the magnetic flux density distribution in the air gap which is created by the magnetomotive force (MMF) due to the permanent magnet and air gap permeance. Therefore, it is necessary to examine the design parameters such as a slot opening ratio and permanent magnet thickness which determine the amplitudes and the orders of the harmonics of the magnetic flux density. In order to determine the number of poles of the correct vernier motor, a comparative analysis of the effect of the pole ratio and windings pole number is required.

This chapter presents an analytical calculation method of the vernier motors, and their results are compared with those of finite-elements method (FEM).

Firstly, the operational principle of the surface permanent magnet vernier motor and the magnetic flux density in the air gap are described in detail. Secondly, the harmonics of the magnetic flux density in the air gap are analyzed according to the design parameters. Next, the best design parameters are determined, and the 2-D FEM results verify the analytical calculation method. Then, the characteristics of the surface permanent magnet vernier motor in accordance with various pole ratios are analyzed by the 2-D FEM. Finally, to verify the usefulness of the proposed design method, a linear vernier motor is designed and compared with the existing proposed model to

evaluate its superiority.

## 3.2 Operational Principle of Surface Permanent Magnet Vernier Motor

A surface permanent magnet vernier motor has the same operational principle as a magnetic gear and is operated using space harmonics of the magnetic flux density in the air gap. The magnetic flux in the air gap can be represented by the product of the air gap permeance due to the stator teeth and the MMF due to the permanent magnet in the rotor. An SPMVM with 17 pole pairs and 18 stator slots shown in Fig. 3.1 is used in an analytical calculation, and its main design parameters are listed in TABLE I.

### 3.2.1 Air gap Permeance distribution

An analytical method for modeling the effect of stator slotting of a radial field brushless permanent magnet dc motor was presented in [38]. The air gap permeance

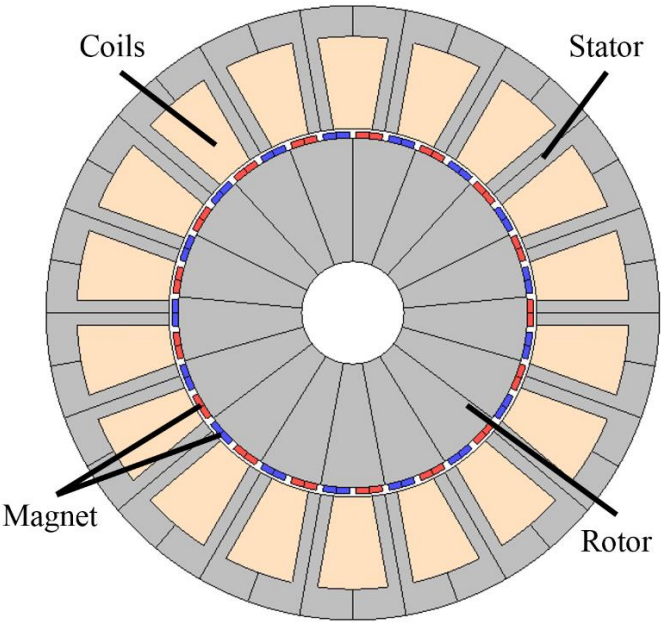


Fig. 3.1. 17-pole pairs 18-slots surface permanent magnet vernier motor

TABLE I
MAIN DESIGN PARAMETER

| Item | Unit | Value |
|---|---|---|
| Motor Type | | Vernier Motor |
| Operation type | | 240AC 3phase |
| Stator Outside Radius | [mm] | R85 |
| Stator Inside Radius | [mm] | R50 |
| Stator Yoke Thickness | [mm] | 8 |
| Stator Teeth Depth | [mm] | 27 |
| Air gap length | [mm] | 0.6 |
| Magnet thickness | [mm] | 2 |
| Rotor Outside Radius | [mm] | R49.4 |
| Rotor Inside Radius | [mm] | R10 |
| Stack length | [mm] | 130 |
| Magnet Material | | NMX-S52[1.45T] |
| Steel sheet | | 35JN210 |

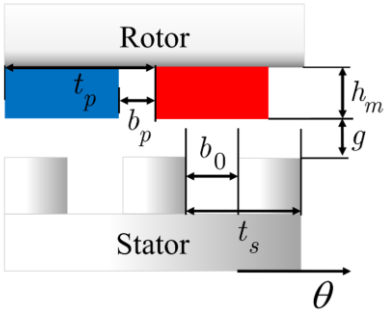


Fig. 3.2. Stator structure with slotting effect

of the stator teeth with the stator slotting effect shown Fig. 2 can be described by Fourier decomposition with a unit magnetic potential between the stator teeth and rotor permanent magnet. Therefore, the permeance function $P(\theta)$ of the stator teeth can be expressed in the following equation:

$$P(\theta) = P_0 + \sum_{i=1}^{\infty} P_i \cos(iN_s\theta) \tag{3.1}$$

where $N_s$ is the number of stator teeth. The coefficients $P_0$, $P_i$ in the permeance function can be obtained as follows:

$$P_0 = \frac{\mu_0}{K_c g'}\left(1-1.6\beta r_{open}\right) \tag{3.2}$$

$$g' = g + \frac{h_m}{\mu_r} \tag{3.3}$$

$$P_i = \frac{4}{i\pi}\frac{\mu_0}{g'}\beta\left[0.5+\frac{\left(ir_{open}\right)^2}{0.78125-2\left(ir_{open}\right)^2}\right]\sin\left(1.6\pi i r_{open}\right) \tag{3.4}$$

$$K_c = \left[1-\frac{2}{\pi}r_{open}\left\{\tan^{-1}\left(\frac{b_s}{g'}\right)-\frac{g'}{b_s}\ln\left[1+\frac{1}{4}\left(\frac{b_s}{g'}\right)\right]\right\}\right]^{-1} \tag{3.5}$$

$$\beta = \frac{1}{2}+\frac{1}{2\sqrt{1+\left(\frac{t_s r_{open}}{2g'}\right)^2}} \tag{3.6}$$

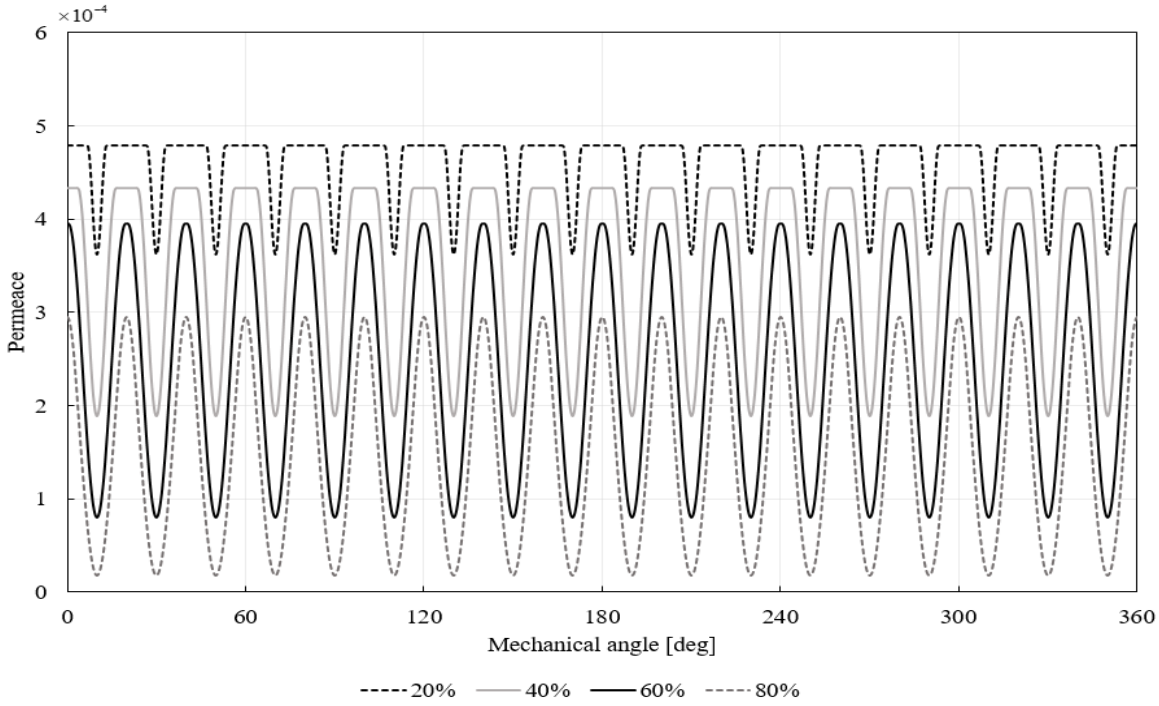


Fig. 3.3. Variation of air gap permeance waveform by analytical calculation according to slot opening ratio

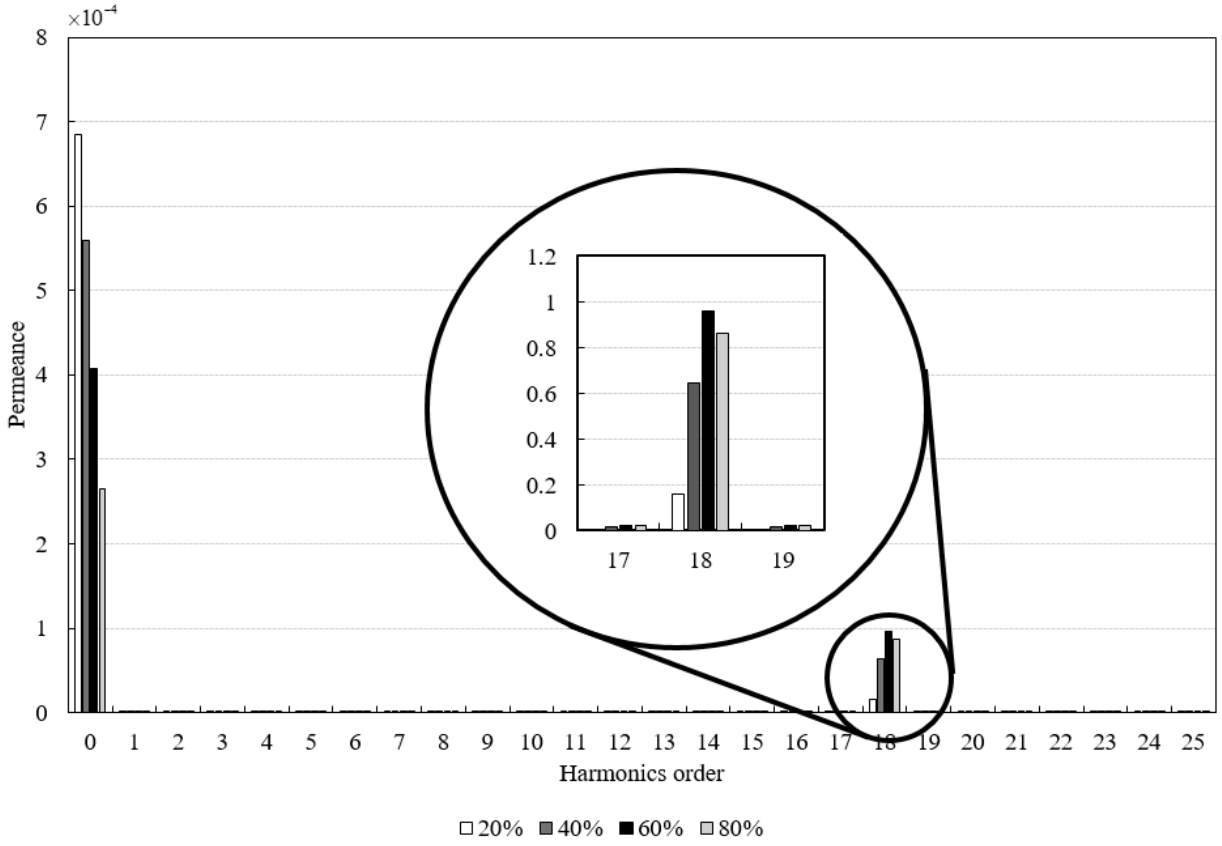


Fig. 3.4. Variation of air gap permeance spectra by analytical calculation according to slot opening ratio

where $r_{open}$ is the slot opening ratio of the slot opening length $b_s$ to the slot pitch $t_s$, $\mu_r$ and $\mu_0$ are the relative permeability of the stator and rotor yokes and the permeability of vacuum, respectively, $g$ is the air gap length and $h_m$ is the permanent magnet thickness as shown in Fig. 3.2. In (3.5), Carter's coefficient $K_c$ has been included to account for the increase of the effective air gap due to the stator slotting [40] and $g'$ is the replaced air gap length for the computation of Carter's coefficient.

Fig. 3.3 and Fig. 3.4 show the variation of the air gap permeance waveform and harmonic spectra. Fig. 3.3 shows that as the slot opening ratio increases, the average value and the shape of each waveform decreased and changes from a square to a sine, respectively. In (3.1), $P_0$ in the first term, and $P_i$ in the second term mean the average value and the amplitude of each waveform in Fig. 3.3. The harmonics spectra shown in Fig. 3.4 will be verified below.

### 3.2.2 Magnetomotive Force

The Fourier series expansion of the magnetomotive force due to the permanent magnet on the rotor is described by

$$F(\theta+\alpha)=\sum_{j=1}^{\infty}A_j\sin\{(2j-1)P_r(\theta+\alpha)\} \tag{3.7}$$

where $P_r$ is the number of pole pairs on the rotor. The coefficient $A_j$ of the MMF function is the magnetization, which is assumed to be uniform throughout the cross-section of the permanent magnets and is given by [39]

$$A_j=\frac{B_r}{\mu_0 jP_r}\alpha_p h_m\frac{\sin(\frac{j\pi\alpha_p}{2})}{\frac{j\pi\alpha_p}{2}} \tag{3.8}$$

where $B_r$ is the permanent magnet remanence, $\alpha_p$ is the ratio of the permanent magnet pole arc $b_p$ to the pole pitch $t_p$ as shown in Fig.3.2. Fig. 3.5 shows the

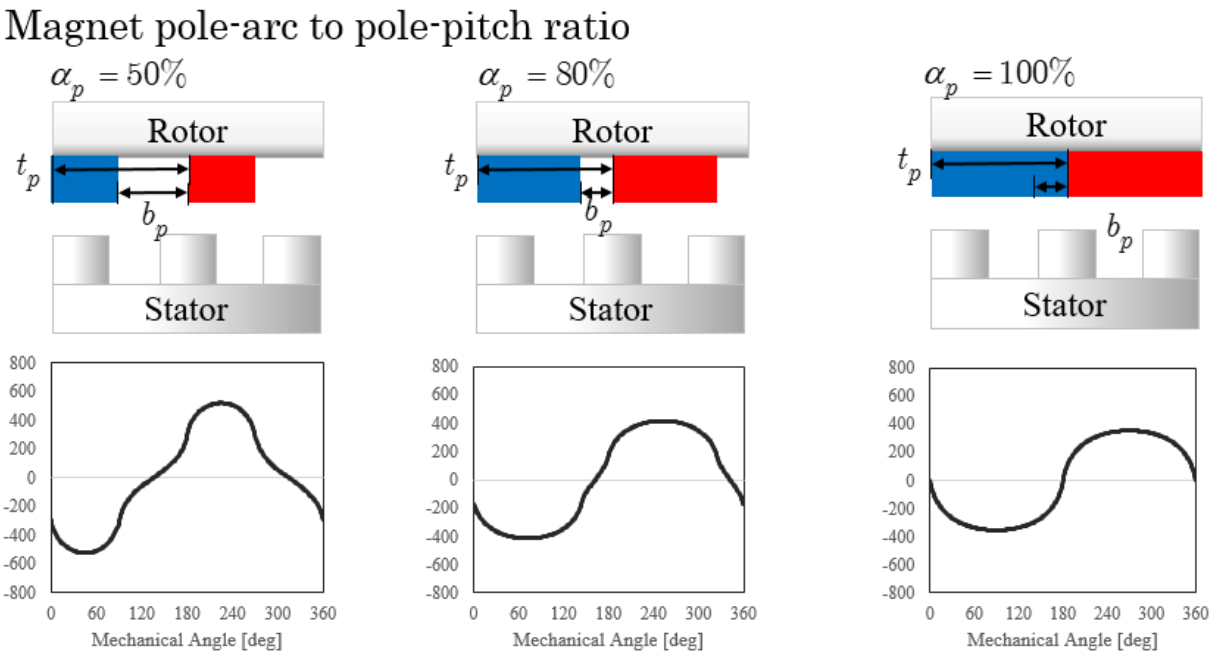


Fig. 3.5. Waveform changes of magnetomotive force according to magnet pole arc to pole-pitch ratio

waveform changes of magnetomotive force according to magnet pole arc to pole-pitch ratio $\alpha_p$.

### 3.2.3 Air gap Magnetic Flux Density

The air gap magnetic flux density distribution can be obtained by the product of the air gap permeance function $P(\theta)$ and the magnetomotive force function $F(\theta+\alpha)$ as shown in the following equation:

$$\begin{aligned} B(\theta,\alpha) &= P(\theta)F(\theta+\alpha) \\ &= \sum_{j=1}^{\infty} P_0 A_j \cos\{(2j-1)P_r(\theta+\alpha)\} \\ &+ \sum_{j=1}^{\infty}\sum_{i=1}^{\infty} P_i A_j \times \left[ \begin{array}{l} \cos\{iN_s-(2j-1)P_r\}\left\{\theta+\dfrac{(2j-1)P_r\alpha}{iN_s-(2j-1)P_r}\right\} \\ -\cos\{iN_s+(2j-1)P_r\}\left\{\theta+\dfrac{(2j-1)P_r\alpha}{iN_s+(2j-1)P_r}\right\} \end{array} \right] \end{aligned} \tag{3.9}$$

In (3.9), the magnetic flux distribution contains three primary harmonic components: 1 fundamental harmonic component $(2j-1)P_r$, and two harmonic components $iN_s \mp (2j-1)P_r$. The two harmonic components are created by the modulation of the permeance and MMF. Since a vernier motor is operated with a magnetically geared effect, the number of winding pole pairs of a vernier motor should be equal to either of the two harmonic components and can be obtained by

$$P_\omega = \left| iN_s \mp (2j-1)P_r \right| \tag{3.10}$$

The amplitude and rotation angle of 2 harmonic components are $P_i A_j$ and $(2j-1)P_r\alpha \big/ iN_s \mp 2j-1\ P_r$, respectively. $P_i$ is one of the parameters determining the amplitude of the harmonic order of the flux density. Therefore, as shown in Fig. 3.4, the amplitude of the 17th component corresponding to $P_i$ has a great influence on the harmonics of the permanent magnet flux density.

### 3.2.4 Back EMF and Torque

In the case of a three-phase surface permanent synchronous motor, the general torque equation is as follows:

$$T_e = \frac{P}{\omega_m} = \frac{e_u i_u + e_v i_v + e_w i_w}{\omega_m} \tag{3.11}$$

where $P$ is the power, $\omega_m$ is the rotor speed in $ras/s$, $e$ and $i$ are the back EMF and current of each phase, respectively. For a conventional surface permanent synchronous motor, the back EMF is the derivative of the flux linkage waveform. However, since the vernier motor has a different operational principle from a conventional surface permanent synchronous motor, the phase EMF can be obtained as follow:

$$e_{ph} = \frac{d\lambda}{dt} = \frac{d\theta_e}{dt}\frac{d\lambda}{d\theta_e} = k_r \omega_e \frac{d\lambda}{d\theta_e} \tag{3.12}$$

where $e_{ph}$ is the phase EMF, $\lambda$ is the flux linkage, $\theta_e$ is the electrical angle and $k_r$ is the ratio of the number of pole pairs of the permanent magnet to winding pole pairs. Substituting (3.9) into (3.12), the back EMF can be redefined by

$$\begin{aligned} e_{ph} &= \frac{d\lambda}{dt} = \frac{d\theta_e}{dt}\frac{d\lambda}{d\theta_e} = k_r k_w \omega_e \frac{d\lambda}{d\theta_e} = k_r k_w \frac{P_r}{2}\omega_m \frac{d\lambda}{d\theta_e} \\ &= k_r k_w \frac{P_r}{2}\omega_m \frac{2N\phi_g}{\pi} = k_r k_w \frac{P_r}{2}\omega_m \frac{2N}{\pi}\left(\frac{2\pi R_{ro} L_{stk}}{P_r} B_{g1}\right) \end{aligned} \tag{3.13}$$

where $\theta_m$ is the mechanical angle, $k_w$ is the winding factor, $L_{stk}$ is the stack length, $R_{ro}$ is the outer radius of the rotor, $\phi_g$ and $B_{g1}$ are the harmonic flux and flux density, respectively. The torque equation can be obtained by dividing (3.13) by the rotational speed and multiplying the current as follows,

$$\begin{aligned} T_e &= \frac{3}{2} e_{ph} i_{ph} \omega_m \\ &= \frac{3}{2} k_r k_w N R_{ro} L_{stk} B_{g1} i_{ph} \end{aligned} \tag{3.14}$$

## 3.3 Verification of Analytical Calculation

Assuming that $i$ and $j$ in (3.10) are 1, the 17-pole-pairs-18-slot vernier motor is driven using either of the first or 35th harmonics. In this study, the number of winding pole pairs is one because the first order harmonics are used. Based on the main design parameters listed in TABLE I, the SPMVM was designed as shown in Fig. 3.1. An FEM analysis was conducted to compare the analytical calculation result.

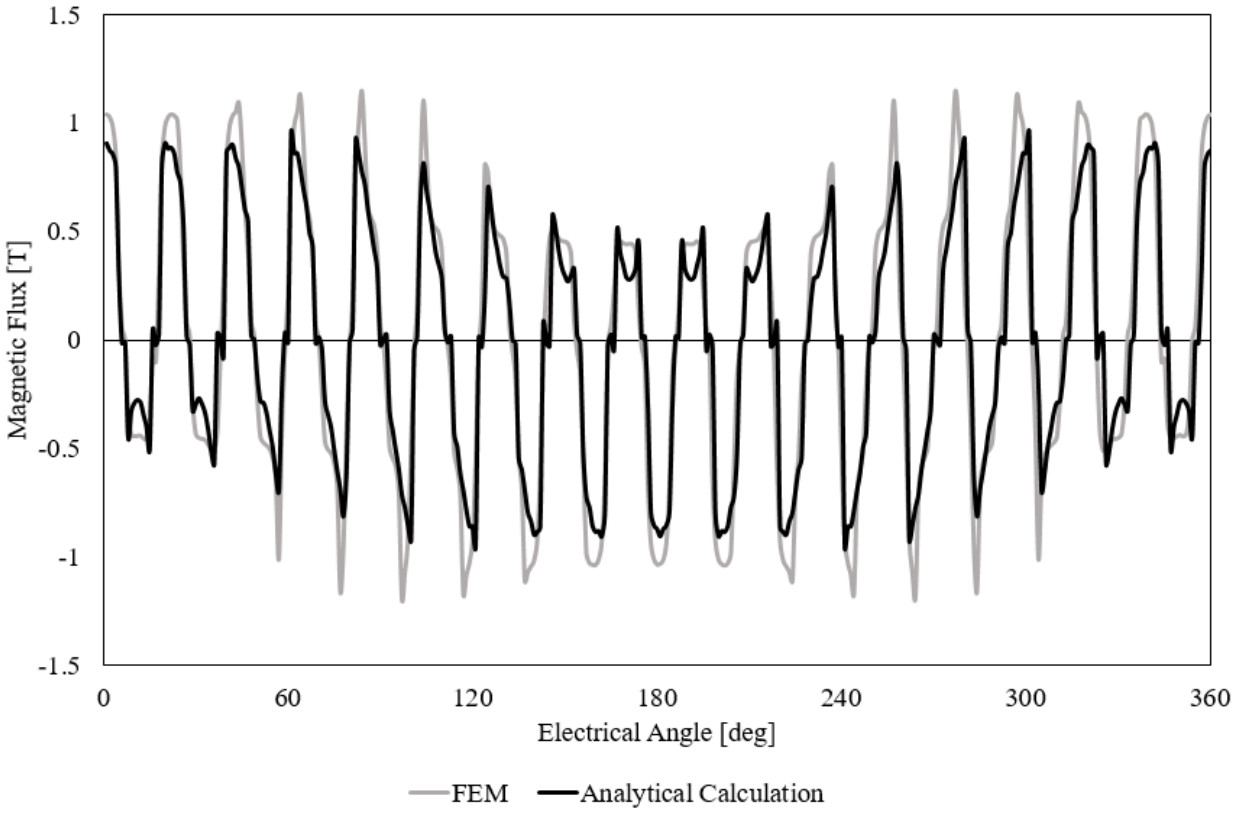


Fig. 3.6. Comparison of air gap magnetic flux density waveforms by 2-D FEM and analytical calculation

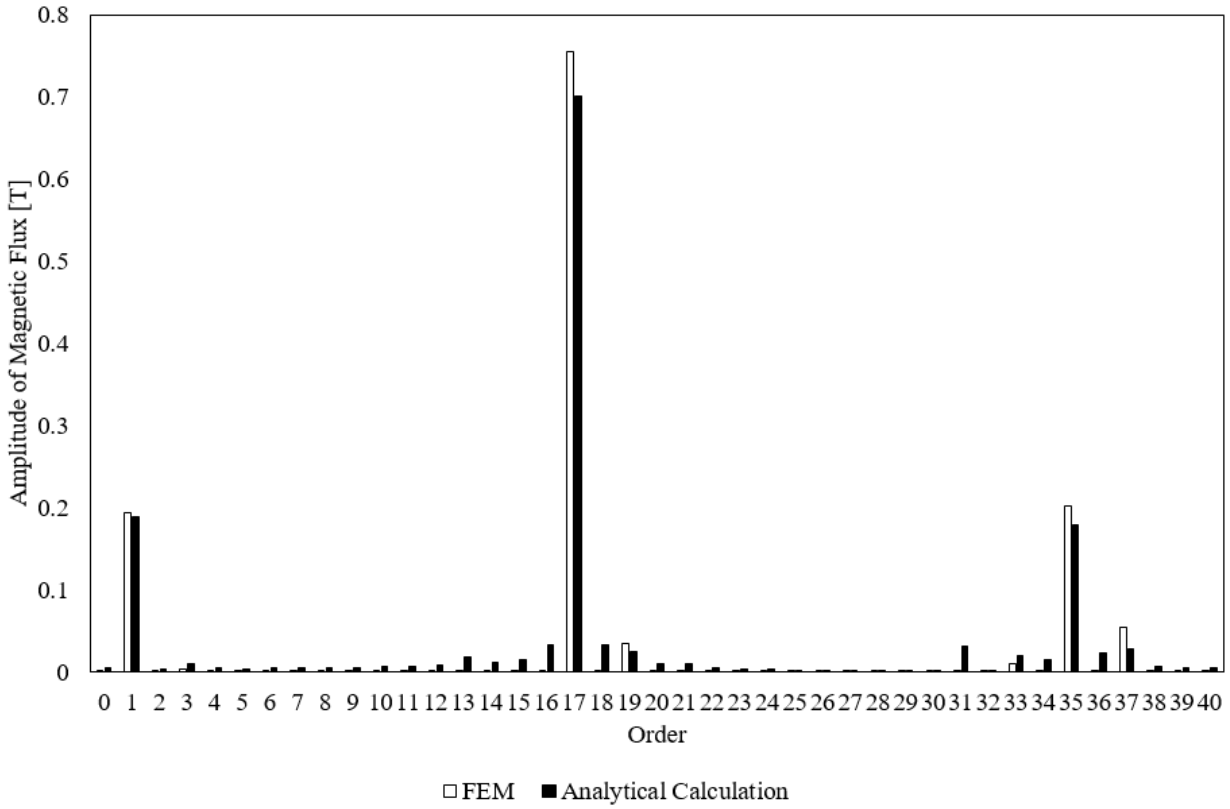


Fig. 3.7. Comparison of air gap magnetic flux density harmonics spectra by 2-D FEM and analytical calculation

### 3.3.1 Air gap magnetic flux density

Fig. 3.6 and Fig. 3.7 show the comparisons of the air gap magnetic flux density distribution and its harmonics spectra at t=0 sec. It can be seen that the shapes of the waveforms by the FEM and the analytical calculation look quite similar to each other in Fig. 3.6. The fundamental component 17th harmonic has the highest value, and the first and 35th harmonic components have the next highest value as shown in Fig. 3.7. As shown in Fig.3.7, the error rate between the FEM and analytical calculation method is within ±7.12%.

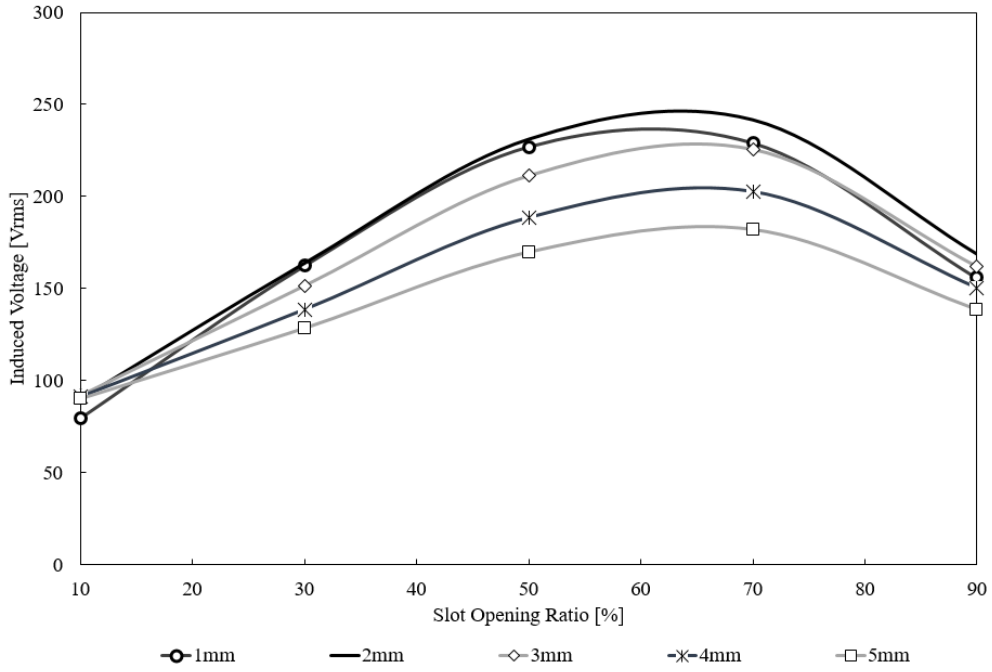


Fig. 3.8. Back EMF calculated by FEM according to the slot opening ratio and magnet thickness

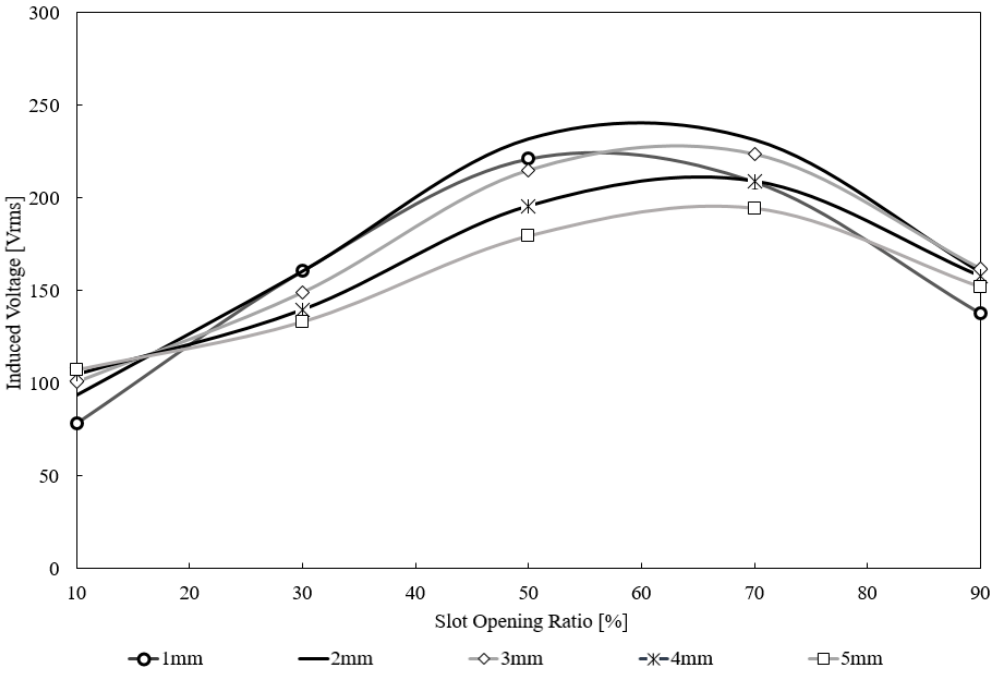


Fig. 3.9. Back EMF calculated by analytical calculation according to the slot opening ratio and magnet thickness

### 3.3.2 Back EMF

Fig. 3.8 and Fig. 3.9 illustrate the distribution of the back EMF root mean square (RMS) value according to the slot opening ratio and the permanent magnet thickness. Both graphs show a similar pattern, and when the opening ratio and permanent magnet thickness are 60% and 2mm, respectively, the highest induced voltages are observed in each graph.

### 3.3.3 Torque

As mentioned above, the opening ratio was fixed 60% and the output torque according to the permanent magnet thickness was analyzed when a three-phase current of 10 Arms was input, and the rotor was rotated at 500 rpm. Fig. 3.10 shows the trend line of the torque with the permanent magnet thickness change. Two lines showed an almost similar pattern and the model with 2-mm permanent magnet had the best output torque.

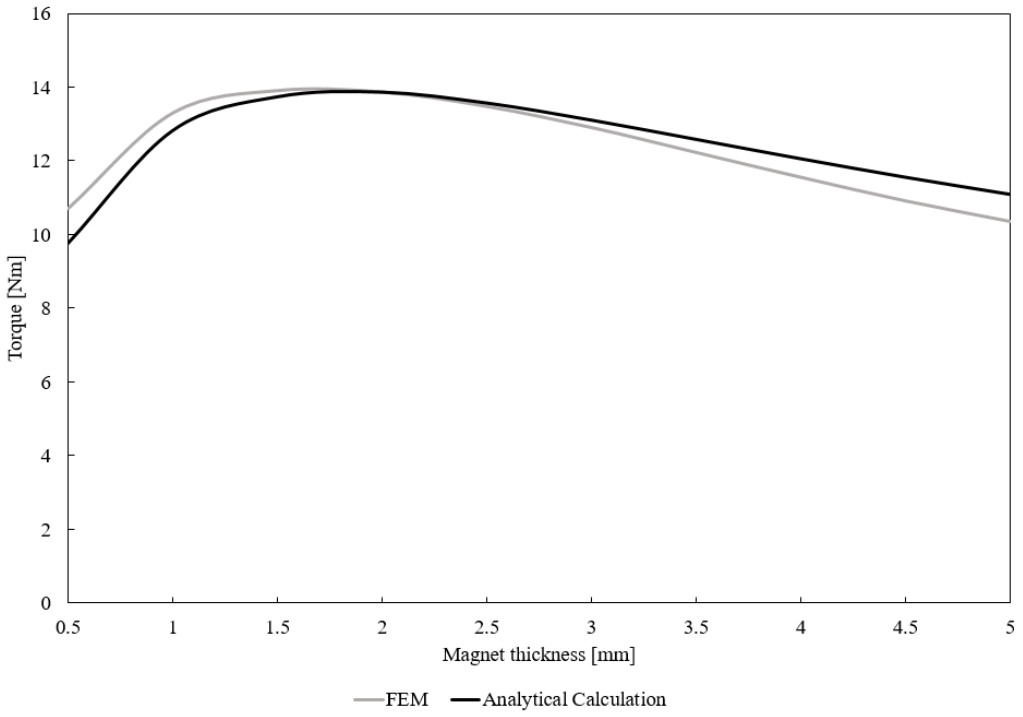


Fig. 3.10. Variation of output torque by FEM and analytical calculation

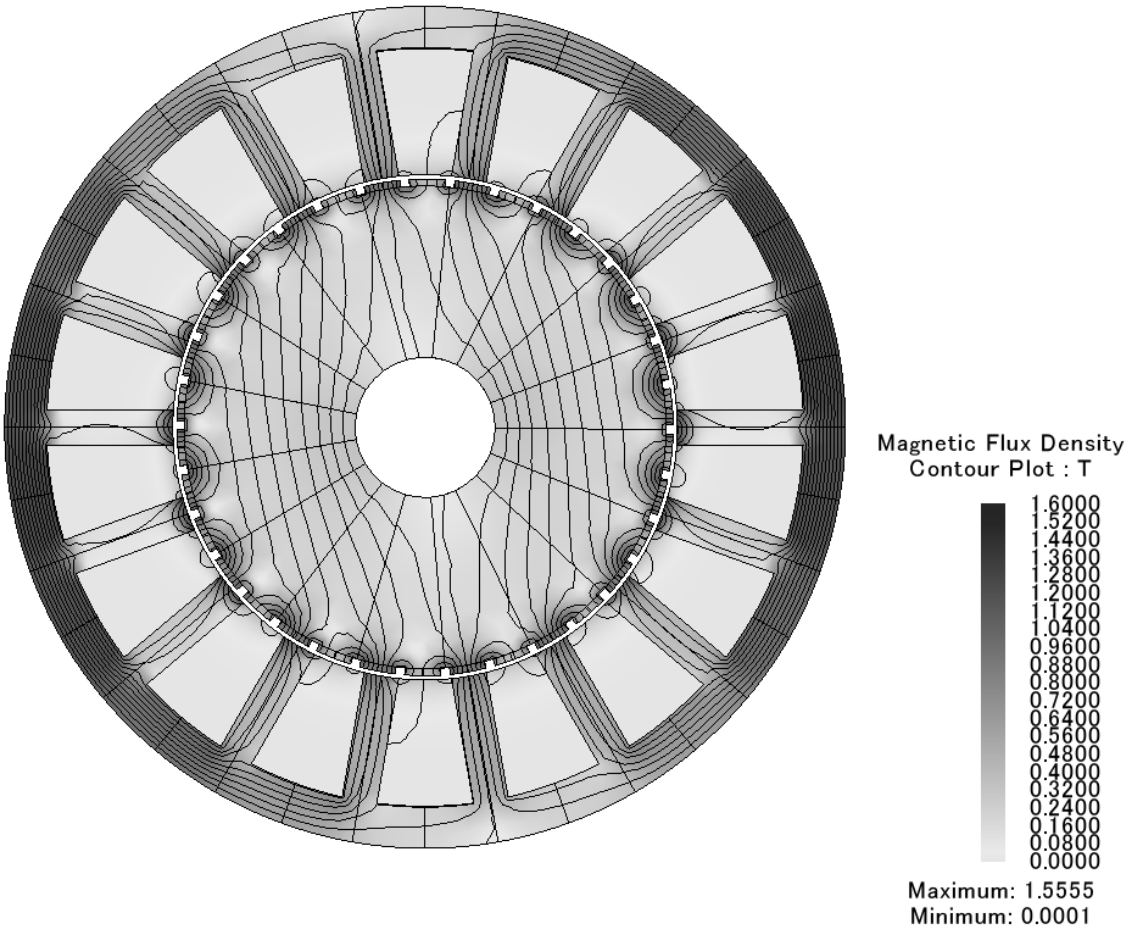


Fig. 3.11. FEM model of the designed surface permanent magnet vernier motor

### 3.3.4 N-T, T-I and T- η Characteristics

The N-T, T-I and the T-η characteristics of the SPMVM are computed using 2-D FEM. The 2-D FEM model of the SPMVM is shown in Fig. 3.11.

Fig. 3.12 and Fig. 3.13 showed the N-T and T-I characteristics when a sinusoidal voltage was supplied from 10 rpm to 500 rpm. The T-η characteristics are shown in Fig. 3.13 and the efficiency $\eta$ is given by

$$\eta = \frac{P_{out}}{P_{out} + W_{iron} + W_{copper}} \tag{3.15}$$

where $P_{out}$ is the output power, $W_{iron}$ is the iron loss of the laminated cores calculated

after FEM and $W_{copper}$ is the copper loss in the coils. As shown in Figs. 3.12 and 3.13, when the load torque is higher than 50 Nm, the efficiency is lower than 80%, and the current is greater than 20 Arms.

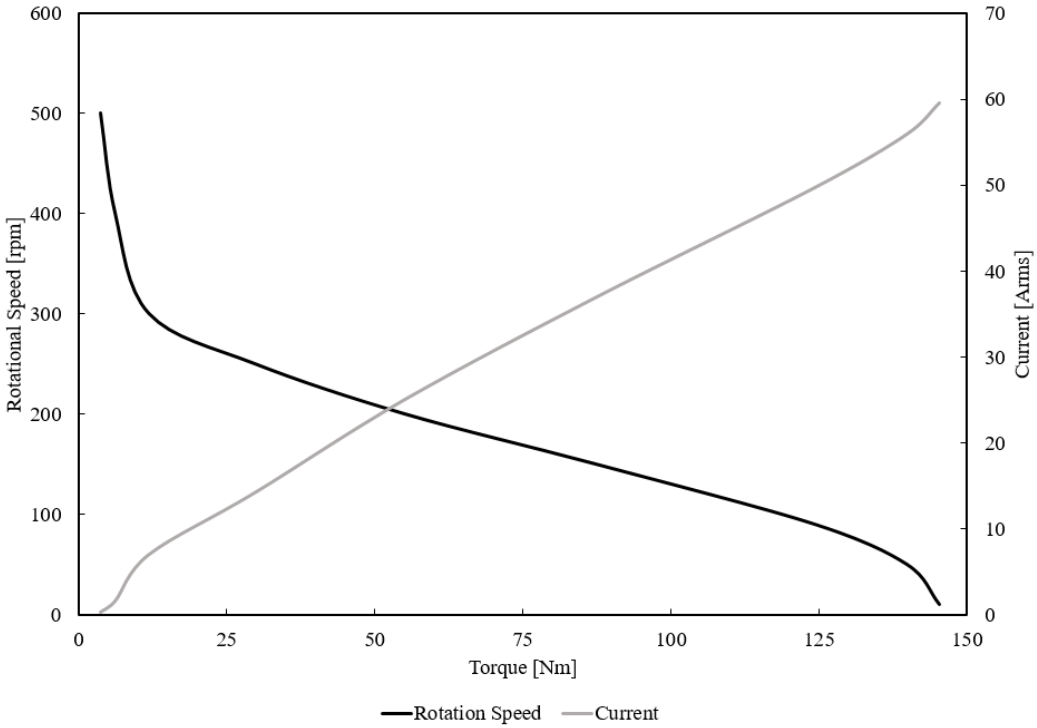


Fig. 3.12. N-T and T-I characteristics

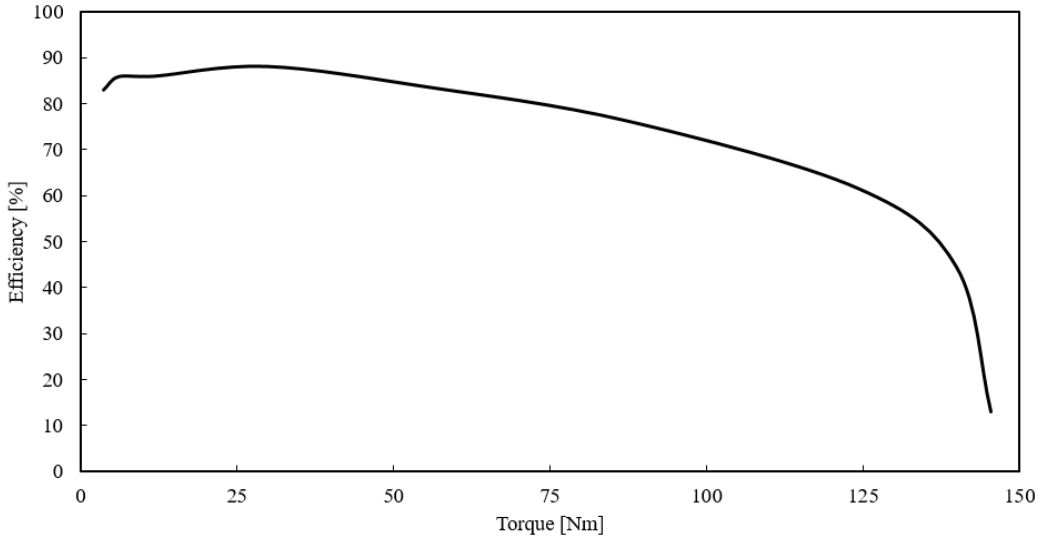


Fig. 3.13. T- η characteristics

### 3.3.5 Summary

Chapters 3.2 and 3.3 expressed an analytical calculation of an SPMVM with a stator slotting effect and designed a model based on a theoretical approach. An Analytical calculation method on how to calculate the air gap magnetic flux density and harmonics using an SPMVM operating principle was described. The analytical calculation method showed a good agreement with the FEM results. Finally, the characteristics of an SPMVM designed with the calculated design variables were verified using 2-D FEM analysis.

## 3.4 Design Procedure of Surface Permanent Magnet Vernier Motor

The design procedure of the surface permanent magnet type vernier motor can be refined step by step as mentioned in Chapters 3.2 and 3.3, as shown in Fig.3.14.

The first step in a machine design is not to calculate the machine size. However, to analyze specifications that provide essential information such as a machine's target performance and limits on external conditions. The next step is to determine the stator/rotor pole combination, the material of the permanent magnet and steel sheet and the length of the air gap before a motor design. A careful decision is needed because the performance and characteristics of the motor vary according to the configuration. Once the basic configuration is determined, the optimal detailed design parameters are obtained through an analytical calculation method. If the predicted performance and specifications do not match well, they are refined until the fixed values of the parameters match well at the beginning of the design.

Finally, the performance through FEM is evaluated. This process can be used to achieve a target performance through iterative loops.

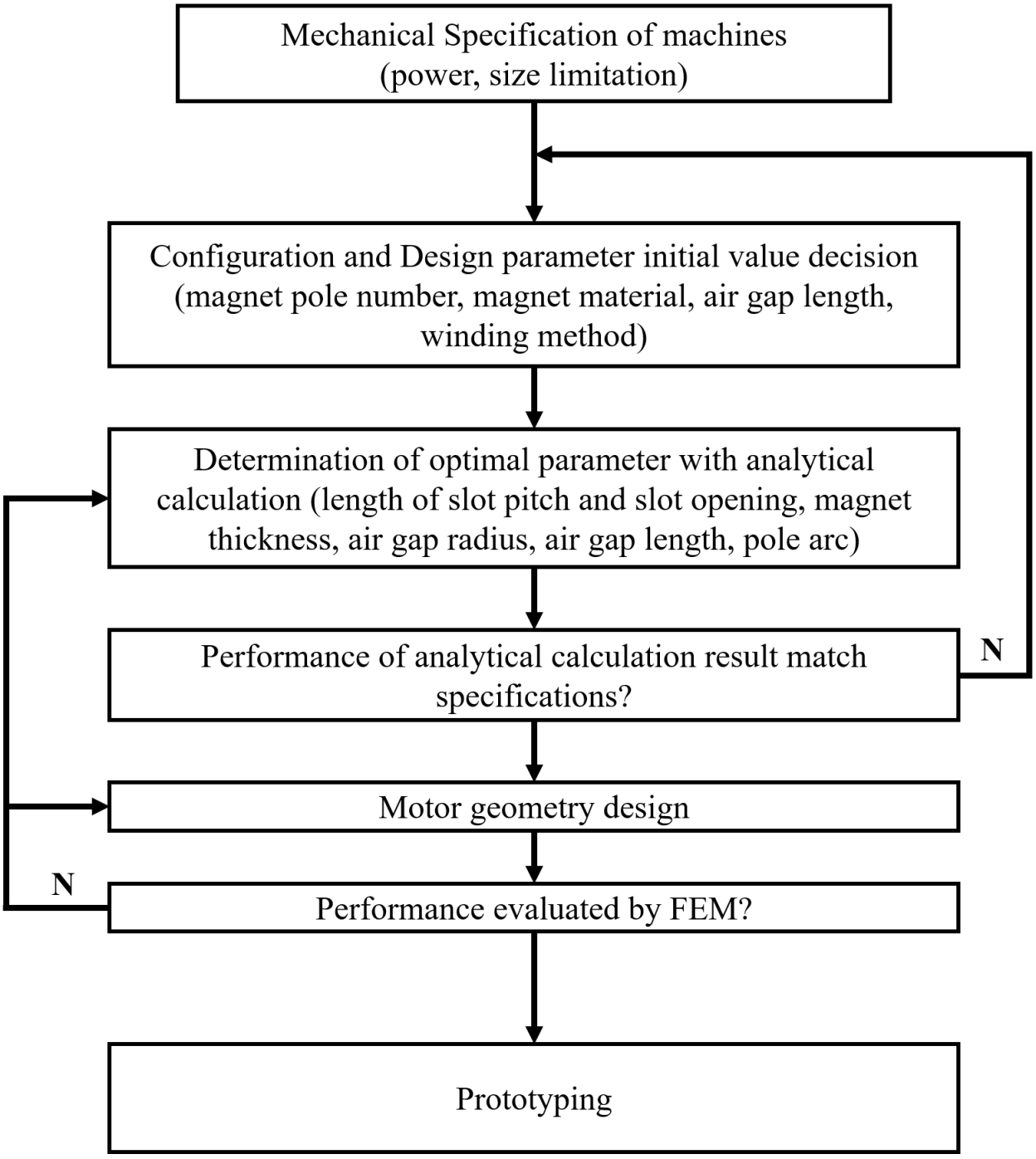


Fig. 3.14. Design procedure for surface permanent magnet vernier motor

## 3.5 Characteristics Analysis according to Pole Ratio and Winding Pole Number

In this chapter, first, models with various combinations are designed according to the design procedure in Fig. 3.14 based on TABLE III and 2-D FEM is performed. The characteristics of each model are analyzed by comparing the output results of not only a cogging torque and a torque ripple but also N-T and N-η characteristics. Table IV shows the combination of various numbers of permanent magnet pole pairs and stator teeth based on (3.10). The air-gap magnetic flux density and harmonic spectra of eight models are obtained by conducting an FEM analysis and the analytical calculation.

TABLE III

MAIN DESIGN PARAMETER

| Item | unit | value |
|---|---|---|
| Motor Type | | Vernier Motor |
| Operation type | | 240AC 3Phase |
| Stator Outside Radius | [mm] | R85 |
| Stator Inside Radius | [mm] | R50 |
| Stator Yoke Thickness | [mm] | 8 |
| Stator Teeth Depth | [mm] | 27 |
| air gap length | [mm] | 0.6 |
| Rotor Outside Radius | [mm] | R49.4 |
| Rotor Inside Radius | [mm] | R20 |
| Stack Length | [mm] | 130 |
| Magnet Material | | NMX-S52 [1.45T] |
| Steel sheet | | 35JN210 |

TABLE IV

COMBINATION OF POLE RATIO AND WINDING POLE NUMBER

| $N_s$ | $P_r$ | $P_\varnothing$ | Pole ratio | LCM |
|---|---|---|---|---|
| 12 | 10 | 2 | 5 | 60 |
| 12 | 11 | 1 | 11 | 132 |
| 15 | 14 | 1 | 14 | 210 |
| 18 | 16 | 2 | 8 | 144 |
| 18 | 17 | 1 | 17 | 306 |
| 21 | 20 | 1 | 20 | 420 |
| 24 | 22 | 2 | 11 | 264 |
| 24 | 23 | 1 | 23 | 552 |

The FEM results of each model are compared with the analytical analysis result. Fig. 3.15 shows the contours of the magnetic flux density of the FEM models. Fig. 3.16 shows the amplitude of the generated harmonic order of each compared model, respectively. As shown in Fig. 3.16, the error rate between the two methods is within ±11.52%.

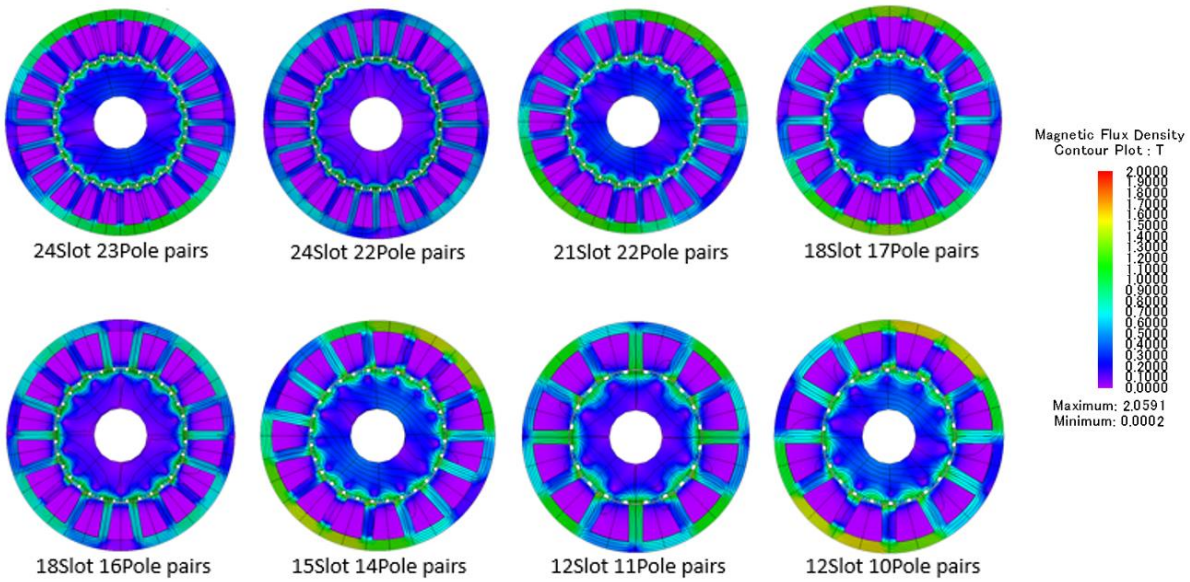


Fig. 3.15. FEM model with various combination

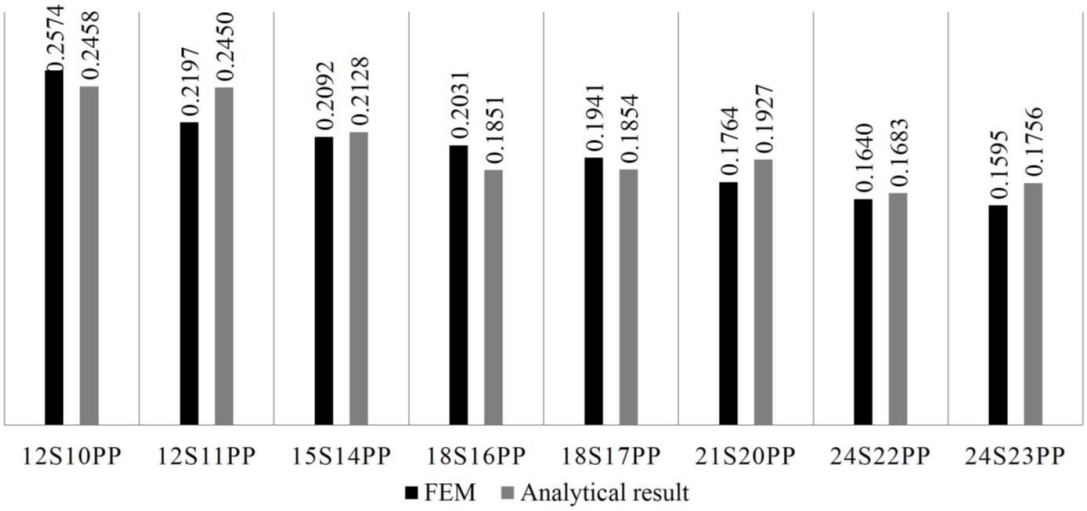


Fig. 3.16. Comparison of the amplitude of the generated harmonic order between the FEM and the analytical calculation in air-gap flux density

### 3.5.1 Cogging Torque and Torque ripple

In an electrical machine, the least common multiple (LCM) of the number of stator teeth and rotor pole pairs is known as a factor to affect its cogging torque and torque ripple. The LCMs of each model are listed in Table IV. Fig. 3.17 shows the cogging torque and torque ripple of each model. Models with 12 stators have a higher torque ripple and cogging torque than the others because their LCM is lower than the others as mentioned above. In addition, the waveforms of the cogging torque and torque ripple in Fig. 3.17 show similar trends.

### 3.5.2 Speed-Torque and Speed-Efficiency Characteristics

The N-T and N-η characteristics when a sinusoidal voltage was supplied from 50 to 500 rpm are analyzed and shown in Figs. 8 and 9. The efficiency $\eta$ is calculated using (3.15). Models of the 24S22PP, 18S16PP, and 12S10PP without a marker on the line in

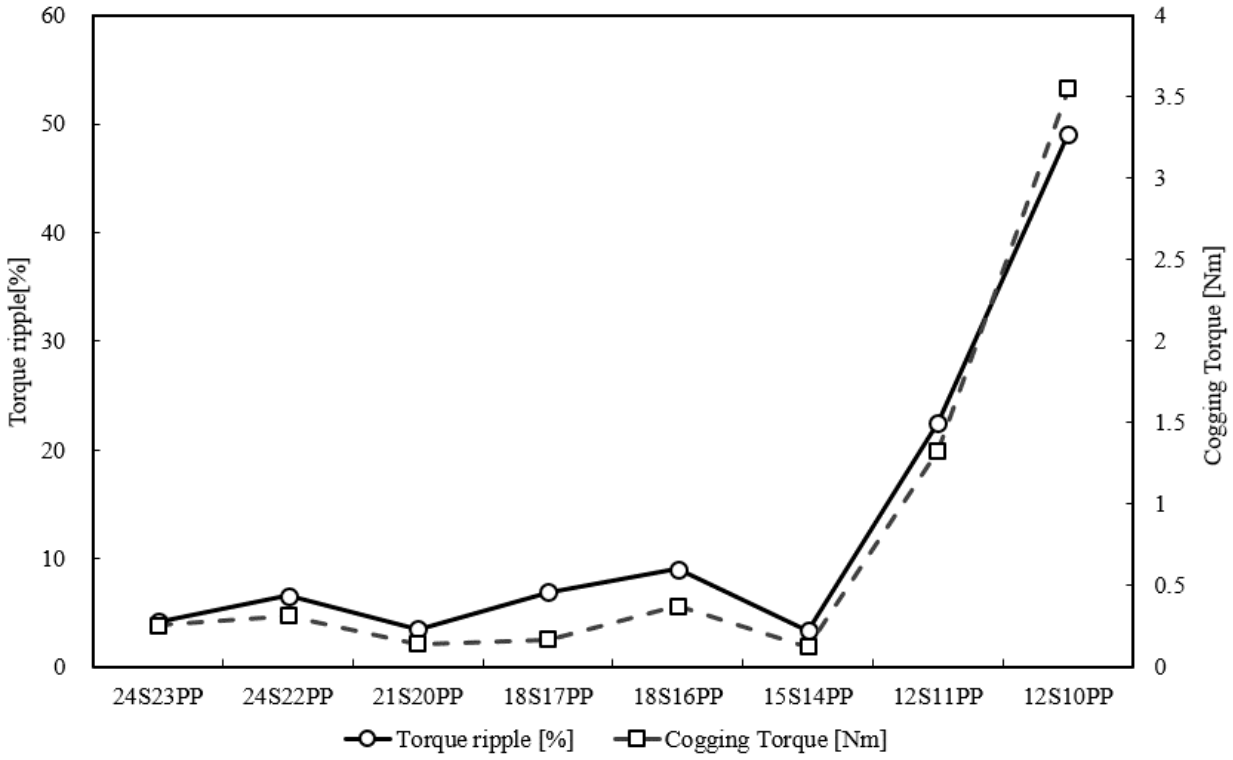


Fig. 3.17. Torque ripple and cogging torque

Fig. 3.18 and Fig. 3.19 show significantly higher output torque at low speeds and slightly higher efficiency at high speeds.

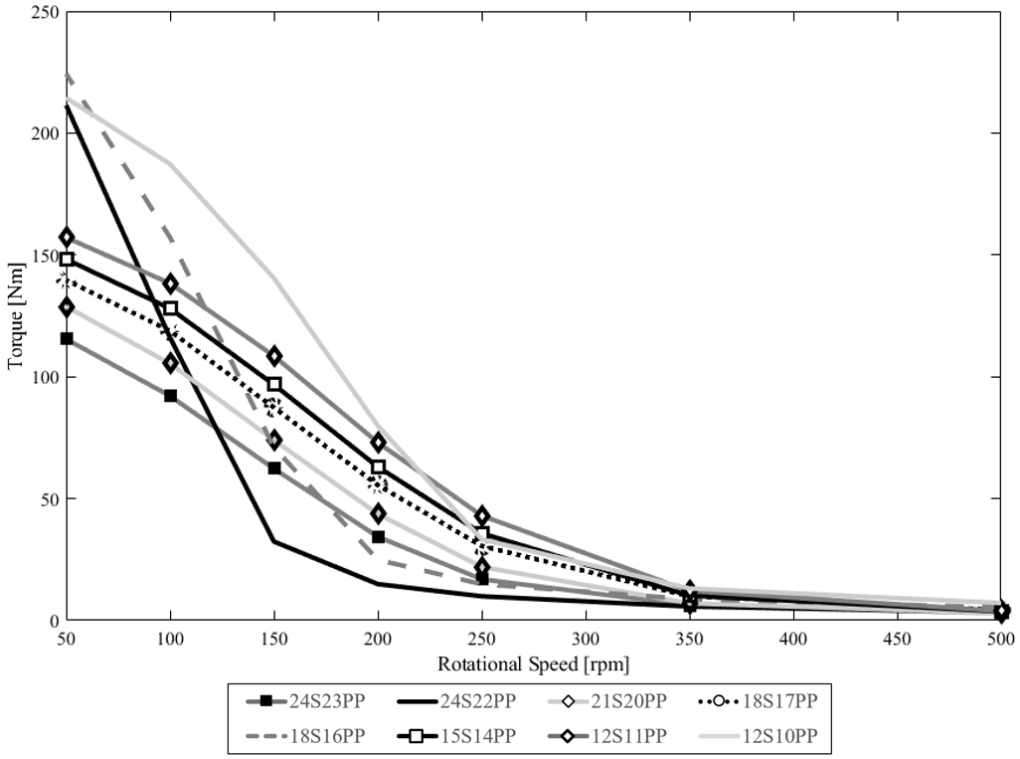


Fig. 3.18. N-T characteristics

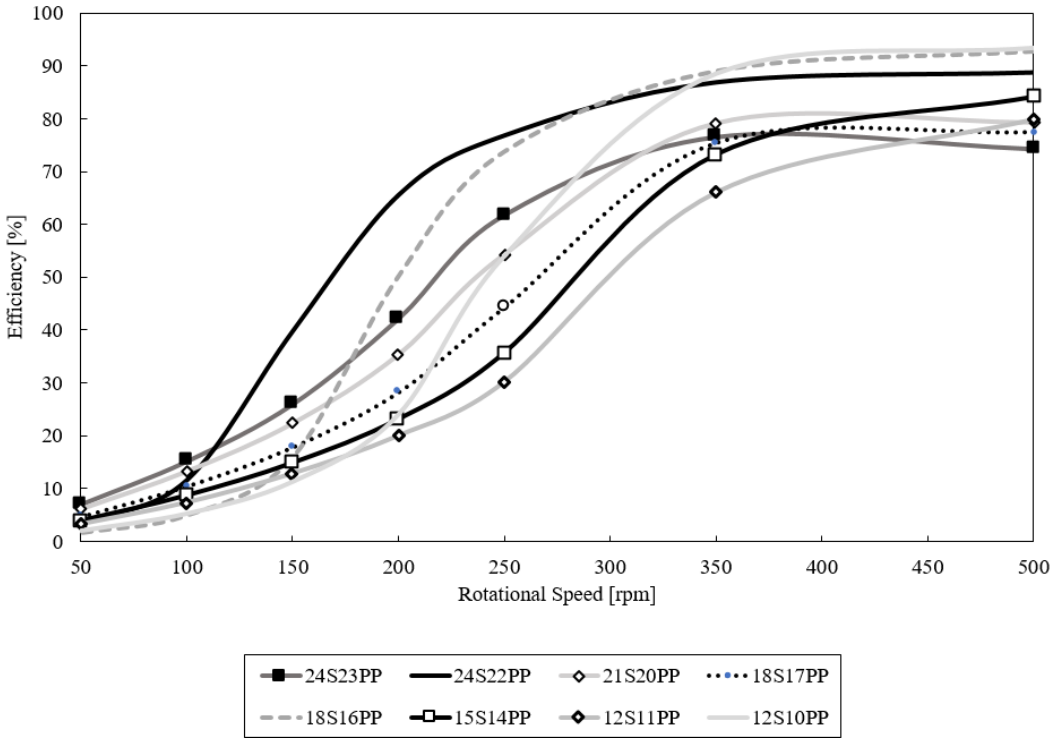


Fig. 3.19. N-η characteristics

### 3.5.3 Summary

In Chapter 3.5, eight surface permanent magnet vernier motors with various pol ratios were designed according to the design procedure in chapter 3.4, and the output characteristics, such as a cogging torque, torque ripple, N-T and N-η characteristics, according to the pole ratio were verified and analyzed by conducting 2-D FEM. According to the results, it can be seen that the surface magnet type vernier motor having 15 or more stator slots is excellent in the cogging torque and the torque ripple surface, and the motor with two winding pole pairs can drive a relatively higher torque.

## 3.6 Surface Permanent Magnet Vernier Linear Motor

Recently, direct drive linear motors have been used in various automation industries[46-49]. They have many advantages of faster response and more precise control than conventional linear systems using rotary motors such as conveying systems and indoor automatic door. However, since the linear motors are driven without mechanical gears, it does not have a high force. Accordingly, vernier linear motos are considered as a good alternative because the linear motor with a vernier effect can expect a relatively high power compared to existing direct drive motors. Previous research described a vernier motor in which permanent magnets are placed only on the stator for an application in the automatic household door[50]. Compared to conventional BLDC linear motors, it showed an improved performance. However, due to the lack of optimization of the design parameters, the results showed a low efficiency, high detent force and force ripple. Therefore, in this Chapter, a surface permanent magnet vernier linear motor is designed according to the design methodology, and its superiority is evaluated by comparing with the previous model[50] as shown in Fig. 3.20.

### 3.6.1 Structure of proposed vernier linear motor

The previous model[50] was designed as shown in Fig. 3.20. The proposed model shown in Fig. 3.21 has the same overall size as the previous model, and the number of stator slot and pole-pairs are designed differently to 16 and 18, respectively. As noted in Chapter 3.5, 18-slot 16-pole-pair vernier motors are chosen because they exhibited the widest operating range and high efficiency in the torque-speed characteristics as shown in Figs. 3.18 and 3.19. The design specification is shown in TABLE V.

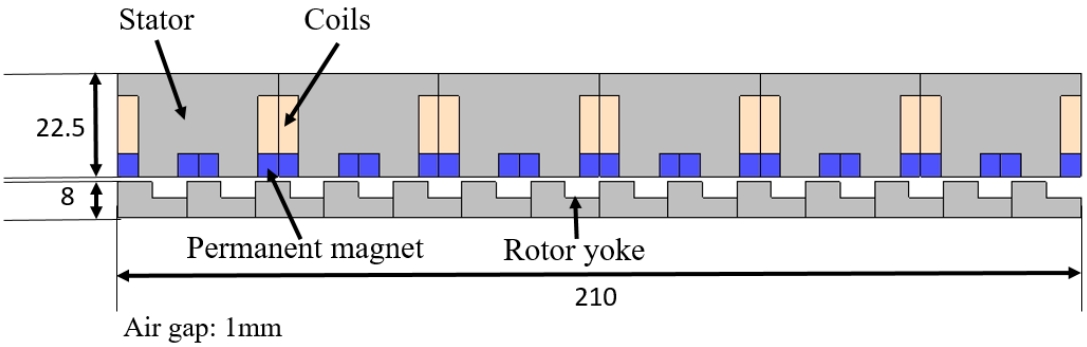


Fig. 3.20. 12-magnetic-poles 15-mover-pole vernier linear motor[50]

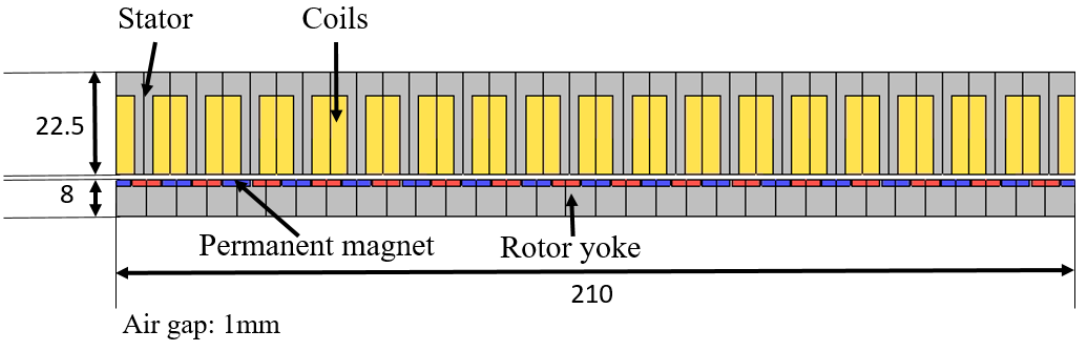


Fig. 3.21. 18-slot 16-pole-pair surface permanent vernier linear motor

TABLE V

MAIN DESIGN SPECIFICATION

| Item | Unit | Proposed motor | Previous motor |
|---|---|---|---|
| Motor Type | | Vernier motor | Vernier motor |
| Operation voltage | | 12VAC | 12VAC |
| Stator height | [mm] | 22.5 | 22.56 |
| Stator width | [mm] | 210 | 210 |
| Mover height | [mm] | 8 | 8 |
| Number of turns | [mm] | 79 | 388 |
| Phase resistance | [W] | 2.46293 | 16.797 |
| Air gap length | [mm] | 1 | 1 |
| Permanent magnet thickness | [mm] | 1 | 3 |
| Stack length | [mm] | 16 | 16 |
| Winding method | | Distributed winding | Concentrated winding |
| Permanent magnet Material | | NMX-S50 | NMX-S50 |
| Steel sheet | | 35JN210 | 35JN210 |

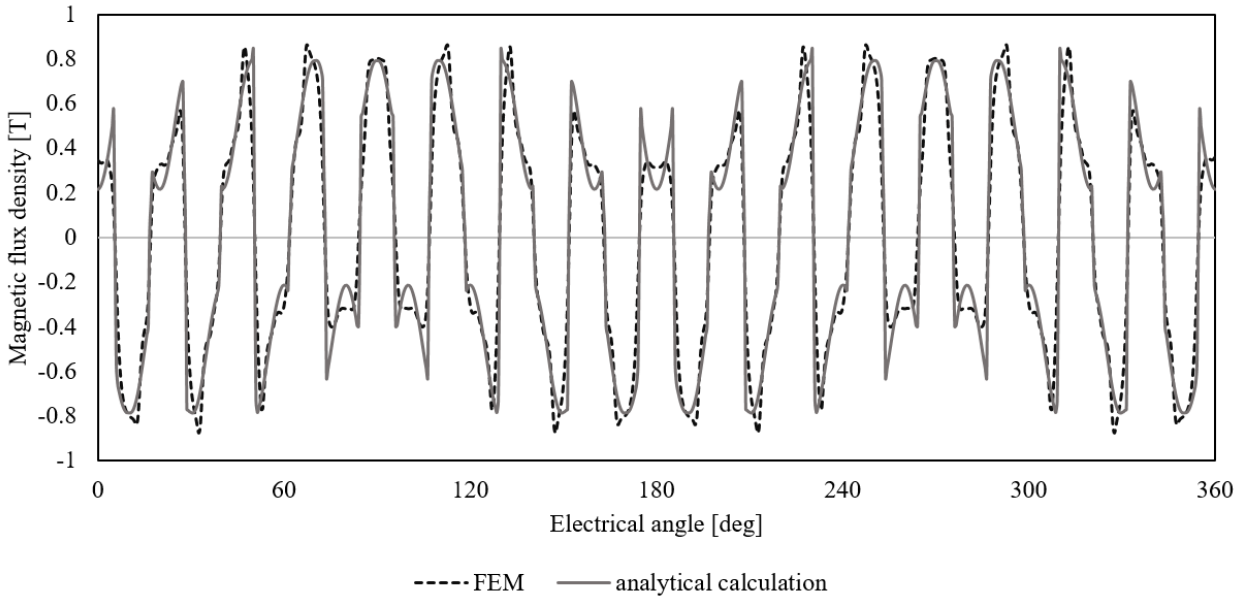


Fig. 3.22. Comparison of air gap magnetic flux density waveform by 2-D FEM

### 3.6.2 Design Parameter Optimization

According to the design procedure, the design parameters for the maximum thrust of the motor can be obtained. As shown in Figs. 3.22 and 3.23, the results of the analytical predictions are approximate to FEM. Using the analytical calculation method, the air gap magnetic flux density and its space harmonics used to drive the vernier motor can

be obtained quickly and accurately. As mentioned in Chapter 3.3.1, the amplitude $P_i A_j$ of the modulated harmonics within the magnetic flux density function $B\,\theta,\alpha$ can be determined by $P_i$ and $A_j$. The amplitude of the coefficients can be adjusted using the design parameters $h_m$ and $r_{open}$ of (3.4) and (3.8). The proposed motor is operated by the 2nd order harmonics. Therefore, the design parameter, such as a permanent magnet thickness $h_m$ on the mover and the stator teeth opening ratio $r_{open}$ between the slot pitch $t_s$ and opening length $b_0$. Fig. 3.24 shows the variation of the second order harmonics of the magnetic flux density according to the combination of the opening ratio from 10% to 80% and the permanent magnet thickness increasing from 0.25 mm to 2.5 mm by 0.25 mm. 140 cases were computed using the analytical calculation method, and the calculation time was 4.016 seconds. The highest second order harmonic is found when the slot opening ratio is 60% and the thickness of the permanent magnet is 1 mm.

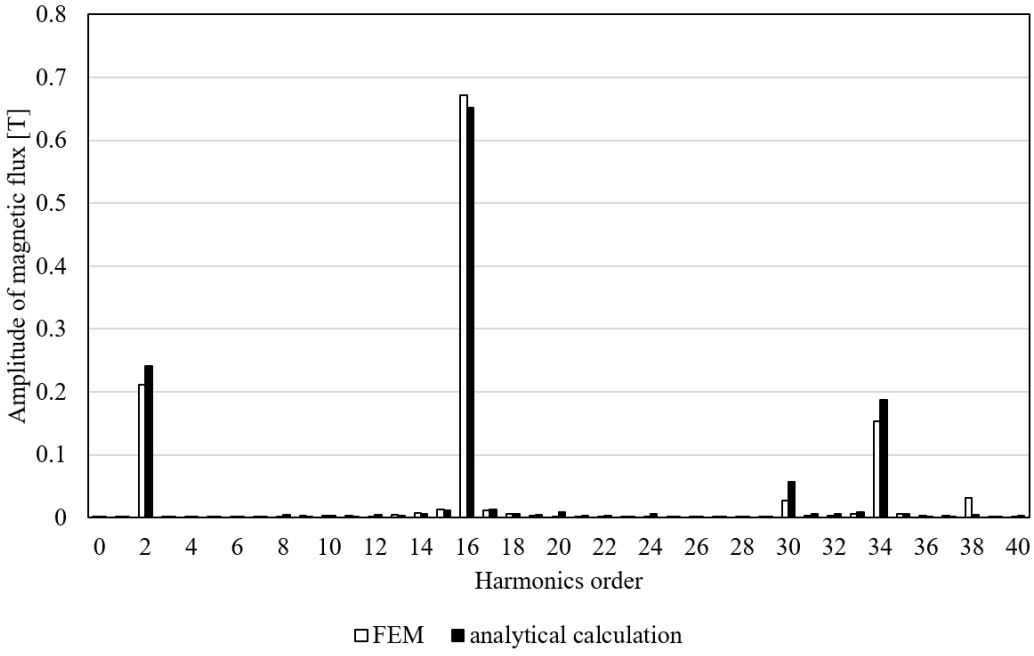


Fig. 3.23. Comparison of air gap magentic flux density harmonic spectra

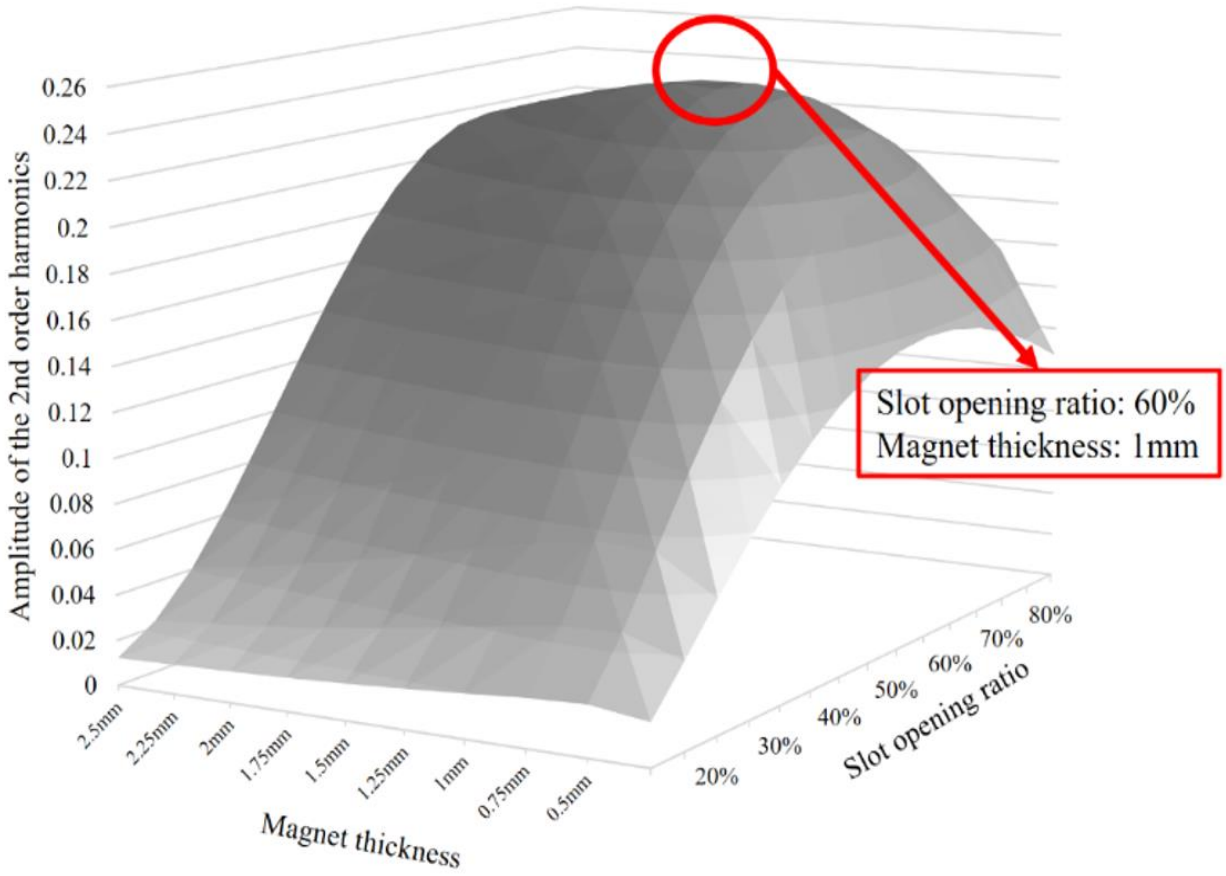


Fig. 3.24. Variation of the second-order harmonics in accordance with magnet thickness and slot opening ratio

### 3.6.3 Performance comparison using Finite Element Analysis

In order to verify the effectiveness of the proposed surface permanent magnet vernier linear motor, the results through 2-D FEM were compared with the previously studied vernier motor with 14-slots and 12-pole-pairs[50] shown in Fig. 3.20. The static thrust characteristics of each model are analyzed first, and the speed-torque characteristics are calculated.

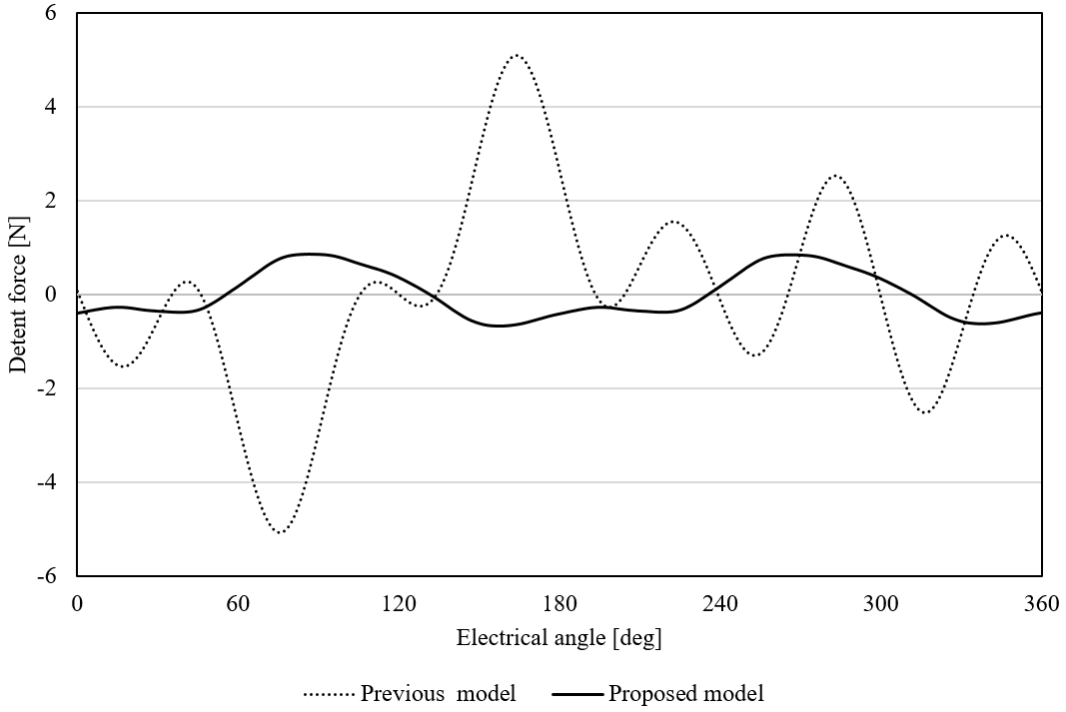


Fig. 3.25. Comparison of thrust characteristics at current 0A

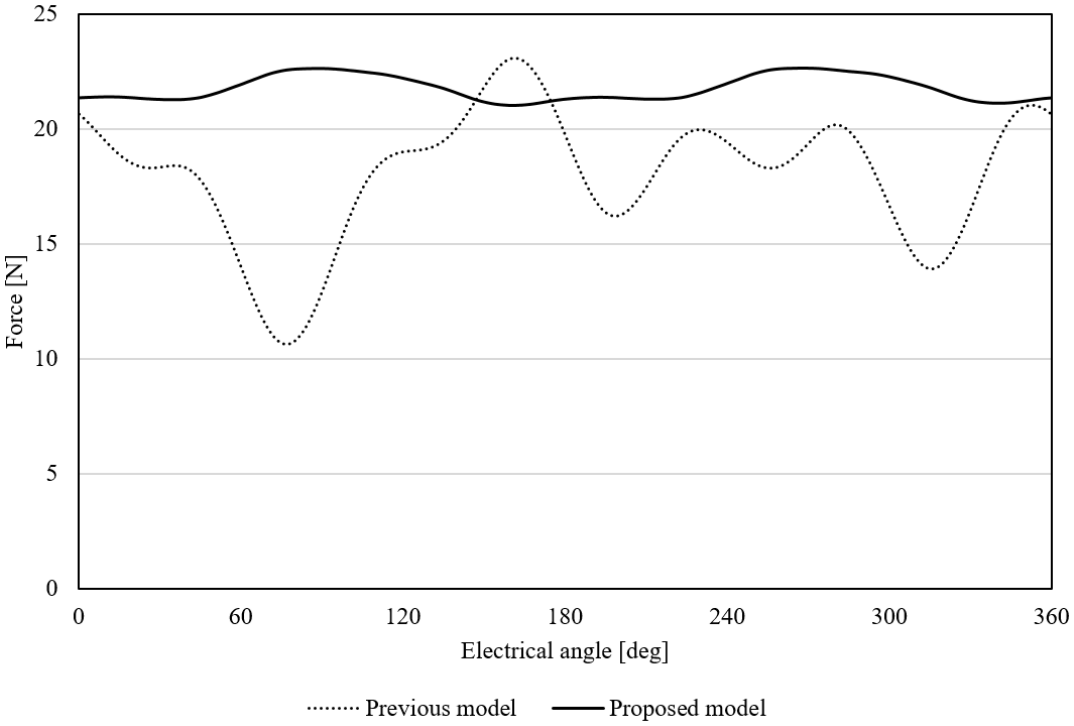


Fig. 3.26. Comparison of thrust characteristics at current 0.6A

Figs. 3.25 and 26 show the comparison of the thrust characteristics at currents of 0 and 0.6 A. When the current is 0 A, the detent force of the previously studied model is 10.2 N, while the optimized model is 1.5 N and is much lower. When a current of 0.6 A is applied, the average force and the ripple rate of the previous model are 18.0 N and 69.1%, respectively. However, those of the optimized model showed 21.8 N and 7.4%. When the current is applied, the average force of the optimized model is observed to be higher than 3.8 N, and the ripple rate and detent force are reduced more than 6 times as small as the previous model.

The N-T characteristics are calculated by applying a three-phase sinusoidal 12-V voltage source to the coils for each phase of both motors and by using a motion equation of the linear motor of the FEM. The N-T characteristics are calculated by increasing a load at constant intervals until the moving speed of each motor becomes 0 m/s, and the losses due to frictions are ignored in the calculation process. As shown in Fig. 3.27, both motors show similar results at a maximum speed of 0.53 m/s under no load.

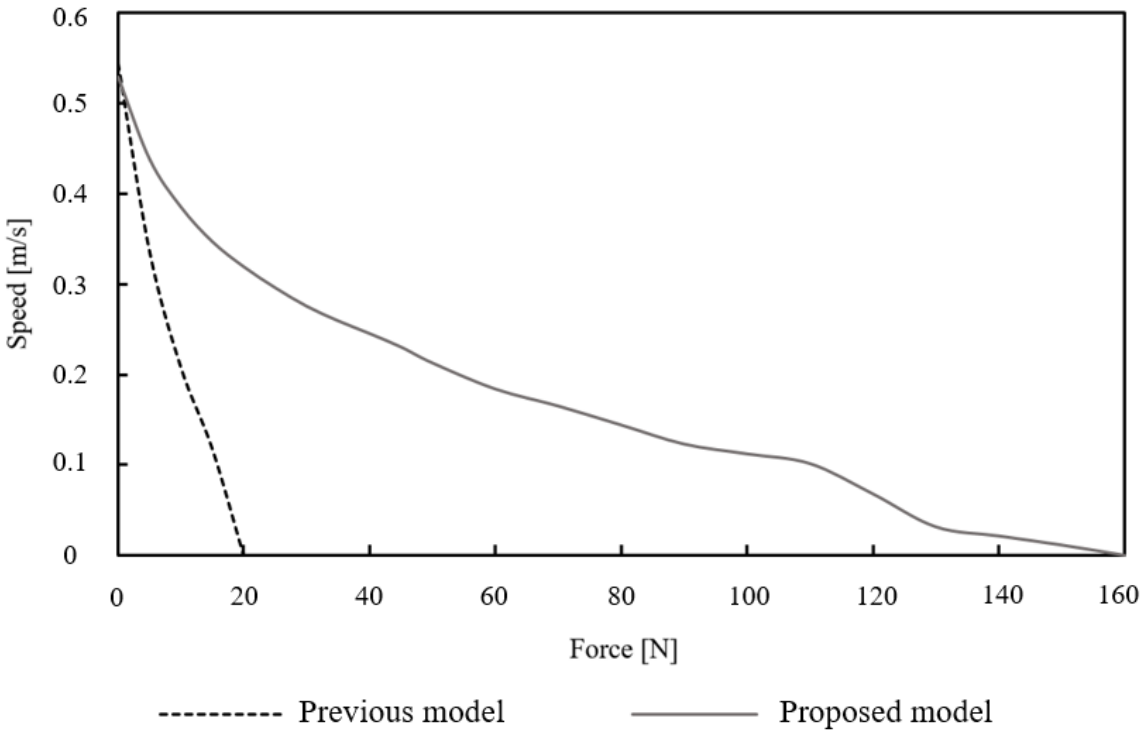


Fig. 3.27. Comparison of the N-T characteristics

However, the slope of the N-T curve of each motor shown in Fig. 3.27 represents a large difference of eight times. Therefore, the proposed motor showed superior performance in terms of motor size.

### 3.6.4 Summary

Using the design procedure, the design parameter optimization with the highest amplitude of the modulated harmonic of the magnetic flux density driving the proposed surface permanent magnet vernier linear motor was performed. The proposed model in the static thrust characteristics show much less ripple than the previous model and are much superior in the high force range.

## 3.7 Conclusion

Chapter 3 described the principle of operation through the mathematical modeling of vernier motors, and found features that operate using harmonics of the void magnetic field of a vernier motor. In particular, analytical calculation methods are described using the effect of air gap permeance on stator slots on specific harmonics. The analytical method was evaluated by comparing the results with 2-D FEM. A design procedure for generating the maximum torque of a surface magnet type vernier motor using an analytical calculation method with excellent results was presented, and the characteristics of eight vernier motors were analyzed using this method. Finally, using the proposed design procedure, a surface permanent magnet vernier linear motor with the same dimension as the previously studied motor was designed and the results were compared with each other. The effectiveness of the design methodology was evaluated through analysis of the FEM results of the two motors.

# Chapter 4 Thesis Conclusion

This paper aimed at mathematical modeling of a magnetic geared motor and vernier motor, which are electric motors with a magnetic gear effect. The air gap magnetic field distribution is calculated based on the parameters directly used in the design of the permanent magnet thickness, slot pitch, gap length, etc., and its excellent results are verified through FEM.

Chapter 1 describes in detail the magnetic gear, which is a feature of magnetic geared motors and vernier motors. First, the magnetic gears were classified and arranged according to the operation method from the initial model to the present. Next, the operation principle of the magnetic gear driven by the harmonics of the air gap magnetic field distribution is briefly described. Finally, the origin and kinds of the magnetic geared motor and the vernier motor to be covered in this paper are discussed.

In Chapter 2, the mathematical modeling of a magnetic geared motor was performed. First, the operational principle is described. An analytical calculation method is presented reflecting the characteristics of a magnetic geared motor with two rotors and pores and expressed in the order. The calculation results were first compared to the air gap magnetic field and its harmonics by performing a 2-D FEM. The comparison of the magnetic field results in the inner air gap showed excellent results. In the outer air gap, it was calculated by the same method as the inner air gap. However, it showed a large error. Therefore, reflecting the influence of the permanent magnet of the rotor, the fifth harmonic and the twelfth harmonic, which drive the magnetic geared motor, showed almost the same results.

In Chapter 3, mathematical modeling of a surface permanent magnet type vernier motor was discussed. First, the characteristics of the air gap permeance varying according to the opening ratio of the slot in describing the operation principle of the surface permanent magnet type vernier motor will be described. Here, the principle that the change of the air gap permeance significantly affects the harmonics of the magnetic field driving the vernier motor will be described. The results calculated by

the analytical method are compared with the 2-D FEM. EMF voltage and torque according to a various slot opening ratios and thickness of the rotor permanent magnets are calculated and displayed graphically and it can be seen that the analytical calculation method is superior through the almost same result. Next, the design methodology is presented to have the maximum torque of the surface permanent magnet type vernier motor using the analytical method. Then, the results of the 2-D FEM are obtained for each of 8 vernier motors designed using the design procedure, and the results are used to compare the characteristics of the surface permanent magnet vernier motor according to the pole ratio and winding pole number. Finally, the surface permanent magnet vernier linear motor was designed through the design procedure and evaluated the proposed design methodology by comparing the results with the previously studied models.

This paper has described its features in detail by performing mathematical modeling of two types of motors with a magnetic geared effect. In the case of vernier motors, it will be possible to reduce significantly the time consumed in designing vernier motors applicable to electric automobiles and other industrial electrical machines by the suggested design procedure and analytical calculation method. Thus, it is expected to contribute to the technological development of vernier motors and magnetic geared motor in the future.

# Reference

[1] C.Armstrong “power transmitting device” US patent 687 292, 1901.

[2] A. Neuland, “Apparatus for transmitting power,” US Patent 117 1351, 1913.

[3] H. Faus, “Magnet gearing” US Patent 2243 555, 1941.

[4] H. Hurvitz, “Magnetic gearing system,” US Patent 2 548 373, 1951.

[5] G. Reese, “Magnetic gearing arrangement,” US Patent 3 301 091, 1967

[6] S. Rand, S. Rand, “Magnetic transmission system,” US Patent 3 523 204, 1970.

[7] D. Hesmondhalgh and D. Tipping, “A multielement magnetic gear,” IEEE PROCEEDINGS, vol. 127, 1980.

[8] K. Tsurumoto and S. Kikuchi, “A new magnetic gear using permanent magnet,” IEEE Tran. Magn., vol. 23, no. 5, pp. 3622-3624, Sept. 1987.

[9] S. Kikuchi, “Design and characteristics of a new magnetic worm gear using permanent magnet,” IEEE TRANSACTIONS ON MAGNETICS, vol. 29, no. 6, NOVEMBER 1993.

[10] Y. D. Yao, D. R. Huang, C. C. Hsieh, D. Y. Chiang, S. J. Wang, and T. F. Ying, “The radial magnetic coupling studies of perpendicular magnetic gears,” *IEEE Transactions on Magnetics,* vol. 32, no. 5, pp. 5061-5063, 1996.

[11] C. Huang, M. Tsai, D. G. Dorrell and B. Lin, "Development of a Magnetic Planetary Gearbox," in *IEEE Transactions on Magnetics*, vol. 44, no. 3, pp. 403-412, March 2008.

[12] K. Atallah, and D. Howe, “A novel high-performance magnetic gear,” *Magnetics, IEEE Transactions on,* vol. 37, no. 4, pp. 2844-2846, 2001.

[13] K. Atallah, S. D. Calverley, and D. Howe, “Design, analysis and realisation of a

high-performance magnetic gear," *Electric Power Applications, IEE Proceedings -,* vol. 151, no. 2, pp. 135-143, 2004.

[14] K. Atallah, J. Wang, and D. Howe, "A high-performance linear magnetic gear," *Journal of Applied Physics,* vol. 97, no. 10, pp. 10N516, 2005.

[15] S. Mezani, K. Atallah, and D. Howe, "A high-performance axial-field magnetic gear," *Journal of Applied Physics,* vol. 99, no. 8, pp. 08R303, 2006.

[16] N. Niguchi, and K. Hirata, "Cogging Torque Analysis of Magnetic Gear," *Industrial Electronics, IEEE Transactions on,* vol. 59, no. 5, pp. 2189-2197, 2012.

[17] N. Niguchi, and K. Hirata, "Cogging torque characteristics of magnetic - geared motor," *COMPEL - The international journal for computation and mathematics in electrical and electronic engineering,* vol. 31, no. 5, pp. 1470-1481, 2012.

[18] N. Niguchi, and K. Hirata, "Torque-Speed Characteristics Analysis of a Magnetic-Geared Motor Using Finite Element Method Coupled With Vector Control," *Magnetics, IEEE Transactions on,* vol. 49, no. 5, pp. 2401-2404, 2013.

[19] E. Morimoto, K. Hirata, N. Niguchi, and Y. Ohno, "Design and Analysis of Magnetic-Geared Motor With Field Windings," *Magnetics, IEEE Transactions on,* vol. 50, no. 11, pp. 1-4, 2014.

[20] N. Niguchi, and K. Hirata, "Magnetic-geared motors with high transmission torque density," *COMPEL - The international journal for computation and mathematics in electrical and electronic engineering,* vol. 34, no. 2, pp. 428-438, 2015.

[21] K. Atallah, J. Rens, S. Mezani, and D. Howe, "A Novel "Pseudo" Direct-Drive Brushless Permanent Magnet Machine," *Magnetics, IEEE Transactions on,* vol. 44, no. 11, pp. 4349-4352, 2008.

[22] K. Atallah, W. Jiabin, S. D. Calverley, and S. Duggan, "Design and Operation of a

Magnetic Continuously Variable Transmission," *Industry Applications, IEEE Transactions on,* vol. 48, no. 4, pp. 1288-1295, 2012.

[23] A. Zaini, N. Niguchi, and K. Hirata, "Continuously Variable Speed Vernier Magnetic Gear," *Magnetics, IEEE Transactions on,* vol. 48, no. 11, pp. 3104-3107, 2012.

[24] N. Shuangxia, S. L. Ho, and W. N. Fu, "Design of a Novel Electrical Continuously Variable Transmission System Based on Harmonic Spectra Analysis of Magnetic Field," *Magnetics, IEEE Transactions on,* vol. 49, no. 5, pp. 2161-2164, 2013.

[25] C. H. Lee, "Vernier Motor and Its Design," *Power Apparatus and Systems, IEEE Transactions on,* vol. 82, no. 66, pp. 343-349, 1963.

[26] A. Toba, and T. A. Lipo, "Generic torque-maximizing design methodology of surface permanent-magnet vernier machine," *Industry Applications, IEEE Transactions on,* vol. 36, no. 6, pp. 1539-1546, 2000.

[27] K. Okada, N. Niguchi, and K. Hirata, "Analysis of a Vernier Motor with Concentrated Windings," *Magnetics, IEEE Transactions on,* vol. 49, no. 5, pp. 2241-2244, 2013.

[28] L. Jiangui, and K. T. Chau, "Performance and Cost Comparison of Permanent-Magnet Vernier Machines," *Applied Superconductivity, IEEE Transactions on,* vol. 22, no. 3, pp. 5202304-5202304, 2012.

[29] S. Hyoseok, N. Niguchi, and K. Hirata, "Characteristic Analysis of Surface Permanent-Magnet Vernier Motor According to Pole Ratio and Winding Pole Number," *IEEE Transactions on Magnetics,* vol. 53, no. 11, pp. 1-4, 2017.

[30] A. Ishizaki, T. Tanaka, K. Takasaki, and S. Nishikata, "Theory and optimum design of PM Vernier motor." pp. 208-212.

[31] E. Spooner, and L. Haydock, "Vernier hybrid machines," *IEE Proceedings - Electric*

*Power Applications,* vol. 150, no. 6, pp. 655-662, 2003.

[32] K. C. Mukherji, and A. Tustin, “Vernier reluctance motor,” *Proceedings of the Institution of Electrical Engineers,* vol. 121, no. 9, pp. 965-974, 1974.

[33] L. Xu, G. Liu, W. Zhao, X. Yang, and R. Cheng, “Hybrid Stator Design of Fault-Tolerant Permanent-Magnet Vernier Machines for Direct-Drive Applications,” *IEEE Transactions on Industrial Electronics,* vol. 64, no. 1, pp. 179-190, 2017.

[34] R. Zhang, J. Li, R. Qu, and D. Li, “Analysis and Design of Triple-Rotor Axial-Flux Spoke-Array Vernier Permanent Magnet Machines,” *IEEE Transactions on Industry Applications,* vol. 54, no. 1, pp. 244-253, 2018.

[35] S. Tabi, A. Tounzi, and F. Piriou, “Study of a Stator Current Excited Vernier Reluctance Machine,” *IEEE Transactions on Energy Conversion,* vol. 21, no. 4, pp. 823-831, 2006.

[36] T. Sekine, K. Hijikata, and Y. Tanaka, "Investigation of torque and suspension force characteristic in a reluctance type bearingless vernier motor." pp. 1-6.

[37] K. Byungtaek, and T. A. Lipo, “Operation and Design Principles of a PM Vernier Motor,” *Industry Applications, IEEE Transactions on,* vol. 50, no. 6, pp. 3656-3663, 2014.

[38] Z. Q. Zhu, and D. Howe, “Instantaneous magnetic field distribution in brushless permanent magnet DC motors. III. Effect of stator slotting,” IEEE Transactions on Magnetics, vol. 29, no. 1, pp. 143-151, 1993.

[39] Z. Q. Zhu, D. Howe, E. Bolte, and B. Ackermann, “Instantaneous magnetic field distribution in brushless permanent magnet DC motors. I. Open-circuit field,” IEEE Transactions on Magnetics, vol. 29, no. 1, pp. 124-135, 1993.

[40] F. W. Carter, “The magnetic field of the dynamo-electric machine,” Electrical Engineers, Journal of the Institution of, vol. 64, no. 359, pp. 1115-1138, 1926.

[41] T. Zou, X. Han, D. Jiang, R. Qu, and D. Li, “Inductance Evaluation and Sensorless Control of a Concentrated Winding PM Vernier Machine,” IEEE Transactions on Industry Applications, pp. 1-1, 2018.

[42] R. Zhang, J. Li, R. Qu, and D. Li, “Analysis and Design of Triple-Rotor Axial-Flux Spoke-Array Vernier Permanent Magnet Machines,” IEEE Transactions on Industry Applications, vol. 54, no. 1, pp. 244-253, 2018.

[43] X. Zhang, X. Liu, and Z. Chen, “A Novel Dual-Flux-Modulator Coaxial Magnetic Gear for High Torque Capability,” IEEE Transactions on Energy Conversion, pp. 1-1, 2017.

[44] L. Xu, G. Liu, W. Zhao, X. Yang, and R. Cheng, “Hybrid Stator Design of Fault-Tolerant Permanent-Magnet Vernier Machines for Direct-Drive Applications,” IEEE Transactions on Industrial Electronics, vol. 64, no. 1, pp. 179-190, 2017.

[45] T. SUGIYAMA, “Basic Design Method for SPMSM Based on Air - Gap Magnetic Flux Density Distribution Focusing on Image Magnetic Pole,” Electrical Engineering in Japan, vol. 200, no. 4, pp. 53-67, 2017.

[46] Y. Fujimoto, T. Kominami, and H. Hamada, "Development and Analysis of a High Thrust Force Direct-Drive Linear Actuator," IEEE Transactions on Industrial Electronics, vol. 56, pp. 1383-1392, 2009.

[47] Q. Liu, H. Yu, M. Hu, C. Liu, J. Zhang, L. Huang, et al., "Cogging Force Reduction of Double-Sided Linear Flux-Switching Permanent Magnet Machine for Direct Drives," IEEE Transactions on Magnetics, vol. 49, pp. 2275-2278, 2013.

[48] W. Zhong, H. Yu, M. Hu, Z. Shi, and Q. Liu, "Study on a Novel Pseudo-Six-Phase Linear Flux-Switching Permanent-Magnet Machine for Direct Drive," IEEE Transactions on Applied Superconductivity, vol. 26, pp. 1-4, 2016.

[49] S. Zhou, H. Yu, M. Hu, C. Jiang, and L. Huang, "Nonlinear Equivalent Magnetic Circuit Analysis for Linear Flux-Switching Permanent Magnet Machines," IEEE Transactions on Magnetics, vol. 48, pp. 883-886, 2012.

[50] D. Kameda, K. Hirata, and N. Niguchi, "Study of linear vernier motor for household automatic doors," in 2017 11th International Symposium on Linear Drives

for Industry Applications (LDIA), 2017, pp. 1-4.

# Research Achievements

## Published Papers

1. S. Hyoseok, N. Niguchi and K. Hirata, "Characteristic Analysis of Surface Permanent-Magnet Vernier Motor According to Pole Ratio and Winding Pole Number," in *IEEE Transactions on Magnetics*, vol. 53, no. 11, pp. 1-4, Nov. 2017, Art no. 8211104.
2. Hyoseok Shi, Noboru Niguchi, and Katsuhiro Hirata, “Analytical Calculation of Air Gap Magnetic Field Distribution in Magnetic Geared Motors,” in Journal of Power Electronics, vol. 19, No. 3, pp.794-802, May 2019

## International Conferences

1. Hyoseok Shi, Noboru Niguchi and Katsuhiro Hirata, “Design and Analysis of Surface Permanent Magnet Vernier Linear Motor Based on Air Gap Magnetic Flux Density Distribution,” *2019 13th International Symposium on Linear Drives for Industry Applications(LDIA),* Neuchatel, Switzerland (Accepted)
2. H. Shi, N. Niguchi and K. Hirata, "Analytical Calculation of Air Gap Magnetic Flux Density Distribution in Magnetic Geared Motor," TENCON 2018 - 2018 IEEE Region 10 Conference, Jeju, Korea (South), 2018, pp. 0767-0771.
3. H. Shi, N. Niguchi and K. Hirata, "Analytical calculation of air gap magnetic field distribution in vernier motor," 2017 IEEE 12th International Conference on Power Electronics and Drive Systems (PEDS), Honolulu, HI, 2017, pp. 247-251.
4. H. Shi and K. Hirata, "Characteristic analysis of surface permanent magnet vernier motor with concentrated winding according to pole ratio and winding pole number," 2017 IEEE International Magnetics Conference (INTERMAG), Dublin, 2017, pp. 1-1.

Domestic Conferences

1. Shi Hyoseok, 平田勝弘, “Proposal of New Vernier Machine with Dual Stator and Spoke-Array Permanent Magnet”, 電気学会 回転機・リニアドライブ・家電・民生合同研究会; , LD-15-030, pp.43-46, 2015.08

# Acknowledgments

Firstly, I would like to express my sincere gratitude to my advisor Professor Katsuhiro Hirata for the continuous support of my Ph.D. study and related research, for his patience, motivation, and immense knowledge. His guidance helped me in all the time of research and writing of this thesis. I could not have imagined having a better advisor and mentor for my Ph.D. study.

Besides my advisor, I would like to thank the rest of my thesis committee: Professor Katsuaki Suganuma and Associate Professor Fumikazu Miyasaka for their insightful comments and encouragement, but also for the hard question which incented me to widen my research from various perspectives.

My sincere thank also goes to Assistant Professor Noboru Niguchi who has been always advising on my research. This research could not be done without his valuable support.

I would like to express my gratitude to the lab colleagues for making the time spent in the Hirata laboratory a wonderful experience.

Thanks are also extended to all my friends and colleagues for all their help during my stay in Osaka.

Last but not the least, I would like to thank my family: my parents and to my sister for supporting me spiritually throughout writing this thesis and my life in general.